

1 LEVERAGING MULTI-MESSENGER ASTROPHYSICS FOR DARK MATTER SEARCHES

By

Daniel Nicholas Salazar-Gallegos

A DISSERTATION

Submitted to
Michigan State University
in partial fulfillment of the requirements
for the degree of

Physics—Doctor of Philosophy
Computational Mathematics in Science and Engineering—Dual Major

Today

ABSTRACT

3 I did Dark Matter with HAWC and IceCube. I also used Graph Neural Networks

⁴ Copyright by

⁵ DANIEL NICHOLAS SALAZAR-GALLEGOS

⁶ Today

ACKNOWLEDGMENTS

8 I love my friends. Thanks to everyone that helped me figure this out. Amazing thanks to the people
9 at LANL who supported me. Eames, etc Dinner Parties Jenny and her child Kaydince Kirsten, Pat,
10 Andrea Family. You're so far but so critical to my formation. Unconditional love. Roommate

TABLE OF CONTENTS

12	LIST OF TABLES	vii
13	LIST OF FIGURES	viii
14	LIST OF ABBREVIATIONS	xv
15	CHAPTER 1 INTRODUCTION	1
16	CHAPTER 2 DARK MATTER IN THE COSMOS	2
17	2.1 Introduction	2
18	2.2 Dark Matter Basics	3
19	2.3 Evidence for Dark Matter	4
20	2.4 Searching for Dark Matter: Particle DM	11
21	2.5 Sources for Indirect Dark Matter Searches	16
22	2.6 Multi-Messenger Dark Matter	18
23	CHAPTER 3 HIGH ALTITUDE WATER CHERENKOV (HAWC) OBSERVATORY	21
24	3.1 The Detector	21
25	3.2 Events Reconstruction and Data Acquisition	21
26	3.3 Remote Monitoring	21
27	CHAPTER 4 ICECUBE NEUTRINO OBSERVATORY	22
28	4.1 The Detector	22
29	4.2 Events Reconstruction and Data Acquisition	22
30	4.3 Northern Test Site	22
31	CHAPTER 5 GLORY DUCK: MULTI-WAVELENGTH SEARCH FOR DARK MATTER ANNIHILATION TOWARDS DWARF SPHEROIDAL GALAXIES	23
32	5.1 Introduction	23
33	5.2 Dataset and Background	25
34	5.3 Analysis	26
35	5.4 Likelihood Methods	31
36	5.5 HAWC Results	37
37	5.6 Glory Duck Combined Results	40
38	5.7 HAWC Systematics	45
39	5.8 J -factor distributions	46
40	5.9 Discussion and Conclusions	52
43	CHAPTER 6 MULTITHREADING HAWC ANALYSES FOR DARK MATTER SEARCHES	56
44	6.1 Introduction	56
45	6.2 Dataset and Background	56
46	6.3 Analysis	58

48	6.4	Likelihood Methods	61
49	6.5	Computational Methods: Multithreading	62
50	6.6	Analysis Results	68
51	6.7	Systematics	73
52	6.8	Conclusion and Discussion	73
53	CHAPTER 7	HEAVY DARK MATTER ANNIHILATION SEARCH WITH ICE-CUBE'S NORTH SKY TRACK DATA	75
54			
55	CHAPTER 8	NU DUCK	76
56	APPENDIX A	MULTI-EXPERIMENT SUPPLEMENTARY FIGURES	77
57	APPENDIX B	MULTITHREADING DARK MATTER ANALYSES SUPPLEMENTARY MATERIAL	78
58			
59	B.1	Remaining Spectral Models	78
60	B.2	<code>mpu_analysis.py</code>	79
61	B.3	Comparison with Glory Duck	88
62	BIBLIOGRAPHY	91

LIST OF TABLES

<p>64 Table 5.1 Summary of the relevant properties of the dSphs used in the present work. Column 1 lists the dSphs. Columns 2 and 3 present their heliocentric distance and galactic coordinates, respectively. Columns 4 and 5 report the J-factors of each source given from the \mathcal{GS} and \mathcal{B} independent studies and their estimated $\pm 1\sigma$ uncertainties. The values $\log_{10} J$ (\mathcal{GS} set) [45] correspond to the mean J-factor values for a source extension truncated at the outermost observed star. The values $\log_{10} J$ (\mathcal{B} set) [47] are provided for a source extension at the tidal radius of each dSph. Bolded sources are within HAWC's field of view and provided to the Glory Duck analysis.</p> <p>73 Table 5.2 Summary of dSph observations by each experiment used in this work. A ‘-’ indicates the experiment did not observe the dSph for this study. For Fermi-LAT, the exposure at 1 GeV is given. For HAWC, $\Delta\theta$ is the absolute difference between the source declination and HAWC latitude. HAWC is more sensitive to sources with smaller $\Delta\theta$. For IACTs, we show the zenith angle range, the total exposure, the energy range, the angular radius θ of the signal or ON region, the ratio of exposures between the background-control (OFF) and signal (ON) regions (τ), and the significance of gamma-ray excess in standard deviations, σ.</p> <p>82 Table 6.1 Summary of the relevant properties of the dSphs used in the present work. Column 1 lists the dSphs. Columns 2 and 3 present their heliocentric distance and galactic coordinates, respectively. Column 4 reports the J-factors of each source given from the \mathcal{LS} studies and estimated $\pm 1\sigma$ uncertainties. The values $\log_{10} J$ (\mathcal{LS} set) [65] correspond to the mean J-factor values for a source extension truncated at 0.5°.</p> <p>88 Table 6.2 Timing summaries for analyses for serial and multithreaded processes. M tasks is the number of functional-parallel tasks ran for the computation. $T_{p,c}$ is a single run time in hours:minutes:seconds for runs utilizing p nodes and c threads. Runs are run interactively on the same computer to maximize consistency. Empty entries are indicated with ‘-’. (.) entries are estimated entries extrapolated from data earlier in the column.</p> <p>94 Table 6.3 Speed up summaries for analyses for serial and multithreaded processes. M tasks is the number of functional-parallel tasks ran for the computation. $S_{p,c}$ is a single speedup comparison for runs utilizing p nodes and c threads. $[\cdot]$ are the estimated speedups calculated from Tab. 6.2, Eq. (6.10), and Eq. (6.5). Empty entries are indicated with ‘-’.</p> <p>99 Proof I know how to include</p>	<p>31</p> <p>32</p> <p>62</p> <p>66</p> <p>66</p> <p>68</p>
--	---

LIST OF FIGURES

101	Figure 2.1	Rotation curve fit to NGC 6503 from [7]. Dashed line is the contribution 102 from visible matter. Dotted curves are from gas. Dash-dot curves are from 103 dark matter (DM). Solid line is the composite contribution from all matter 104 and DM sources. Data are indicated with bold dots with error bars. Data 105 agree strongly with a matter + DM composite prediction.	5
106	Figure 2.2	Light from distant galaxy is bent in unique ways depending on the distribution 107 of mass between the galaxy and Earth. Yellow dashed lines indicate where 108 the light would have gone if the matter were not present [8].	7
109	Figure 2.3	(left) Optical image of galactic cluster 1E0657-558. (right) X-ray image of the 110 cluster with redder meaning hotter and higher baryon density. (both) Green 111 contours are reconstruction of gravity contours from weak lensing. White 112 rings are the best fit mass maxima at 68.3%, 95.5%, and 99.7% confidence. 113 The matter maxima of the clusters are clearly separated from x-ray maxima. [9]	8
114	Figure 2.4	Plank CMB sky. Sky map features small variations in temperature in primor- 115 dial light. These anisotropies are used to make inferences about the universe's 116 energy budget and developmental history. [10]	9
117	Figure 2.5	Observed Cosmic Microwave Background power spectrum as a function of 118 multipole moment from Plank [10]. Blue line is best fit model from Λ CDM. 119 Red points and lines are data and error, respectively.	10
120	Figure 2.6	Predicted power spectra of CMB for different $\Omega_m h^2$ values for fixed baryon 121 density from [11]. (left) Low $\Omega_m h^2$ increases the prominence of first and 122 second peaks. (middle) $\Omega_m h^2$ is most similar to the observed power spectrum. 123 The second and third peaks are similar in height. (right) $\Omega_m h^2$ is large which 124 suppresses the first peak and raises the prominence of the third peak.	10
125	Figure 2.7	The Standard Model (SM) of particle physics. Figure taken from http://www.quantumdiaries.org/2014/03/14/the-standard-model-a-beautiful-but-flawed-theory/	12
128	Figure 2.8	Simplified Feynman diagram demonstrating with different ways DM can 129 interact with SM particles. The 'X's refer to the DM particles whereas the 130 SM refer to fundamental particles in the SM. The large circle in the center 131 indicates the vertex of interaction and is purposely left vague. The colored 132 arrows refer to different directions of time as well as their respective labels. 133 The arrows indicate the initial and final state of the DM -SM interaction in time.	13

134	Figure 2.9 A single jet event in ATLAS detector from 2017 [16]. Jet momentum was 135 observed to be 1.9 TeV. Missing transverse momentum was observed to be 136 1.9 TeV compared to the initial transverse momentum of the event was 0. 137 Implied MET is traced by a red dashed line in event display.	14
138	Figure 2.10 More detailed pseudo-Feynman diagram of particle cascade from dark matter 139 annihilation into 2 quarks. The quarks hadronize and down to stable particles 140 like γ or the anti-proton (p^-). Diagram pulled from ICRC 2021 presentation 141 on DM annihilation search [17].	15
142	Figure 2.11 Dark Matter (DM) decay spectrum for $b\bar{b}$ initial state and γ final state. Redder 143 spectra are for larger DM masses. Bluer spectra are light DM masses. x is a 144 unitless factor defined as the ratio of the mass of DM, m_χ , and the final state 145 particle energy E_γ . Figure from [19].	17
146	Figure 2.12 Different dark matter density profiles compared. Some models produce ex- 147 ceptionally large densities at small r [20].	18
148	Figure 2.13 The Milky Way Galaxy in photons (γ) and neutrinos (ν) [22]. The Galactic 149 center is at $l=0^\circ$ and is the brightest region in all panels. (top) An Optical 150 color image of the Milky Way galaxy seen from Earth. Clouds of gas and dust 151 obscure some light from stars. (2nd down) Integrated flux of γ -rays observed 152 by the Fermi-LAT telescope [23]. (middle) Expected neutrino emission 153 that corresponds with Fermi-LAT observations. (2nd up) Expected neutrino 154 emission profile after considering detector systematics of IceCube. (bottom) 155 Observed neutrino emission from region of the galactic plane. Substantial 156 neutrino emission was detected.	19
157	Figure 2.14 Dark Matter annihilation spectra for different final state particle and standard 158 model annihilation channels [24]. Photons (red), e^\pm (green), \bar{p} (blue), ν (black).	20
159	Figure 5.1 Sensitivities of five gamma-ray experiments compared to percentages of the 160 Crab nebula's emission and dark matter annihilation. Solid lines present 161 estimated sensitivities to power law spectra [FACT CHECK THIS] for each 162 experiment. Green lines are Fermi-LAT sensitivities where lighter green is 163 the sensitivity to the galactic center and dark green is its sensitivity to higher 164 declinations. Orange, red, and purple solid lines represent the MAGIC, HESS, 165 and VERITAS 50 hour sensitivities respectively. The maroon and brown lines 166 are the HAWC 1 year and 5 year sensitivities. Across four decades of gamma- 167 ray energy, these experiments have similar sensitivities on the order 10^{-12} 168 $\text{erg cm}^{-2}\text{s}^{-1}$. The dotted lines are estimated dark matter fluxes assuming 169 $m_\chi = 5 \text{ TeV}$ DM annihilating to bottom quarks (red), tau leptons (blue), 170 and W bosons (green). Faded gray lines outline percentage flux of the Crab 171 nebula. Figure is an augmented version of [25]	24

172	Figure 5.2 Effect of Electroweak (EW) corrections on expected DM annihilation spec-	
173	trum for $\chi\chi \rightarrow W^-W^+$. Solid lines are spectral models that consider EW	
174	corrections. Dash-dot lines are spectral models without EW corrections. Red	
175	lines are models for $M_\chi = 1$ TeV. Blue lines represent models for $M_\chi = 100$	
176	TeV. All models are sourced from the PPPC4DMID [44].	28
177	Figure 5.3 $\frac{dJ}{d\Omega}$ maps for Segue1 (top) and Coma Berenices (bottom). Origin is centered	
178	on the specific dwarf spheroidal galaxies (dSph). X and Y axes are the	
179	angular separation from the center of the dwarf. Plots of the remaining 11	
180	dSph HAWC studied are linked in Fig. A.1.	30
181	Figure 5.4 Illustration of the combination technique showing a comparison between	
182	$-2 \ln \lambda$ provided by four instruments (colored lines) from the observation	
183	of the same dSph without any J nuisance and their sum, <i>i.e.</i> the resulting	
184	combined likelihood (thin black line). According to the test statistics of	
185	Equation (5.6), the intersection of the likelihood profiles with the line $-2 \ln \lambda$	
186	= 2.71 indicates the 95% C.L. upper limit on $\langle \sigma v \rangle$. The combined likelihood	
187	(thin black line) shows a smaller value of upper limit on $\langle \sigma v \rangle$ than those	
188	derived by individual instruments. We also show how the uncertainties on	
189	the J factor effects the combined likelihood and degrade the upper limit on	
190	$\langle \sigma v \rangle$ (thick black line). All likelihood profiles are normalized so that the global	
191	minimum $\widehat{\langle \sigma v \rangle}$ is 0. We note that each profile depends on the observational	
192	conditions in which a target object was observed. The sensitivity of a given	
193	instrument can be degraded and the upper limits less constraining if the	
194	observations are performed in non-optimal conditions such as a high zenith	
195	angle or a short exposure time.	35
196	Figure 5.5	38
197	Figure 5.6 HAWC TS values for best fit $\langle \sigma v \rangle$ versus m_χ for seven SM annihilation	
198	channels with J factors from \mathcal{GS} . The solid black line shows the combined	
199	best fit TS values. The colored, dashed lines are the TS values for each of the	
200	13 sources HAWC studied.	39
201	Figure 5.7 HAWC Brazil bands at 95% confidence level on $\langle \sigma v \rangle$ versus DM mass for	
202	seven annihilation channels with J -factors from \mathcal{GS} [53]. The solid line	
203	represents the combined limit from 13 dSphs. The dashed line is the expected	
204	limit. The green band is the 68% containment. The yellow band is the 95%	
205	containment.	40

206	Figure 5.8	Upper limits at 95% confidence level on $\langle \sigma v \rangle$ in function of the DM mass for 207 eight annihilation channels, using the set of J factors from Ref. [53] (\mathcal{GS} set 208 in Table 5.1). The black solid line represents the observed combined limit, 209 the black dashed line is the median of the null hypothesis corresponding 210 to the expected limit, while the green and yellow bands show the 68% and 211 95% containment bands. Combined upper limits for each individual detector 212 are also indicated as solid, colored lines. The value of the thermal relic 213 cross-section in function of the DM mass is given as the red dotted-dashed 214 line [54].	41
215	Figure 5.9	Same as Fig. 5.8, using the set of J factors from Ref. [47, 55] (\mathcal{B} set in Table 5.1).	42
216	Figure 5.10	Comparisons of the combined limits at 95% confidence level for each of the 217 eight annihilation channels when using the J factors from Ref. [53] (\mathcal{GS} set in 218 Table 5.1), plain lines, and the J factor from Ref. [47, 55] (\mathcal{B} set in Table 5.1), 219 dashed lines. The cross-section given by the thermal relic is also indicated [54].	44
220	Figure 5.11	Comparisons of the combined limits at 95% confidence level for a point source 221 analysis and extended source using [53] \mathcal{GS} J-factor distributions and PPPC 222 [44] annihilation spectra. Shown are the limits for Segue1 which will have 223 the most significant impact on the combined limit. 6 of the 7 DM annihilation 224 channels are shown. Solid lines are extended source studies. Dashed lines 225 are point source studies. Overall, the extended source analysis improves the 226 limit by a factor of 2.	46
227	Figure 5.12	Same as Fig. 5.11 on Coma Berenices. This dSph also contributes signifi- 228 cantly to the limit. The limits are identical in this case.	47
229	Figure 5.13	Comparison of combined limits when correcting for HAWC's pointing sys- 230 tematic. All DM annihilation channels are shown. The solid black line is the 231 ratio between published limit to the declination corrected limit. The blue solid 232 line or "Combined_og" represented the limits computed for Glory Duck. The 233 solid orange line or "Combined_ad" represented the limits computed after 234 correcting for the pointing systematic.	48
235	Figure 5.14	Differential map of dJ/Ω from model built in Section 5.8.1 and profiles 236 provided directly from authors. (Top) Differential from Segue1. (bottom) 237 Differential from Coma Berenices. Note that their scales are not the same. 238 Segue1 shows the deepest discrepancies which is congruent with its large 239 uncertainties. Both models show anuli where unique models become apparent.	49

240	Figure 5.15 HAWC limits for Coma Berenices (top) and Segue1 (bottom) for two different map sets. Blue lines are limits calculated on maps with poor model representation. Orange lines are limits calculated on spatial profiles provided by the authors of [45]. Black line is the ratio of the poor spatial model limits to the corrected spatial models. The left y-axis measures $\langle \sigma v \rangle$ for the blue and orange lines. The right y-axis measures the ratio and is unitless.	50
246	Figure 5.16 Comparisons between the J -factors versus the angular radius for the computation of J factors from Ref. [53] (\mathcal{GS} set in Table 5.1) in blue and for the computation from Ref. [47, 55] (\mathcal{B} set in Tab. 5.1) in orange. The solid lines represent the central value of the J -factors while the shaded regions correspond to the 1σ standard deviation.	53
251	Figure 5.17 Comparisons between the J -factors versus the angular radius for the computation of J factors from Ref. [53] (\mathcal{GS} set in Tab. 5.1) in blue and for the computation from Ref. [47, 55] (\mathcal{B} set in Tab. 5.1) in orange. The solid lines represent the central value of the J -factors while the shaded regions correspond to the 1σ standard deviation.	54
256	Figure 6.1 Difference between spectral hypotheses from PPPC [44] and HDM [64]. Shown is the expected DM annihilation spectrum for $\chi\chi \rightarrow W^-W^+$. Solid lines are spectral models with EW corrections from the PPPC. Dash-dot lines are spectral models from HDM. Red lines are models for $M_\chi = 1$ TeV. Blue lines represent models for $M_\chi = 100$ TeV.	59
261	Figure 6.2 Photon spectra for $\chi\chi \rightarrow \gamma\gamma$ (left) and $\chi\chi \rightarrow ZZ$ (right) after gaussian convolution of line features. Both spectra have δ -features at photon energies equal to the DM mass. Bluer lines are annihilation spectra with lower DM mass. Redder lines are spectra from larger DM mass. All Spectral models are sourced from the Heavy Dark Matter models [64]. Axes are drawn roughly according to the energy sensitivity of HAWC.	60
267	Figure 6.3 $\frac{dJ}{d\Omega}$ maps for Coma Berenices, Draco, Segue1, and Sextans. Columns are divided for the $\pm 1\sigma$ uncertainties in $dJ/d\Omega$ around the mean value from \mathcal{LS} [65]. Origin is centered on the specific dwarf spheroidal galaxies (dSph). θ and ϕ axes are the angular separation from the center of the dwarf	61
271	Figure 6.4 Infographic on how jobs and DM computation was organized in Section 5.3. Jobs were built for each permutation of CHANS and SOURCES shown by the left block in the figure. Each job, which took on the order 2 hrs to compute, had the following work flow: 1. Import HAWC analysis software, 2 min to run. 2. Load HAWC count maps, 5 min to run. 3. Load HAWC energy and spatial resolutions, 4 min. 5. Load DM spatial source templates and spectral models, less than 1 s. 6. Perform likelihood fit on data and model, about 8 min per DM mass. 7. Write results to file, less than 1s.	63

279	Figure 6.5	Graphic of Gustafson parallel coding pattern. f_s is the fraction of a program, in time, spent on serial computation. f_p is the fraction of computing time that is parallelizable. T_p is the total time for a parallel program to run. T_1 is the total time for a parallel program to run if only 1 processor is allocated. P_N is the N -th processor where it's row is the computation the processor performs. The Gustafson pattern is most similar to what is implemented for this analysis. Figure is pulled from [67].	64
286	Figure 6.6	Task chart for one multi-threaded job developed for this project. Green blocks indicate a shared resource across the threads AND computation performed serially. Red blocks indicate functional parallel processing within each thread. 3 threads are represented here, yet many more can be employed during the full analysis. Jobs are defined by the SOURCE as these require unique maps to be loaded into the likelihood estimator. The m_χ , CHAN, and $\langle\sigma v\rangle$ variables are entered into the thread pool and allocated as evenly as possible across the threads.	66
294	Figure 6.7	HAWC upper limits at 95% confidence level on $\langle\sigma v\rangle$ versus DM mass for $\chi\chi \rightarrow b\bar{b}, t\bar{t}, u\bar{u}, d\bar{d}, s\bar{s}, c\bar{c}, gg, W^+W^-$, and hh . Limits are with \mathcal{LS} J - factors [65]. The solid line represents the observed combined limit. Dashed lines represent limits from individual dSphs.	69
298	Figure 6.8	HAWC upper limits at 95% confidence level on $\langle\sigma v\rangle$ versus DM mass for $\chi\chi \rightarrow \nu_e\bar{\nu}_e, \nu_\mu\bar{\nu}_\mu, \nu_\tau\bar{\nu}_\tau, e\bar{e}, \mu\bar{\mu}, \tau\bar{\tau}, \gamma\gamma$ and ZZ . Limits use \mathcal{LS} J factors [65]. The solid line represents the observed combined limit. Dashed lines represent limits from individual dSphs.	70
302	Figure 6.9	HAWC TS values for best fit $\langle\sigma v\rangle$ versus m_χ for SM annihilation channels: $\chi\chi \rightarrow b\bar{b}, t\bar{t}, u\bar{u}, d\bar{d}, s\bar{s}, c\bar{c}, gg, W^+W^-$, and hh . Limits use \mathcal{LS} J factors. The solid black line shows the combined best fit TS values. The colored, dashed lines are the TS values from each dSph.	71
306	Figure 6.10	HAWC TS values for best fit $\langle\sigma v\rangle$ versus m_χ for SM annihilation channels: $\chi\chi \rightarrow \nu_e\bar{\nu}_e, \nu_\mu\bar{\nu}_\mu, \nu_\tau\bar{\nu}_\tau, e\bar{e}, \mu\bar{\mu}, \tau\bar{\tau}, \gamma\gamma$ and ZZ . Limits use \mathcal{LS} J factors. The solid black line shows the combined best fit TS values. The colored, dashed lines are the TS values from each dSph.	72
310	Figure 6.11	Comparison of HAWC limits from this analysis to Glory Duck (Fig. 5.5) for 3 dSphs and 3 SM annihilation channels: $b\bar{b}, \tau\bar{\tau}$, and $e\bar{e}$. Each sector shows the 95% confidence limit from Glory Duck (blue line) and this analysis (orange line) in the top plot. The lower plot features the ratio in log scale of Glory Duck to this analysis in a red solid line. Horizontal dashed lines are for ratios of 1.0 (black) and $\sqrt{2}$ (blue). Ratios larger than 1.0 are for limits smaller, or stricter, than Glory Duck. Ratios larger than $\sqrt{2}$ indicates limits are stricter than a simple doubling of the Glory Duck data.	74

318	Figure A.1 Sister figure to Figure 5.3. Sources in the first row from left to right: Bootes 319 I, Canes Venatici I, II. In second row: Draco, Hercules, Leo I. In the first row: 320 Leo II, Leo IV, Sextans. In the final row: Ursa Major I, Ursa Major II.	77
321	Figure B.1 Sister figure to Figure 6.2 for remaining SM primary annihilation channels 322 studied for this thesis. These did not require any post generation smoothing 323 and so are directly pulled from [64] with a binning scheme most helpful for a 324 HAWC analysis.	78
325	Figure B.2 TODO: fill this out	88
326	Figure B.3 TODO: fill this out	89
327	Figure B.4 TODO: fill this out	90

LIST OF ABBREVIATIONS

- 329 **MSU** Michigan State University
330 **LANL** Los Alamos National Laboratory
331 **DM** Dark Matter
332 **SM** Standard Model
333 **HAWC** High Altitude Water Cherenkov Observatory
334 **dSph** Dwarf Spheroidal Galaxy

335

CHAPTER 1

INTRODUCTION

336 Is the text not rendering right? Ah ok it knows im basically drafting the doc still

CHAPTER 2

337

DARK MATTER IN THE COSMOS

338 **2.1 Introduction**

339 The dark matter problem can be summarized in part by the following thought experiment.

340 Let us say you are the teacher for an elementary school classroom. You take them on a field
341 trip to your local science museum and among the exhibits is one for mass and weight. The exhibit
342 has a gigantic scale, and you come up with a fun problem for your class.

343 You ask your class, "What is the total weight of the classroom? Give your best estimation to
344 me in 30 minutes, and then we'll check your guess on the scale. If your guess is within 10% of the
345 right answer, we will stop for ice cream on the way back."

346 The students are ecstatic to hear this, and they get to work. The solution is some variation of
347 the following strategy. The students should give each other their weight or best guess if they do
348 not know. Then, all they must do is add each student's weight and get a grand total for the class.
349 The measurement on the giant scale should show the true weight of the class. When comparing
350 the measured weight to your estimation, multiply the measurement by 1.0 ± 0.1 to get the $\pm 10\%$
351 tolerances for your estimation.

352 Two of your students, Sandra and Mario, return to you with a solution.

353 They say, "We weren't sure of everyone's weight. We used 65 lbs. for the people we didn't
354 know and added everyone who does know. There are 30 of us, and we got 2,000 lbs.! That's a ton!"

355 You estimated 1,900 lbs. assuming the average weight of a student in your class was 60 lbs.
356 So, you are pleased with Sandra's and Mario's answer. You instruct your students to all gather on
357 the giant scale and read off the weight together. To all your surprise, the scale reads *10,000 lbs.*!
358 10,000 is significantly more than a 10% error from 2,000. In fact, it is approximately 5 times more
359 massive than either your or your students' estimates. You think to yourself and conclude there
360 must be something wrong with the scale. You ask an employee to check the scale and verify it is
361 well calibrated. They confirm that the scale is in working order. You weigh a couple of students
362 individually to assess that the scale is well calibrated. Sandra weighs 59 lbs., and Mario weighs

363 62 lbs., typical weights for their age. You then weigh each student individually and see that their
364 weights individually do not deviate greatly from 60 lbs. So, where does all the extra weight come
365 from?

366 This thought experiment serves as an analogy to the Dark Matter problem. The important
367 substitution to make however is to replace the students with stars and the classroom with a galaxy,
368 say the Milky Way. Individually the mass of stars is well measured and defined with the Sun as our
369 nearest test case. However, when we set out to measure the mass of a collection of stars as large as
370 galaxies, our well-motivated estimation is wildly incorrect. There simply is no way to account for
371 this discrepancy except without some unseen, or dark, contribution to mass and matter in galaxies.
372 I set out in my thesis to narrow the possibilities of what this Dark Matter could be.

373 This chapter is organized like the following... **TODO: Text should look like ... Chapter x has**
374 **blah blah blah.**

375 **2.2 Dark Matter Basics**

376 Presently, a more compelling theory of cosmology that includes Dark Matter (DM) in order
377 to explain a variety of observations is Λ Cold Dark Matter, or Λ CDM. I present the evidence
378 supporting Λ CDM in Section 2.3 yet discuss the conclusions of the Λ CDM model here. According
379 to Λ CDM fit to observations on the Cosmic Microwave Background (CMB), DM is 26.8% of the
380 universe's current energy budget. Baryonic matter, stuff like atoms, gas, and stars, contributes to
381 4.9% of the universe's current energy budget [1, 2, 3].

382 DM is dark; it does not interact readily with light at any wavelength. DM also does not interact
383 noticeably with the other standard model forces (Strong and Weak) at a rate that is readily observed
384 [3]. DM is cold, which is to say that the average velocity of DM is below relativistic speeds [1].
385 'Hot' DM would not likely manifest the dense structures we observe like galaxies, and instead
386 would produce much more diffuse galaxies than what is observed [3, 1]. DM is old; it played a
387 critical role in the formation of the universe and the structures within it [1, 2].

388 Observations of DM have so far been only gravitational. The parameter space available to what
389 DM could be therefore is extremely broad. The broad DM parameter space is iteratively tested in

390 DM searches by supposing a hypothesis that has not yet been ruled out and performing observations
391 to test them. When the observations yield a null result, the parameter space is constrained further.
392 I present some approaches for DM searches in Section 2.4.

393 **2.3 Evidence for Dark Matter**

394 Dark Matter (DM) has been a looming problem in physics for almost 100 years. Anomalies
395 have been observed by astrophysicists in galactic dynamics as early as 1933 when Fritz Zwicky
396 noticed unusually large velocity dispersion in the Coma cluster. Zwicky's measurement was the
397 first recorded to use the Virial theorem to measure the mass fraction of visible and invisible matter
398 in celestial bodies [4]. From Zwicky in [5], "*If this would be confirmed, we would get the surprising*
399 *result that dark matter is present in much greater amount than luminous matter.*" Zwicky's and
400 others' observation did not instigate a crisis in astrophysics because the measurements did not
401 entirely conflict with their understanding of galaxies [4]. In 1978, Rubin, Ford, and Norbert
402 measured rotation curves for ten spiral galaxies [6]. Rubin et al.'s 1978 publication presented a
403 major challenge to the conventional understanding of galaxies that could no longer be dismissed by
404 measurement uncertainties. Evidence has been mounting ever since for this exotic form of matter.
405 The following subsections provide three compelling pieces of evidence in support of the existence
406 of DM.

407 **2.3.1 First Clues: Stellar Velocities**

408 Zwicky, and later Rubin, measured the stellar velocities of various galaxies to estimate their
409 virial mass. The Virial Theorem upon which these observations are interpreted is written as

$$2T + V = 0. \quad (2.1)$$

410 Where T is the kinetic energy and V is the potential energy in a self-gravitating system. The
411 classical Newton's law of gravity from stars and gas was used for gravitational potential modeled in
412 the observed galaxies:

$$V = -\frac{1}{2} \sum_i \sum_{j \neq i} \frac{m_i m_j}{r_{ij}}. \quad (2.2)$$

413 Zwicky et al. measured just the velocities of stars apparent in optical wavelengths [5]. Rubin et al.
 414 added by measuring the velocity of the hydrogen gas via the 21 cm emission line of Hydrogen [6].
 415 The velocities of the stars and gas are used to infer the total mass of galaxies and galaxy clusters
 416 via Equation (2.1). An inferred mass is obtained from the luminosity of the selected sources. The
 417 two inferences are compared to each other as a luminosity to mass ratio which typically yielded [1]

$$\frac{M}{L} \sim 400 \frac{M_{\odot}}{L_{\odot}} \quad (2.3)$$

418 M_{\odot} and L_{\odot} referring to stellar mass and stellar luminosity, respectively. These ratios clearly indicate
 419 a discrepancy in apparent light and mass from stars and gas and their velocities.

420 Rubin et al. [6] demonstrated that the discrepancy was unlikely to be an underestimation of
 421 the mass of the stars and gas. The inferred "dark" mass was up to 5 times more than the luminous
 422 mass. This dark mass also needed to extend well beyond the extent of the luminous matter.

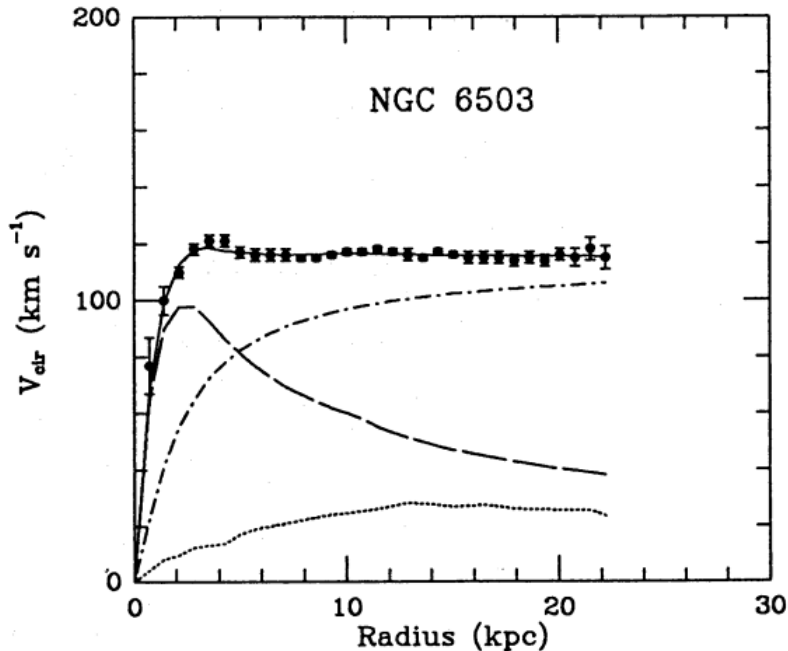


Figure 2.1 Rotation curve fit to NGC 6503 from [7]. Dashed line is the contribution from visible matter. Dotted curves are from gas. Dash-dot curves are from dark matter (DM). Solid line is the composite contribution from all matter and DM sources. Data are indicated with bold dots with error bars. Data agree strongly with a matter + DM composite prediction.

423 Figure 2.1 features one of many rotation curves plotted from the stellar velocities within galaxies.

424 The measured rotation curves mostly feature a flattening of velocities at higher radius which is not
425 expected if the gravity was only coming from gas and luminous matter. The extension of the
426 flat velocity region also indicates that the DM is distributed far from the center of the galaxy.
427 Modern velocity measurements include significantly larger objects, galactic clusters, and smaller
428 objects, dwarf galaxies. Yet, measurements along this regime are leveraging the Virial theorem
429 with Newtonian potential energies. We know Newtonian gravity is not a comprehensive description
430 of gravity. New observational techniques have been developed since 1978, and those are discussed
431 in the following sections.

432 **2.3.2 Evidence for Dark Matter: Gravitational Lensing**

433 Modern evidence for dark matter comes from new avenues beyond stellar velocities. Grav-
434 itational lensing from DM is a new channel from general relativity. General relativity predicts
435 aberrations in light caused by massive objects. In recent decades we have been able to measure the
436 lensing effects from compact objects and DM halos. Figure 2.2 shows how different massive ob-
437 jects change the final image of a faraway galaxy resulting from gravitational lensing. Gravitational
438 lensing developed our understanding of dark matter in two important ways.

439 Gravitational lensing provides additional compelling evidence for DM. The observation of two
440 merging galactic clusters in 2006, shown in Figure 2.3, provided a compelling argument for DM
441 outside the Standard Model. These clusters merged recently in astrophysical time scales. Galaxies
442 and star cluster have mostly passed by each other as the likelihood of their collision is low. Therefore,
443 these massive objects will mostly track the highest mass, dark and/or baryonic, density. Yet, the
444 intergalactic gas is responsible for the majority of the baryonic mass in the systems [4]. These gas
445 bodies will not phase through and will heat up as they collide together. The hot gas is located via
446 x-ray emission from the cluster. Two observations of the clusters were performed independently of
447 each other.

448 The first was the lensing of light around the galaxies due to their gravitational influences.
449 When celestial bodies are large enough, the gravity they exert bends space and time itself. The
450 warped space-time lenses light and will deflect in an analogous way to how glass lenses will bend

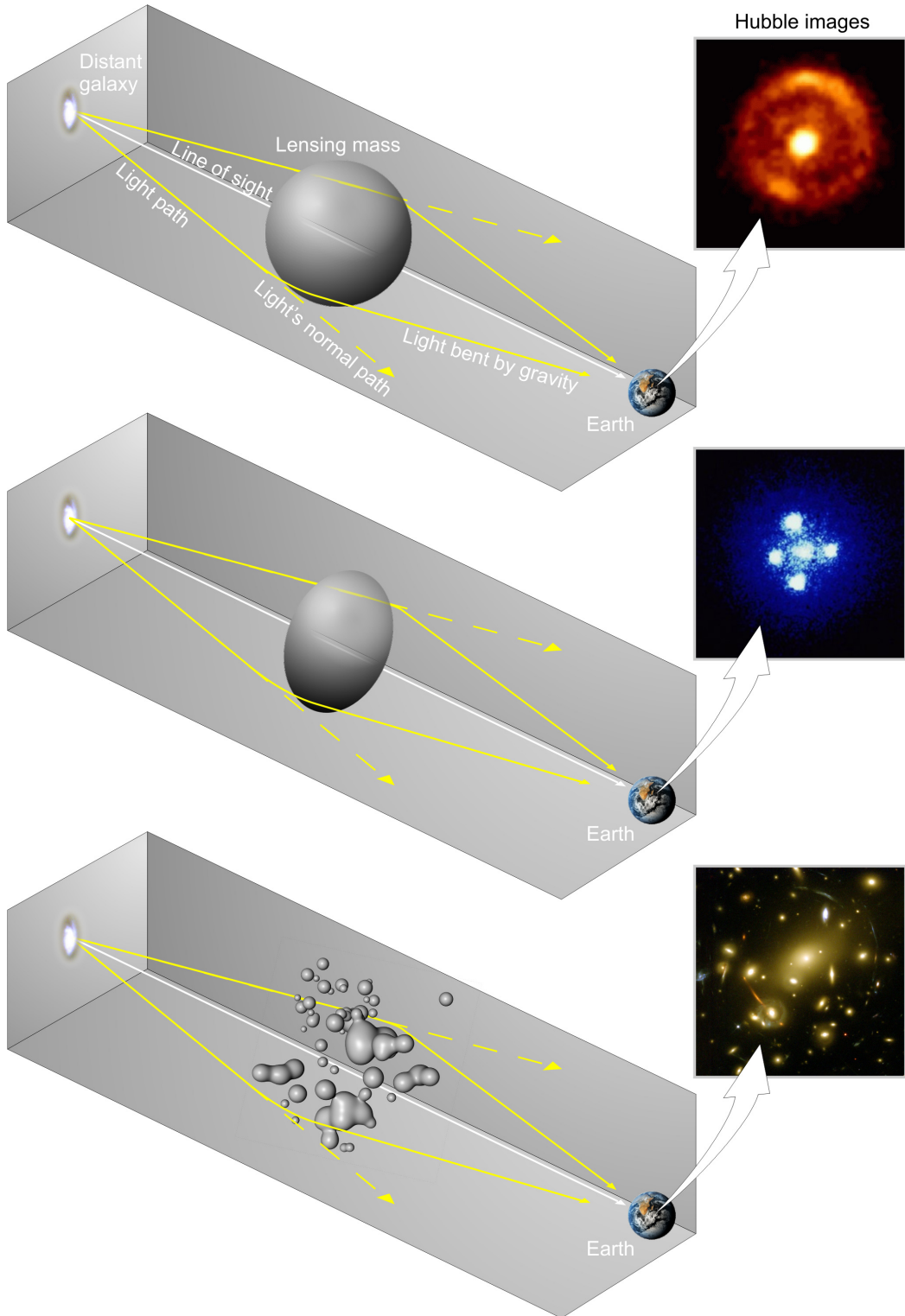


Figure 2.2 Light from distant galaxy is bent in unique ways depending on the distribution of mass between the galaxy and Earth. Yellow dashed lines indicate where the light would have gone if the matter were not present [8].

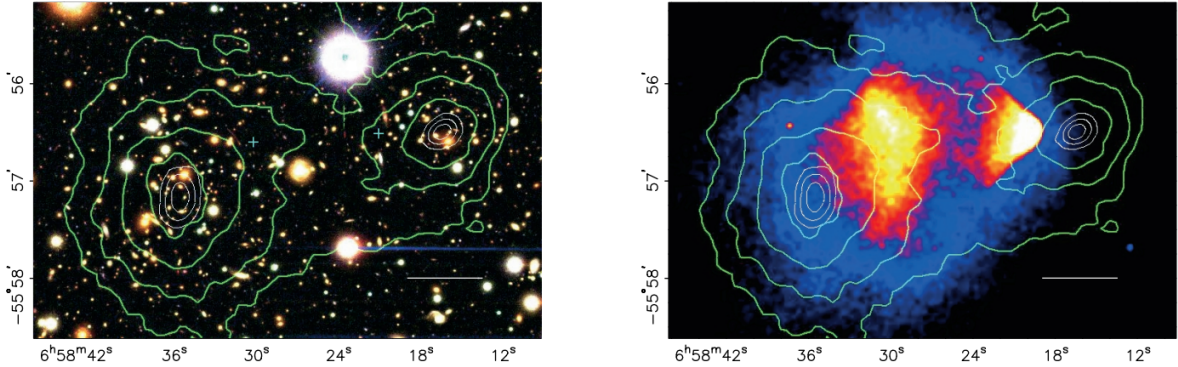


Figure 2.3 (left) Optical image of galactic cluster 1E0657-558. (right) X-ray image of the cluster with redder meaning hotter and higher baryon density. (both) Green contours are reconstruction of gravity contours from weak lensing. White rings are the best fit mass maxima at 68.3%, 95.5%, and 99.7% confidence. The matter maxima of the clusters are clearly separated from x-ray maxima. [9]

451 light, see Figure 2.2. With a sufficient understanding of light sources behind a massive object, we
 452 can reconstruct the contours of the gravitational lenses. The gradient of the contours shown in
 453 Figure 2.3 then indicates how dense the matter is and where it is.

454 The x-ray emission can then be observed from the clusters. Since these galaxies are mostly gas
 455 and are merging, then the gas should be getting hotter. If they are merging, the x-ray emissions
 456 should be the strongest where the gas is mostly moving through each other. Hence, X-ray emission
 457 maps out where the gas is in the merging galaxy cluster.

458 The lensing and x-ray observations were done on the Bullet cluster featured on Figure 2.3.
 459 The x-ray emissions do not align with the gravitational contours from lensing. The incongruence
 460 in mass density and baryon density suggests that there is a lot of matter somewhere that does
 461 not interact with light. Moreover, this dark matter cannot be baryonic [9]. The Bullet Cluster
 462 measurement did not really tell us what DM is exactly, but it did give the clue that DM also does
 463 not interact with itself very strongly. If DM did interact strongly with itself, then it would have been
 464 more aligned with the x-ray emission [9]. There have been follow-up studies of galaxy clusters with
 465 similar results. The Bullet Cluster and others like it provide a persuasive case against something
 466 possibly amiss in our gravitational theories.

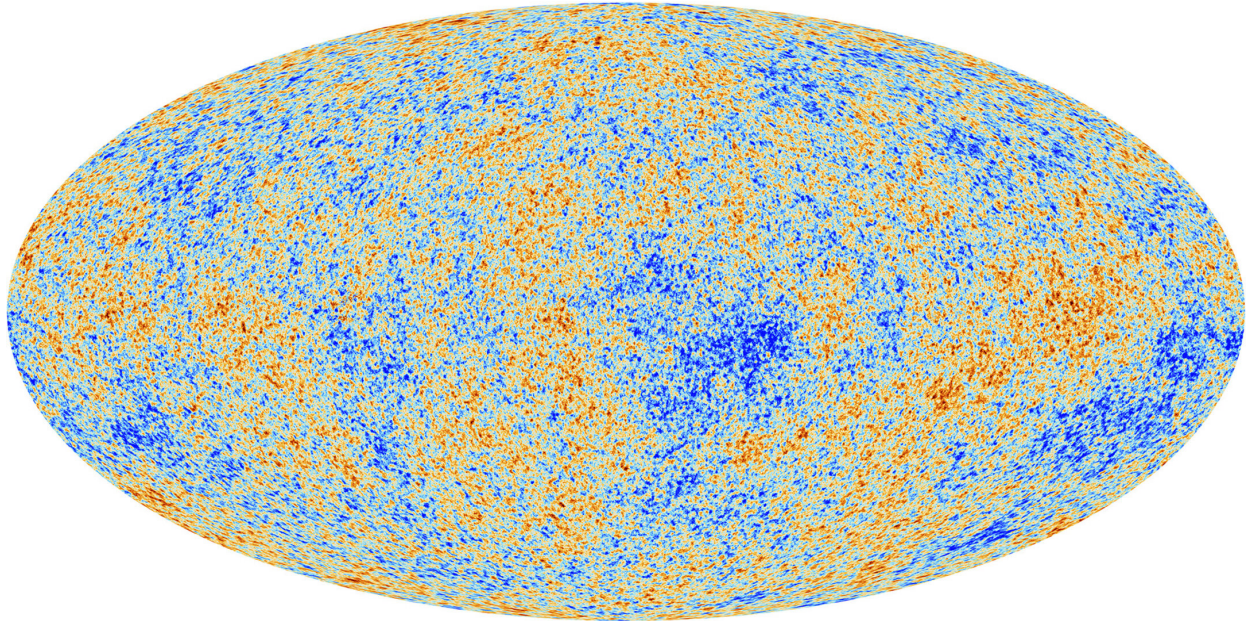


Figure 2.4 Plank CMB sky. Sky map features small variations in temperature in primordial light. These anisotropies are used to make inferences about the universe’s energy budget and developmental history. [10]

467 **2.3.3 Evidence for Dark Matter: Cosmic Microwave Background**

468 The Cosmic Microwave Background (CMB) is the primordial light from the early universe
469 when Hydrogen atoms formed from the free electron and proton soup in the early universe. The
470 CMB is the earliest light we can observe; released when the universe was about 380,000 years old.
471 Then we look at how the simulated universes look like compared to what we see. Figure 2.4 is the
472 most recent CMB image from the Plank satellite after subtracting the average value and masking the
473 galactic plane [10]. Redder regions indicate a slightly hotter region in the CMB, and blue indicates
474 colder. The intensity variations are on the order of 1 in 1000 with respect to the average value.

475 The Cosmic Microwave Background shows that the universe had DM in it from an incredibly
476 early stage. To measure the DM, Dark Energy, and matter fractions of the universe from the CMB,
477 the image is analyzed into a power spectrum, which shows the amplitude of the fluctuations as
478 a function of spherical multipole moments. Λ CDM provides the best fit to the power spectra of
479 the CMB as shown in Figure 2.5. The CMB power spectrum is quite sensitive to the fraction
480 of each energy contribution in the early universe. Low l modes are dominated by variations
481 in gravitational potential. Intermediate l emerge from oscillations in photon-baryon fluid from

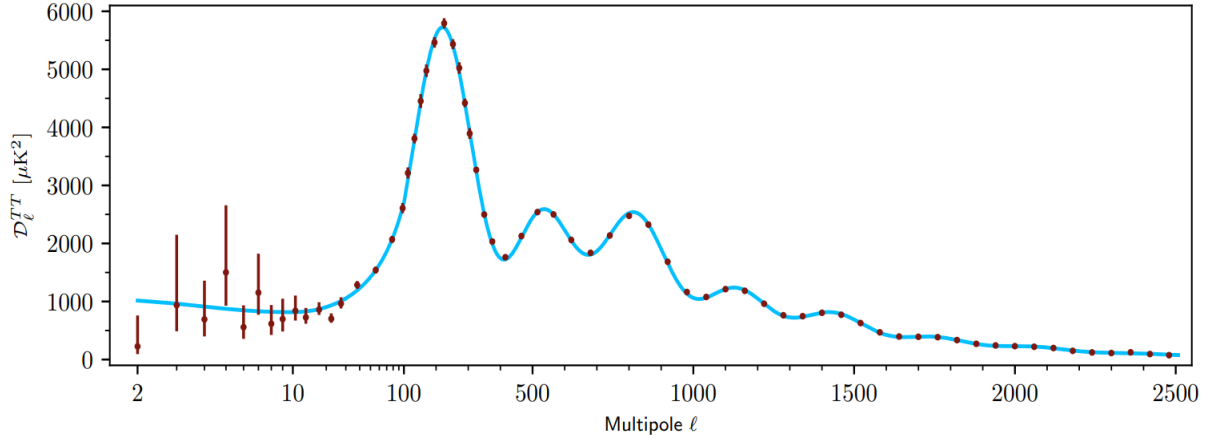


Figure 2.5 Observed Cosmic Microwave Background power spectrum as a function of multipole moment from Plank [10]. Blue line is best fit model from Λ CDM. Red points and lines are data and error, respectively.

482 competing baryon pressures and gravity. High l is a damped region from the diffusion of photons
 483 during electron-proton recombination. [1]

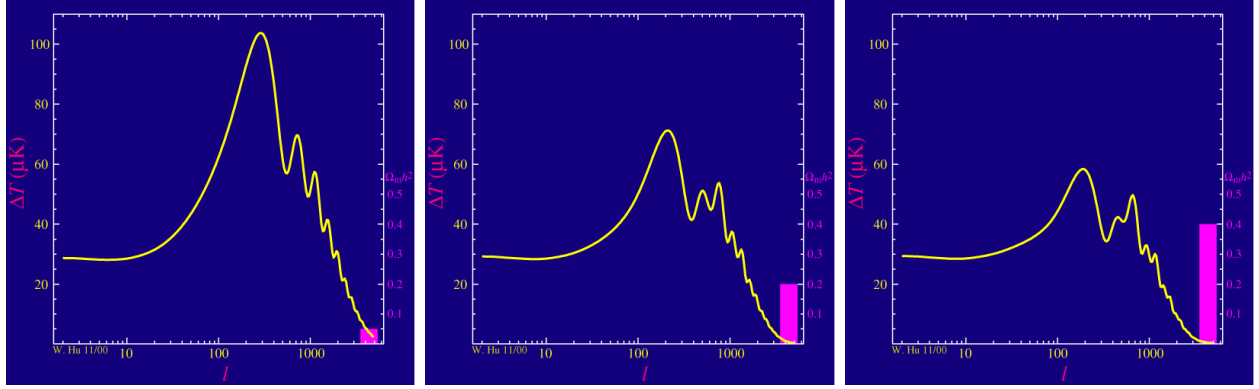


Figure 2.6 Predicted power spectra of CMB for different $\Omega_m h^2$ values for fixed baryon density from [11]. (left) Low $\Omega_m h^2$ increases the prominence of first and second peaks. (middle) $\Omega_m h^2$ is most similar to the observed power spectrum. The second and third peaks are similar in height. (right) $\Omega_m h^2$ is large which suppresses the first peak and raises the prominence of the third peak.

484 The harmonics would look quite different for a universe with less DM. Figure 2.6 demonstrates
 485 the effect $\Omega_m h^2$ has on the expected power spectrum for fixed baryon matter density. [11] Sweeping
 486 $\Omega_m h^2$ in this way clearly shows the effect dark matter has on the CMB power spectrum. The
 487 observations fit well with the Λ CDM model, and the derived fractions are as follows. The matter
 488 fraction: $\Omega_m = 0.3153$; and the baryon fraction: $\Omega_b = 0.04936$ [10]. Plank's observations also
 489 provide a measure of the Hubble constant, H_0 . H_0 especially has seen a growing tension in the

490 past decade that continues to deepened with observations from instruments like the James Webb
491 Telescope [12, 13]. As Hubble tensions deepen, we may find that perhaps Λ **CDM**, despite its
492 successes, is missing some critical physics.

493 Overall, the Newtonian motion of stars in galaxies, weak lensing from galactic clusters, and
494 power spectra from primordial light form a compelling body of research in favor of dark matter.
495 It takes another leap of theory and experimentation to make observations of DM that are non-
496 gravitational in nature. In Section 2.3, the evidence for DM implies strongly that the DM is matter
497 and not a lost parameter in the gravitational fields between massive objects. Finally, if we take one
498 axiom: that this matter has quantum behavior, such as being described by some Bohr wavelength
499 and abiding by some fermion or boson statistics; then we arrive at particle dark matter. One particle
500 DM hypothesis is the Weakly Interacting Massive Particle (WIMP). This DM candidate theory is
501 discussed further in the next section and is the focus of this thesis.

502 2.4 Searching for Dark Matter: Particle DM

503 Section 2.4 shows the Standard Model of particle physics and is currently the most accurate
504 model for the dynamics of fundamental particles like electrons and photons. The current status
505 of the SM does not have a viable DM candidate. When looking at the standard model, we can
506 immediately exclude any charged particle because charged particles interact strongly with light.
507 Specifically, this will rule out the following charged, fundamental particles: $e, \mu, \tau, W, u, d, s, c, t, b$
508 and their corresponding antiparticles. Recalling from Section 2.2 that DM must be long-lived and
509 stable over the age of the universe which excludes all SM particles with decay half-lives at or shorter
510 than the age of the universe. The lifetime constraint additionally eliminates the Z and H bosons.
511 Finally, the candidate DM needs to be somewhat massive. Recall from Section 2.2 that DM is cold
512 or not relativistic through the universe. This eliminates the remaining SM particles: $\nu_{e,\mu,\tau}, g, \gamma$ as
513 DM candidates. Because there are no DM candidates within the SM, the DM problem strongly
514 hints to physics beyond the SM (BSM).

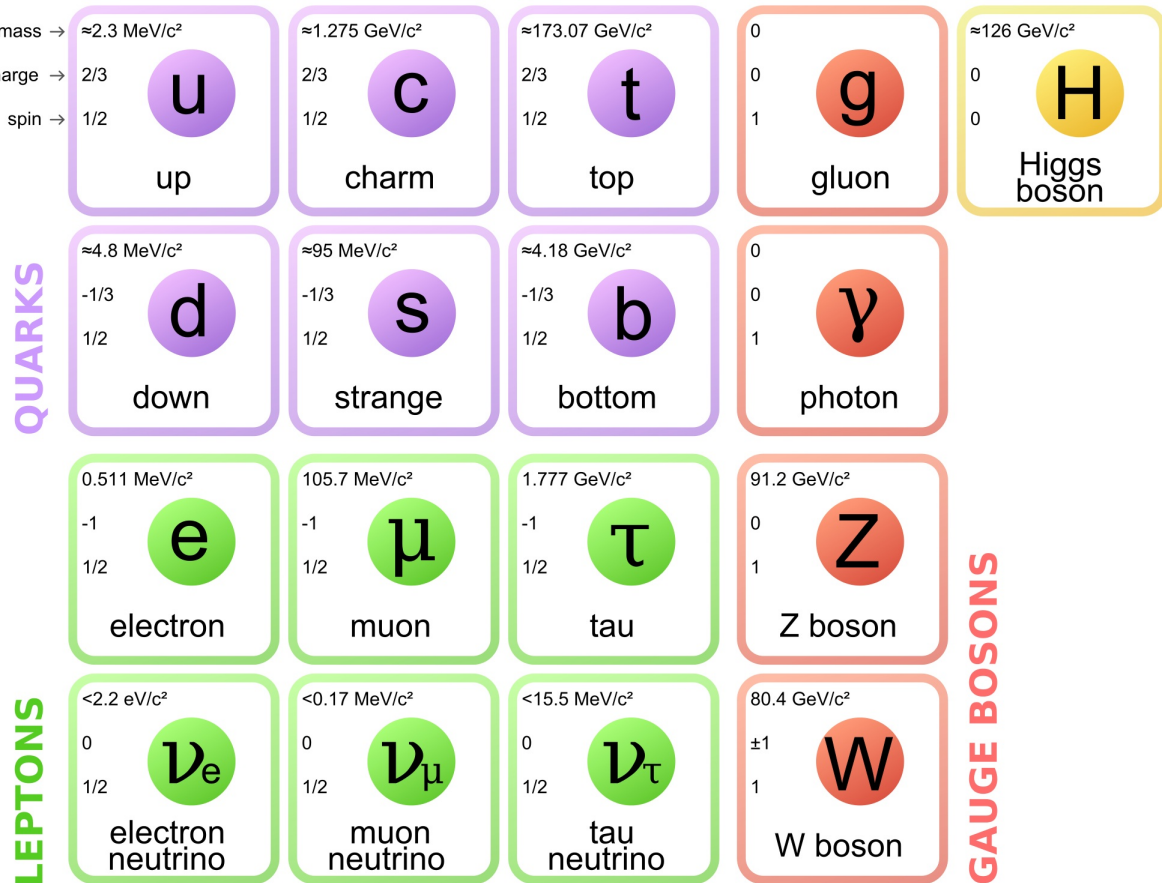


Figure 2.7 The Standard Model (SM) of particle physics. Figure taken from <http://www.quantumdiaries.org/2014/03/14/the-standard-model-a-beautiful-but-flawed-theory/>

515 2.4.1 Shake it, Break it, Make it

516 When considering DM that couples in some way with the SM, the interactions are roughly
 517 demonstrated by interaction demonstrated in Figure 2.8. The figure is a simplified Feynman
 518 diagram where the arrow of time represents the interaction modes of: **Shake it, Break it, Make it**.

519 **Shake it** refers to the direct detection of dark matter. Direct detection interactions start with
 520 a free DM particle and an SM particle. The DM and SM interact via elastic or inelastic collision
 521 and recoil away from each other. The DM remains in the dark sector and imparts some momentum
 522 onto the SM particle. The hope is that the momentum imparted onto the SM particle is sufficiently
 523 high enough to pick up with extremely sensitive instruments. Because we cannot create the DM in
 524 the lab, a direct detection experiment must wait until DM is incident on the detector. Most direct
 525 detection experiments are therefore placed in low-background environments with inert detection

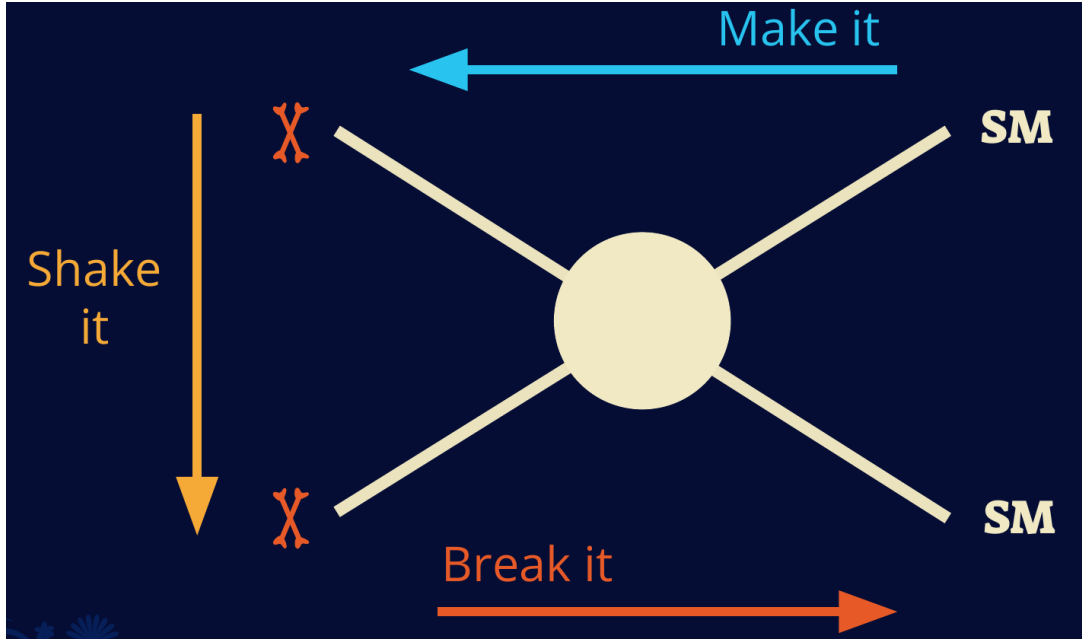


Figure 2.8 Simplified Feynman diagram demonstrating different ways DM can interact with SM particles. The 'X's refer to the DM particles whereas the SM refer to fundamental particles in the SM. The large circle in the center indicates the vertex of interaction and is purposely left vague. The colored arrows refer to different directions of time as well as their respective labels. The arrows indicate the initial and final state of the DM -SM interaction in time.

526 media like the noble gas Xenon. [14]

527 **Make it** refers to the production of DM from SM initial states. The experiment starts with
 528 particles in the SM. These SM particles are accelerated to incredibly high energies and then collide
 529 with each other. In the confluence of energy, DM hopefully emerges as a byproduct of the SM
 530 annihilation. Often it is the collider experiments that are energetic enough to hypothetically produce
 531 DM. These experiments include the world-wide collaborations ATLAS and CMS at CERN where
 532 proton collide together at extreme energies. The DM searches, however, are complex. DM likely
 533 does not interact with the detectors and lives long enough to escape the detection apparatus of
 534 CERN's colliders. This means any DM production experiment searches for an excess of events
 535 with missing momentum or energy in the events. An example event with missing transverse
 536 momentum is shown in Figure 2.9. The missing momentum with no particle tracks implies a
 537 neutral particle carried the energy out of the detector. However, there are other neutral particles
 538 in the SM, like neutrons or neutrinos, so any analysis has to account for SM signatures of missing

539 momentum. [15]

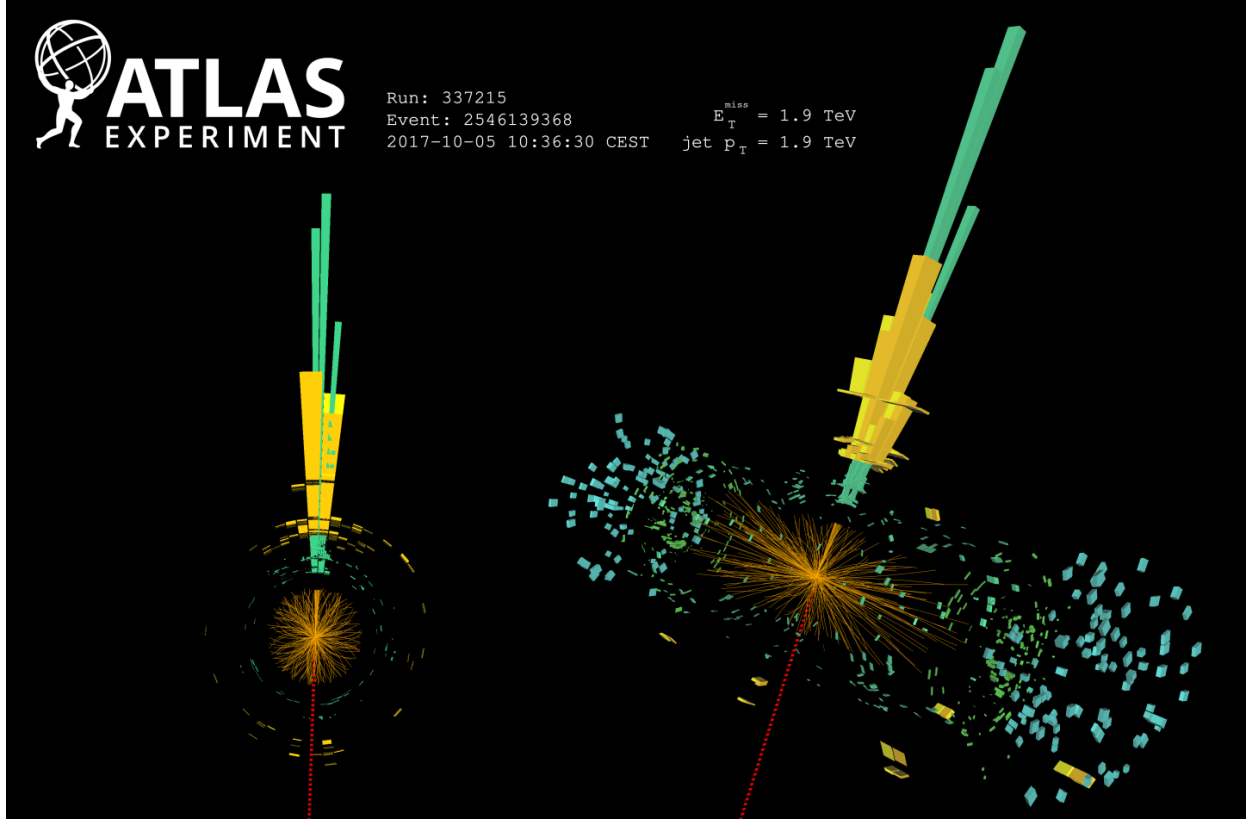


Figure 2.9 A single jet event in ATLAS detector from 2017 [16]. Jet momentum was observed to be 1.9 TeV. Missing transverse momentum was observed to be 1.9 TeV compared to the initial transverse momentum of the event was 0. Implied MET is traced by a red dashed line in event display.

540 2.4.2 Break it: Standard Model Signatures of Dark Matter through Indirect Searches

541 **Break it** refers to the creation of SM particles from the dark sector, and it is the primary focus
542 of this thesis. The interaction begins with DM or in the dark sector. The hypothesis is that this
543 DM will either annihilate with itself or decay and produce an SM byproduct. This method is
544 often referred to as the Indirect Detection of DM because we have no lab to directly control or
545 manipulate the DM. Therefore, most indirect DM searches are performed using observations of
546 known DM densities among the astrophysical sources. The strength is that we have the whole of the
547 universe and its 13.6-billion-year lifespan to use as a detector and particle accelerator. Additionally,
548 locations of dark matter are well cataloged since it was astrophysical observations that presented

549 the problem of DM in the first place.

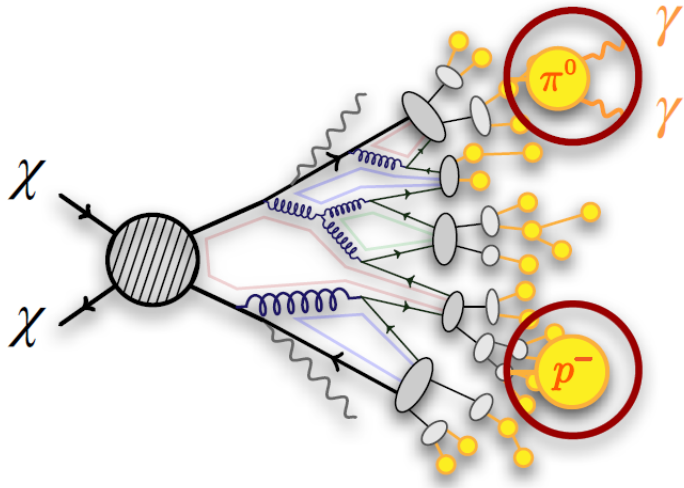


Figure 2.10 More detailed pseudo-Feynman diagram of particle cascade from dark matter annihilation into 2 quarks. The quarks hadronize and down to stable particles like γ or the anti-proton (p^-). Diagram pulled from ICRC 2021 presentation on DM annihilation search [17].

550 However, anything can happen in the universe. There are many difficult to deconvolve back-
551 grounds when searching for DM. One prominent example is the galactic center. We know the
552 galactic center has a large DM content because of stellar kinematics in our Milky Way and DM halo
553 simulations. Yet, any signal from the galactic center is challenging to parse apart from the extreme
554 environment of our supermassive black hole, unresolved sources, and diffuse emission from the
555 interstellar medium [18]. Despite the challenges, any DM model that yields evidence in the other
556 two observation methods, **Shake it or Make it** must be corroborated with indirect observations of
557 the known DM sources. Without corroborating evidence, DM observation in the lab is hard-pressed
558 to demonstrate that it is the model contributing to the DM seen at the universal scale.

559 In the case of WIMP DM, signals are described in terms of primary SM particles produced
560 from DM decay or annihilation. The SM initial state particles are then simulated down to stable
561 final states such as the γ , ν , p , or e which can traverse galactic lengths to reach Earth.

562 Figure 2.10 shows the quagmire of SM particles that emerges from SM initial states that are not
563 stable [17]. There are many SM particles with varying energies that can be produced in such an

564 interaction. For any arbitrary DM source and stable SM particle, the SM flux from DM annihilating
 565 to a neutral particle in the SM, ϕ , from a region in the sky is described by the following.

$$\frac{d\Phi_\phi}{dE_\phi} = \frac{\langle\sigma v\rangle}{8\pi m_\chi^2} \frac{dN_\phi}{dE_\phi} \times \int_{\text{source}} d\Omega \int_{l.o.s} \rho_\chi^2 dl(r, \theta') \quad (2.4)$$

566 In Equation (5.1), $\langle\sigma v\rangle$ is the velocity-weighted annihilation cross-section of DM to the SM. m_χ
 567 refers to the mass of DM, noted with Greek letter χ . $\frac{dN_\phi}{dE_\phi}$ is the N particle flux weighted by the
 568 particle energy. An example is provided in Figure 2.11 for the γ final state. The integrated terms
 569 are performed over the solid angle, $d\Omega$, and line of sight, l.o.s. ρ is the density of DM for a
 570 location (r, θ') in the sky. The terms left of the '×' are often referred to as the particle physics
 571 component. The terms on the right are referred to as the astrophysical component. For decaying
 572 DM, the equation changes to...

$$\frac{d\Phi_\phi}{dE_\phi} = \frac{1}{4\pi\tau m_\chi} \frac{dN_\phi}{dE_\phi} \times \int_{\text{source}} d\Omega \int_{l.o.s} \rho_\chi dl(r, \theta') \quad (2.5)$$

573 In Equation (6.1), τ is the decay lifetime of the DM. Just as in Equation (5.1), the left and right
 574 terms are the particle physics and the astrophysical components respectively. The integrated
 575 astrophysical component of Equation (5.1) is often called the J-Factor. Whereas the integrated
 576 astrophysical component of Equation (6.1) is often called the D-Factor.

577 Exact DM $\text{DM} \rightarrow \text{SM SM}$ branching ratios are not known, so it is usually assumed to go 100%
 578 into an SM particle/anti-particle. Additionally, when a DM annihilation or decay produces one of
 579 the neutral, long-lived SM particles (ν or γ), the particle is traced back to a DM source. For DM
 580 above GeV energies, there are very few SM processes that can produce particles with such a high
 581 energy. Seeing such a signal would almost certainly be an indication of the presence of dark matter.
 582 Fortunately, the universe provides us with the largest volume and lifetime ever for a particle physics
 583 experiment.

584 2.5 Sources for Indirect Dark Matter Searches

585 The first detection of DM relied on optical observations. Since then, we have developed new
 586 techniques to find DM dense regions. As described in Section 2.3.1, many DM dense regions were
 587 through observing galactic rotation curves. Our Milky Way galaxy is among DM dense regions

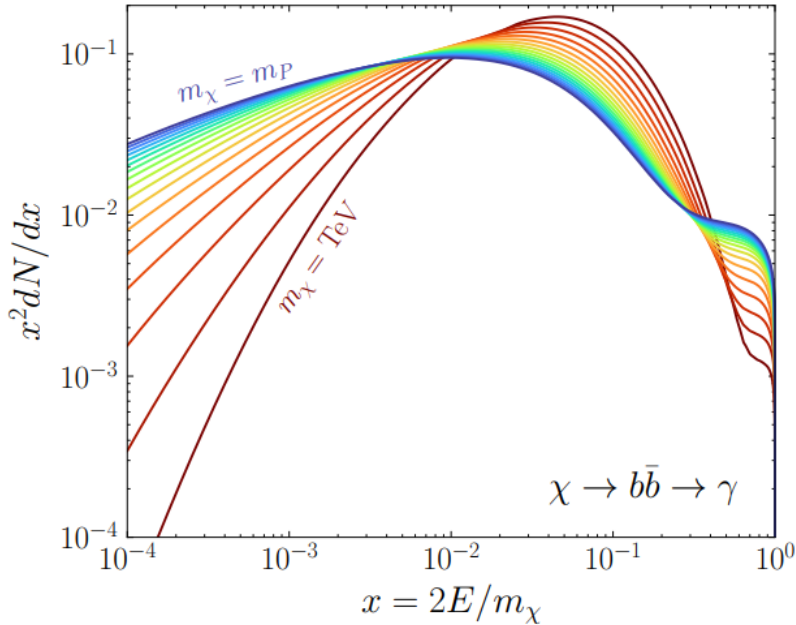


Figure 2.11 Dark Matter (DM) decay spectrum for $b\bar{b}$ initial state and γ final state. Redder spectra are for larger DM masses. Bluer spectra are light DM masses. x is a unitless factor defined as the ratio of the mass of DM, m_χ , and the final state particle energy E_γ . Figure from [19].

discovered, and it is the largest nearby DM dense region to look at. Additionally, the DM halo surrounding the Milky Way is clumpy [18]. There are regions in the DM halo of the Milky Way that have more DM than others that have captured gas over time. These sub-halos were dense enough collapse gas and form stars. These apparent sub galaxies are known as dwarf spheroidal galaxies and are the main sources studied in this thesis. Each source type comes with different trade-offs. Galactic Center studies will be very sensitive to the assumed distribution of DM. The central DM density can vary substantially as demonstrated in Figure 2.12. At distances close to the center of the galaxy, or small r , the differences in DM densities can be 3-4 orders of magnitude. Searches toward the galactic center will therefore be quite sensitive to the assumed DM distribution.

Searches toward Dwarf Spheroidal Galaxies (dSph's) suffer from uncertainties in the DM density less than the galactic center studies. This is mostly from their diminutive size being smaller than the angular resolution of most γ -ray observatories [18]. The DM content dSph's are typically determined with the Virial theorem, Equation (2.1), and are usually majority DM [18] in mass. DSph's tend to be ideal sources to look at for DM searches. Their environments are quiet with little

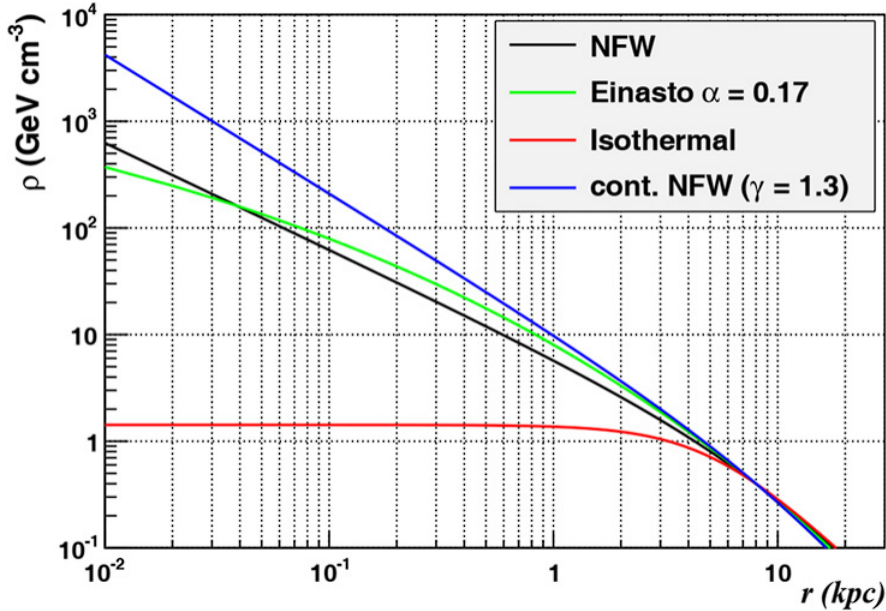


Figure 2.12 Different dark matter density profiles compared. Some models produce exceptionally large densities at small r [20].

602 astrophysical background. Unlike the galactic center, the most active components of dSph's are the
 603 stars within them versus a violent accretion disc around a black hole. All this together means that
 604 dSph's are among the best sources to look at for indirect DM searches. dSph's are the targets of
 605 focus for this thesis.

606 2.6 Multi-Messenger Dark Matter

607 Astrophysics entered a new phase in the past few decades that leverages our increasing sensitivity
 608 to SM channels and general relativity (GR). Up until the 21st century, astrophysical observations
 609 were performed with photons (γ) only. Astrophysics with this 'messenger' is fairly mature now.
 610 Novel observations of the universe have since only adjusted the sensitivity of the wavelength of
 611 light that is observed except at MeV energies. Gems like the CMB [10], and more have ultimately
 612 been observations of different wavelengths of light. Multi-messenger astrophysics proposes using
 613 other SM particles such the p^{+-} , or ν or gravitation waves predicted by general relativity.

614 The experiment LIGO had a revolutionary discovery in 2016 with the first detection of a binary
 615 black hole merger [21]. This opened the collective imagination to observing the universe through
 616 gravitational waves. There has also been a surge of interest in the neutrino (ν) sector. IceCube

617 demonstrated that we are sensitive to neutrinos in regions that correlate with significant photon
 618 emission like the galactic plane [22]. Neutrinos, like gravitational waves and light, travel mostly
 619 unimpeded from their source to our observatories. This makes pointing to the originating source
 620 of these messengers much easier than it is for cosmic rays which are deflected from their source by
 621 magnetic fields.

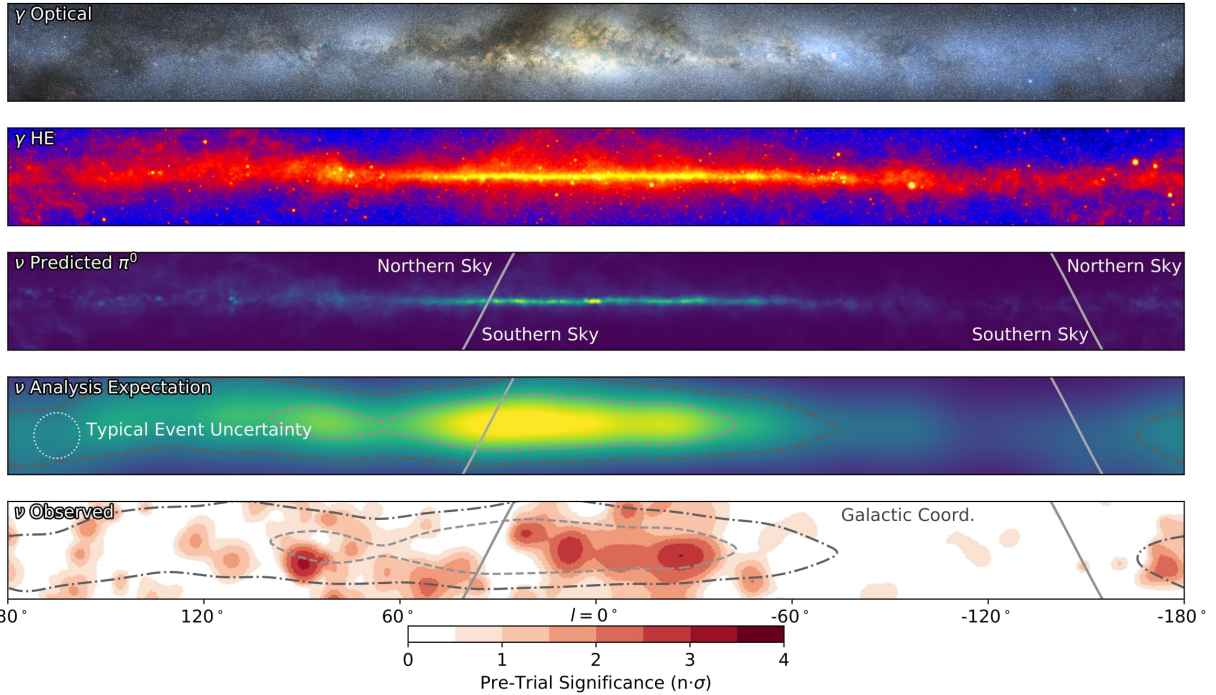


Figure 2.13 The Milky Way Galaxy in photons (γ) and neutrinos (ν) [22]. The Galactic center is at $l=0^\circ$ and is the brightest region in all panels. (top) An Optical color image of the Milky Way galaxy seen from Earth. Clouds of gas and dust obscure some light from stars. (2nd down) Integrated flux of γ -rays observed by the Fermi-LAT telescope [23]. (middle) Expected neutrino emission that corresponds with Fermi-LAT observations. (2nd up) Expected neutrino emission profile after considering detector systematics of IceCube. (bottom) Observed neutrino emission from region of the galactic plane. Substantial neutrino emission was detected.

622 The IceCube collaboration recently published a groundbreaking result of the Milky Way in
 623 neutrinos. The recent result from IceCube, shown in Figure 2.13, proves that we can make
 624 observations under different messenger regimes. The top two panels show the appearance of the
 625 galactic plane to different wavelengths of light. Some sources are more apparent in some panels,
 626 while others are not. This new channel is powerful because neutrinos are readily able to penetrate
 627 through gas and dust in the Milky Way. This new image also refines our understanding of how high

628 energy particles are produced. For example, the fit to IceCube data prefers neutrino production
 629 from the decay of π^0 [22].

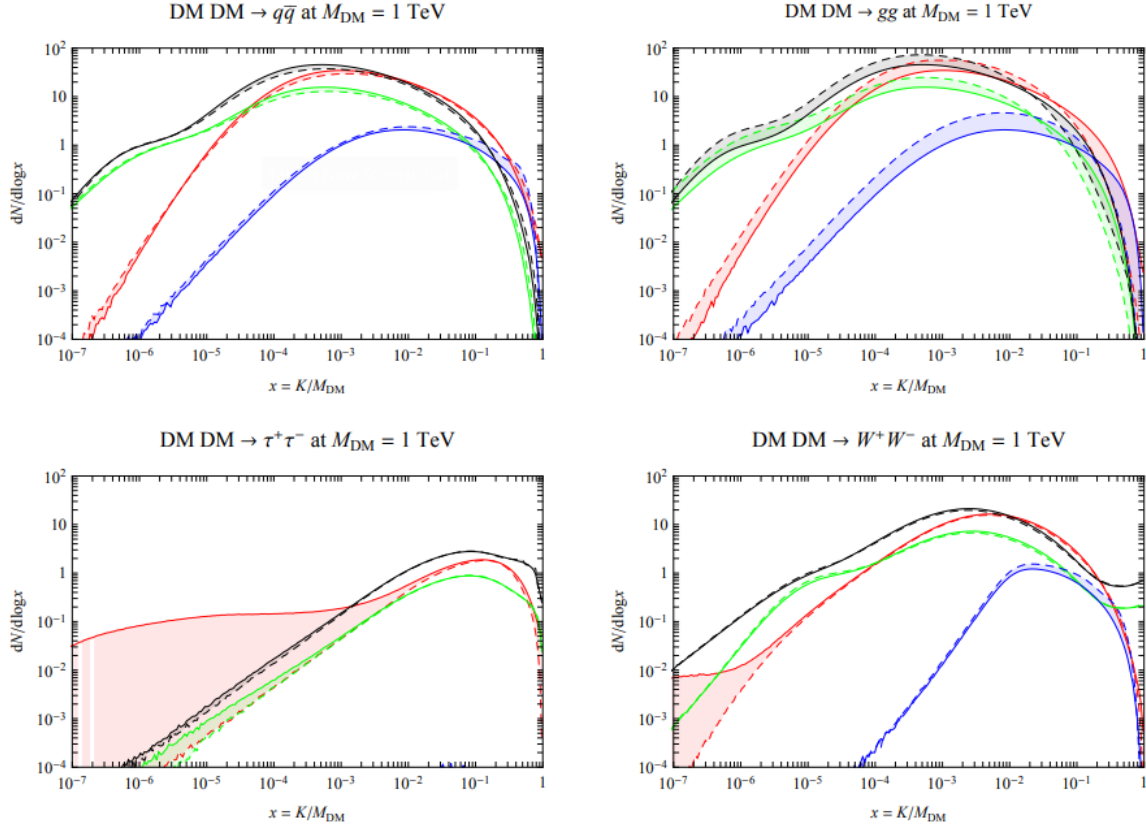


Figure 2.14 Dark Matter annihilation spectra for different final state particle and standard model annihilation channels [24]. Photons (red), e^\pm (green), \bar{p} (blue), ν (black).

630 Exposing our observations to more cosmic messengers greatly increases our sensitivity to
 631 rare processes. In the case of DM, Figure 2.14, there are many SM particles produced in DM
 632 annihilation. Among the final state fluxes are gammas and neutrinos. Charged particles are also
 633 produced however they would not likely make it to Earth since they will be deflected by magnetic
 634 fields between the source and Earth. This means observatories that can see the neutral messengers
 635 are especially good for DM searches and for combining data for a multi-messenger DM search.

CHAPTER 3

636 **HIGH ALTITUDE WATER CHERENKOV (HAWC) OBSERVATORY**

637 **3.1 The Detector**

638 **3.2 Events Reconstruction and Data Acquisition**

639 **3.2.1 G/H Discrimination**

640 **3.2.2 Angle**

641 **3.2.3 Energy**

642 **3.3 Remote Monitoring**

643 **3.3.1 ATHENA Database**

644 **3.3.2 HOMER**

CHAPTER 4

645

ICECUBE NEUTRINO OBSERVATORY

646 **4.1 The Detector**

647 **4.2 Events Reconstruction and Data Acquisition**

648 **4.2.1 Angle**

649 **4.2.2 Energy**

650 **4.3 Northern Test Site**

651 **4.3.1 PIgeon remote dark rate testing**

652 **4.3.2 Bulkhead Construction**

CHAPTER 5

GLORY DUCK: MULTI-WAVELENGTH SEARCH FOR DARK MATTTER ANNIHILATION TOWARDS DWARF SPHEROIDAL GALAXIES

5.1 Introduction

The field of astrophysics now has several instruments and observatories sensitive to high energy gamma-rays. The energy sensitivity for the modern gamma-ray program spans many orders of magnitude. Figure 5.1 demonstrates these similar sensitivities across energies for the five experiments: Fermi-LAT, HAWC, HESS, MAGIC, and VERITAS.

Each of the five experiments featured in Figure 5.1 have independently searched for DM annihilation from dwarf spheroidal galaxies (dSph) and set limits. Intriguingly, there are regions of substantial overlap in their energy sensitivities. This clearly motivates an analysis that combines data from these five. Each experiment has unique gamma-ray detection methods and their weaknesses and strengths can be leveraged with each other. The HAWC gamma-ray observatory is extensively introduced in chapter 3, so it is not introduced here. A brief description of the remaining experiments are in the following paragraphs.

The Large Area Telescope (LAT) is a pair conversion telescope mounted on the NASA Fermi satellite in orbit \sim 550 km above the Earth [26]. LAT's field of view covers about 20% of the whole sky, and it sweeps the whole sky approximately every 3 hours. LAT's gamma-ray energy sensitivity ranges from 20 MeV up to 1 TeV. Previous DM searches towards dSphs using Fermi-LAT are published in [27] and [28]

The High Energy Spectroscopic System (HESS), Major Atmospheric Gamma Imaging Cherenkov (MAGIC), and Very Energetic Radiation Imaging Telescope Array System (VERITAS) are arrays of Imaging Atmospheric Cherenkov Telescopes (IACT). These telescopes observe the Cherenkov light emitted from gamma-ray showers in the Earth's atmosphere. The field of view for these telescopes is no larger than 5° with energy sensitivities ranging from 30 GeV up to 100 TeV [29, 30, 31]. IACTs are able to make precise observations in selected regions of the sky, however can only be operated in ideal dark conditions. HESS's observations of the dwarves

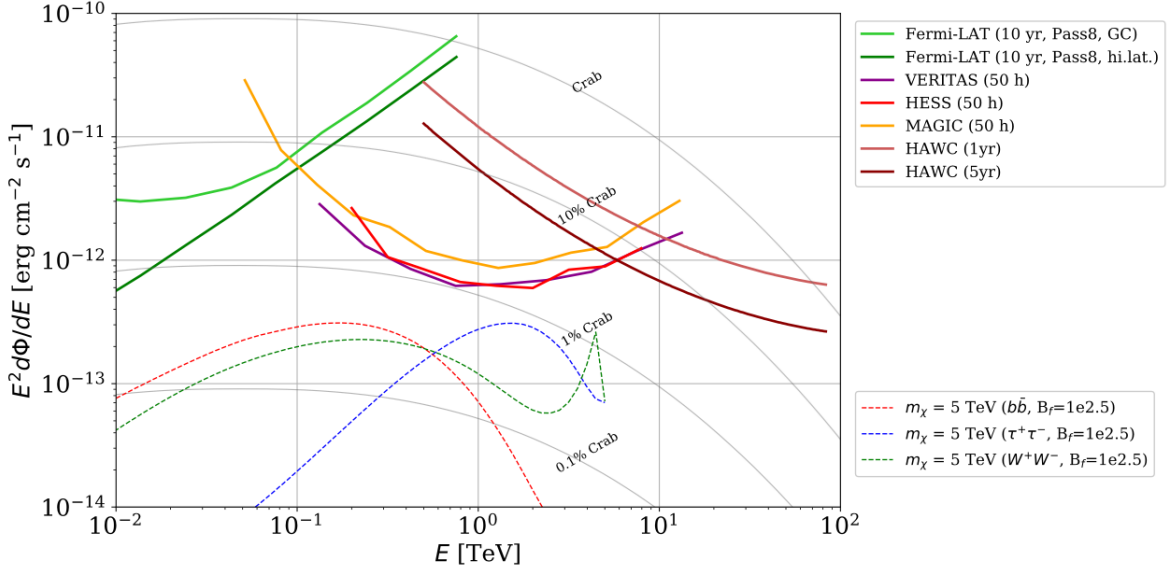


Figure 5.1 Sensitivities of five gamma-ray experiments compared to percentages of the Crab nebula’s emission and dark matter annihilation. Solid lines present estimated sensitivities to power law spectra [FACT CHECK THIS] for each experiment. Green lines are Fermi-LAT sensitivities where lighter green is the sensitivity to the galactic center and dark green is its sensitivity to higher declinations. Orange, red, and purple solid lines represent the MAGIC, HESS, and VERITAS 50 hour sensitivities respectively. The maroon and brown lines are the HAWC 1 year and 5 year sensitivities. Across four decades of gamma-ray energy, these experiments have similar sensitivities on the order 10^{-12} erg $\text{cm}^{-2}\text{s}^{-1}$. The dotted lines are estimated dark matter fluxes assuming $m_\chi = 5$ TeV DM annihilating to bottom quarks (red), tau leptons (blue), and W bosons (green). Faded gray lines outline percentage flux of the Crab nebula. Figure is an augmented version of [25]

679 Sculptor and Carina were between January 2008 and December 2009. HESS’s observations of
 680 Coma Berenices were from 2010 to 2013, and Fornax was observed in 2010 [32, 33, 34]. MAGIC
 681 provided deep observations of Segue1 between 2011 and 2013 [35]. MAGIC also provides data
 682 for three dwarves: Coma Berenices, Draco, and Ursa Major II where observations were made
 683 in: January - June 2019 [36], March - September 2018 [36], and 2014 - 2016 [37] respectively.
 684 VERITAS provided data for Boötes I, Draco, Segue 1, and Ursa Minor from 2009 to 2016 [38].

685 This chapter presents the Glory Duck analysis, the name given for the search for dark matter
 686 annihilation from dSph by combining data from the five gamma-ray observatories: Fermi-LAT,
 687 HAWC, HESS, MAGIC, and VERITAS. Specifically, the methods in analysis and modeling are
 688 presented for the HAWC gamma-ray observatory. This work was published to the Journal of
 689 Cosmology and Astroparticle Physics and presented at the International Cosmic Ray Conference

690 in 2019, 2021, and 2023 [39, 40, 41] and others.

691 **5.2 Dataset and Background**

692 This section enumerates the data and background methods used for HAWC's study of dSphs.
693 Section 5.2.1 and Section 5.2.2 are most useful for fellow HAWC collaborators looking to replicate
694 the Glory Duck analysis.

695 **5.2.1 Itemized HAWC files**

- 696 • Detector Resolution: `response_aerie_svn_27754_systematics_best_mc_test_no`
697 `broadpulse_10pctlogchargesmearing_0.63qe_25kHzNoise_run5481_curvatu`
698 `re0_index3.root`
- 699 • Data Map: `maps-20180119/liff/maptree_1024.root`
- 700 • Spectral Dictionary: `DM_CirrelliSpectrum_dict_gammas.npy`
- 701 • Analysis wiki: https://private.hawc-observatory.org/wiki/index.php/Glory_Duck_Multi-Experiment_Dark_Matter_Search

703 **5.2.2 Software Tools and Development**

704 This analysis was performed using HAL and 3ML [42, 43] in Python version 2. I built software
705 to implement the *A Poor Particle Physicist Cookbook for Dark Matter Indirect Detection* (PPPC)
706 [44] DM spectral model and dSphs spatial model from [45] for HAWC analysis. A NumPy version
707 of this dictionary was made for both Py2 and Py3. The code base for creating this dictionary is
708 linked on my GitLab sandbox:

- 709 • Py2: [Dictionary Generator \(Deprecated\)](#)
- 710 • Py3: [PPPC2Dict](#)

711 The analysis was performed using the f_{hit} framework performed in the HAWC Crab paper
712 [42]. The Python2 NumPy dictionary file for gamma-ray final states is `dmCirSpecDict.npy`. The
713 corresponding Python3 file is `DM_CirrelliSpectrum_dict_gammas.npy`. These files can also

714 be used for decay channels and the PPPC describes how [44]. All other software used for data
715 analysis, DM profile generation, and job submission to SLURM are also kept in my sandbox for
716 [the Glory Duck](#) project.

717 **5.2.3 Data Set and Background Description**

718 The HAWC data maps used for this analysis contain 1017 days of data between runs 2104
719 (2014-11-26) and 7476 (2017-12-20). They were generated from pass 4.0 reconstruction. The
720 analysis is performed using the f_{hit} energy binning scheme with bins (1-9) similar to what was done
721 for the Crab and previous HAWC dSph analysis [42, 46]. Bin 0 was excluded as it has substantial
722 hadronic contamination and poor angular resolution.

723 This analysis was done on dSphs because of their large DM mass content relative to baryonic
724 mass. We consider the following to estimate the background to this study.

- 725 • The dSphs are small in HAWC’s field of view, so the analysis is not sensitive to large or small
726 scale anisotropies.
- 727 • The dSphs used in this analysis are off the galactic plane.
- 728 • The dSphs are baryonically faint relative to their expected dark matter content and are not
729 expected to contain high energy gamma-ray sources.

730 Therefor we make no additional assumptions on the background from our sources and use
731 HAWC’s standard direct integration method for background estimation [42]. It is possible for
732 gamma rays from DM annihilation to scatter in transit to HAWC via Inverse Compton Scattering
733 (ICS). This was investigated and its impact on the flux is basically zero. Supporting information
734 on this is in Section 5.7.1

735 **5.3 Analysis**

736 The expected differential photon flux from DM-DM annihilation to standard model particles,
737 $d\Phi_\gamma/dE_\gamma$, over solid angle, Ω is described by the familiar equation.

$$\frac{d\Phi_\gamma}{dE_\gamma} = \frac{\langle\sigma v\rangle}{8\pi m_\chi^2} \frac{dN_\gamma}{dE_\gamma} \times \int_{\text{source}} d\Omega \int_{l.o.s} \rho_\chi^2 dl(r, \theta') \quad (5.1)$$

738 Where $\langle \sigma v \rangle$ is the velocity weighted annihilation cross-section. $\frac{dN}{dE}$ is the expected differential
 739 number of photons produced at each energy per annihilation. m_χ is the rest mass of the supposed
 740 DM particle. ρ_χ is the DM density. J is the astrophysical J-factor and is defined as

$$J = \int d\Omega \int_{l.o.s} dl \rho_\chi^2(r, \theta') \quad (5.2)$$

741 l is the distance to the source from Earth. r is the radial distance from the center of the source. θ' is
 742 the half angle defining a cone containing the DM source. How each component is synthesized and
 743 considered for HAWC's analysis is presented in the following sections. Section 5.3.1 presents the
 744 particle physics model for DM annihilation. Section 5.3.2 presents the spatial distributions built
 745 for each dSph.

746 5.3.1 $\frac{dN_\gamma}{dE_\gamma}$ - Particle Physics Component

747 For these spectra, we import the PPPC with Electroweak (EW) corrections [44]. The spectrum
 748 is implemented as a model script in astromodels for 3ML. The EW corrections were previously not
 749 considered for HAWC and are significant for DM annihilating to EW coupled SM particles such
 750 as all leptons, and the γ , Z , and W bosons [46]. Figure 5.2 demonstrates the significance of EW
 751 corrections for W boson annihilation. Across EW SM channels, the gamma-ray spectra become
 752 harder than spectra without EW corrections. Tables from the PPPC were reformatted into Python
 753 NumPy dictionaries for collaboration-wide use. A class in astromodels was developed to include
 754 the EW correction from the PPPC and is aptly named `PPPCSpectra` within `DM_models.py`.

755 5.3.2 J - Astrophysical Component

756 The J-factor profiles for each source are imported from Geringer-Sameth (referred to with \mathcal{GS})
 757 [45]. These were pulled from the publication as $J(\theta)$, where θ is the angular separation from the
 758 center of the source. HAWC requires maps in terms of $\frac{dJ}{d\Omega}$, so the conversion from the maps was
 759 done in the following way...

760 First, convert the angular distances to solid angles

$$\Omega = 2 \cdot \pi(1 - \cos(\theta)) \quad (5.3)$$

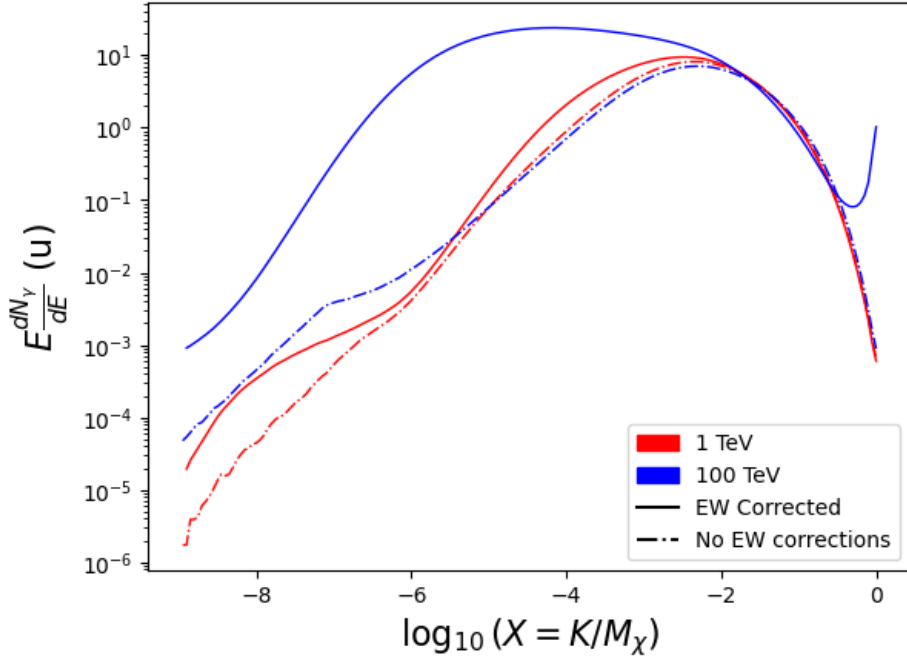


Figure 5.2 Effect of Electroweak (EW) corrections on expected DM annihilation spectrum for $\chi\chi \rightarrow W^-W^+$. Solid lines are spectral models that consider EW corrections. Dash-dot lines are spectral models without EW corrections. Red lines are models for $M_\chi = 1$ TeV. Blue lines represent models for $M_\chi = 100$ TeV. All models are sourced from the PPPC4DMID [44].

761 which reduces with a small angle approximation to $\pi\theta^2$. Next, the central difference for both the
 762 ΔJ and $\Delta\Omega$ value were calculated from the discretized $J(\theta)$ with the central difference stencil:

$$\Delta\phi_i = \phi_{i+1} - \phi_{i-1} \quad (5.4)$$

763 Where ϕ is either Ω or J . These were done separately in case the grid spacing in θ was not uniform.
 764 Finally, these lists are divided so that we are left with an approximation of the $dJ/d\Omega$ profile that
 765 is a function of θ . Admittedly, this is an approximation method for the map which introduces small
 766 errors compared to the true profile estimate. This was checked as a systematic against the author's
 767 profiling of the spatial distribution and is documented in Section 5.8.1.

768 With $\frac{dJ}{d\Omega}(\theta)$, a map is generated, first by filling in the north-east quadrant of the map. This
 769 quadrant is then reflected twice, vertically then horizontally, to fill the full map. Maps are then
 770 normalized by dividing the discrete 2D integral of the map. The 2D integral was a simple height

771 of bins, Newton’s integral:

$$p^2 \cdot \sum_{i,j=0}^{N,M} \frac{dJ}{d\Omega}(\theta_{i,j}, \phi_{i,j}) \quad (5.5)$$

772 These maps are HEALpix maps with NSIDE 16384 and saved in the `.fits` format.

773 Another DM spatial distribution model from Bonnivard (\mathcal{B}) [47] was used for the Glory Duck
774 study. However, to save computational time, limits from \mathcal{GS} were scaled to \mathcal{B} instead of each
775 experiment performing a full study a second time. How these models compare is demonstrated
776 for each dSph in Figure 5.16 and Figure 5.17 Plots of these maps are provided for each source
777 in chapter A Examples of the two most impactful dSphs derived from \mathcal{GS} , Segue1 and Coma
778 Berenices are featured in Figure 5.3

779 5.3.3 Source Selection and Annihilation Channels

780 We use many of the dSphs presented in HAWC’s previous dSph DM search [46]. HAWC’s
781 sources for Glory Duck include Boötes I, Coma Berenices, Canes Venatici I + II, Draco, Hercules,
782 Leo I, II, + IV, Segue 1, Sextans, and Ursa Major I + II. A full description of all sources used
783 in Glory Duck is found in Table 5.1. Triangulum II was excluded from the Glory Duck analysis
784 because of large uncertainties in its J factor. Ursa Minor was excluded from HAWC’s contribution
785 to the combination because the source extension model extended Ursa Minor beyond HAWC’s field
786 of view. Ursa Minor was not expected to contribute significantly to the combined limit, so work
787 was not invested in a solution to include Ursa Minor.

788 This analysis improves on the previous HAWC dSph paper [46] in the following ways. Pre-
789 viously, the dSphs were treated and implemented as point sources. For this analysis, dSphs are
790 modeled and treated as extended source. The impact of this change with respect to the upper limit
791 is source dependent and is explored in Section 5.7.2. Previously, the particle physics model used for
792 gamma-ray spectra from DM annihilation did not have EW corrections where the PPPC includes
793 them. Finally, the gamma-ray ray dataset is much larger. The study performed here analyzes over
794 1000 days of data compared to 507.

795 The SM annihilation channels probed for the Glory Duck combination include $b\bar{b}$, $e\bar{e}$, $\mu\bar{\mu}$, $\tau\bar{\tau}$,
796 $t\bar{t}$, W^+W^- , and ZZ . A summary of all sources, with a description of each experiments’ sensitivity

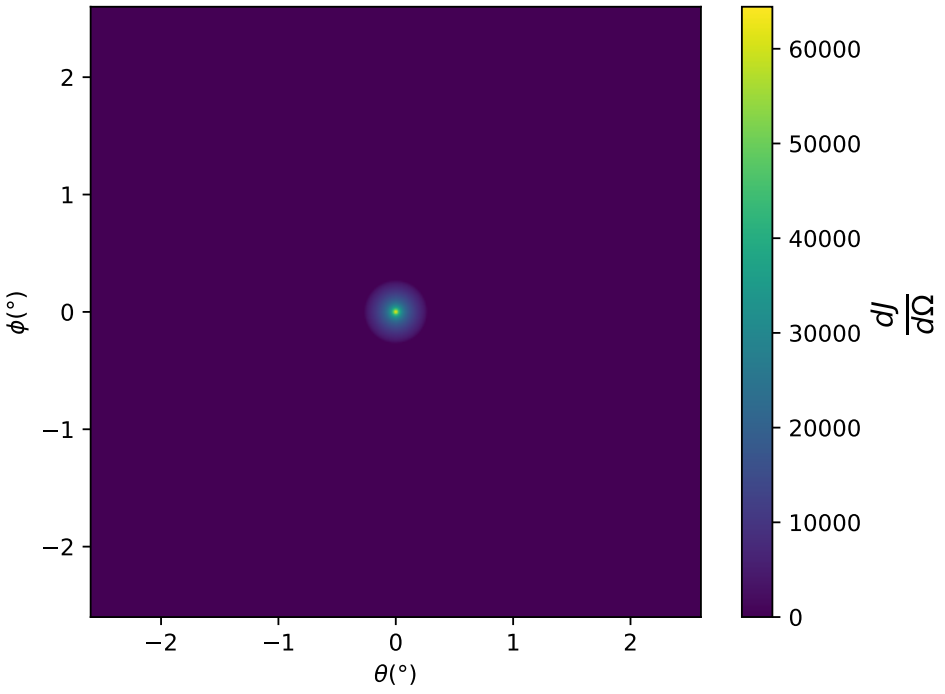
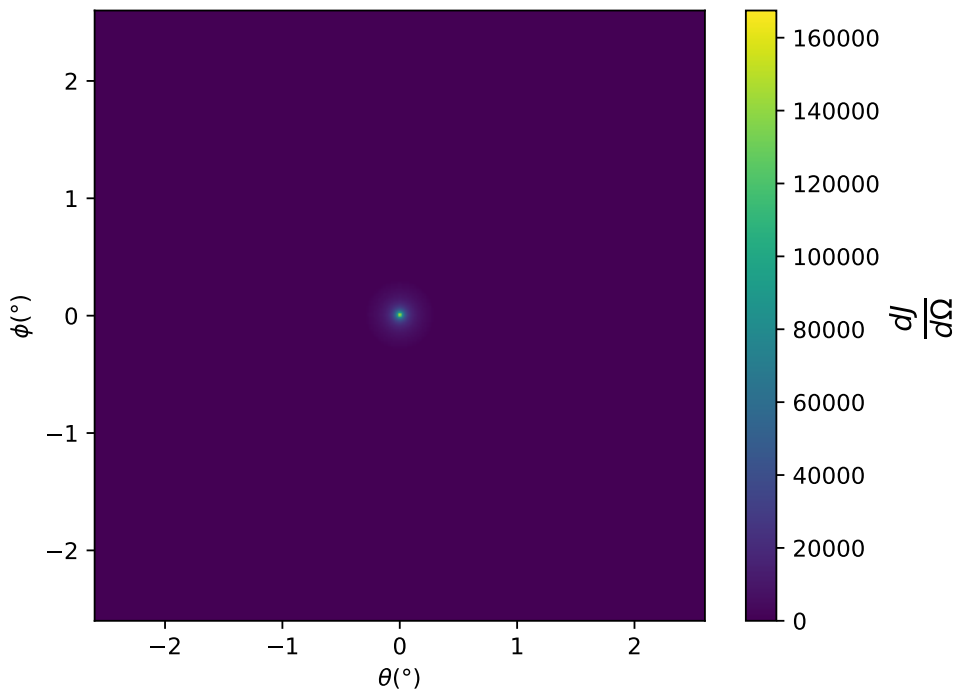


Figure 5.3 $\frac{dJ}{d\Omega}$ maps for Segue1 (top) and Coma Berenices (bottom). Origin is centered on the specific dwarf spheroidal galaxies (dSph). X and Y axes are the angular separation from the center of the dwarf. Plots of the remaining 11 dSph HAWC studied are linked in Fig. A.1.

Table 5.1 Summary of the relevant properties of the dSphs used in the present work. Column 1 lists the dSphs. Columns 2 and 3 present their heliocentric distance and galactic coordinates, respectively. Columns 4 and 5 report the J -factors of each source given from the \mathcal{GS} and \mathcal{B} independent studies and their estimated $\pm 1\sigma$ uncertainties. The values $\log_{10} J$ (\mathcal{GS} set) [45] correspond to the mean J -factor values for a source extension truncated at the outermost observed star. The values $\log_{10} J$ (\mathcal{B} set) [47] are provided for a source extension at the tidal radius of each dSph. **Bolded sources are within HAWC's field of view and provided to the Glory Duck analysis.**

Name	Distance (kpc)	l, b ($^{\circ}$)	$\log_{10} J$ (\mathcal{GS} set) $\log_{10}(\text{GeV}^2 \text{cm}^{-5} \text{sr})$	$\log_{10} J$ (\mathcal{B} set) $\log_{10}(\text{GeV}^2 \text{cm}^{-5} \text{sr})$
Boötes I	66	358.08, 69.62	$18.24^{+0.40}_{-0.37}$	$18.85^{+1.10}_{-0.61}$
Canes Venatici I	218	74.31, 79.82	$17.44^{+0.37}_{-0.28}$	$17.63^{+0.50}_{-0.20}$
Canes Venatici II	160	113.58, 82.70	$17.65^{+0.45}_{-0.43}$	$18.67^{+1.54}_{-0.97}$
Carina	105	260.11, -22.22	$17.92^{+0.19}_{-0.11}$	$18.02^{+0.36}_{-0.15}$
Coma Berenices	44	241.89, 83.61	$19.02^{+0.37}_{-0.41}$	$20.13^{+1.56}_{-1.08}$
Draco	76	86.37, 34.72	$19.05^{+0.22}_{-0.21}$	$19.42^{+0.92}_{-0.47}$
Fornax	147	237.10, -65.65	$17.84^{+0.11}_{-0.06}$	$17.85^{+0.11}_{-0.08}$
Hercules	132	28.73, 36.87	$16.86^{+0.74}_{-0.68}$	$17.70^{+1.08}_{-0.73}$
Leo I	254	225.99, 49.11	$17.84^{+0.20}_{-0.16}$	$17.93^{+0.65}_{-0.25}$
Leo II	233	220.17, 67.23	$17.97^{+0.20}_{-0.18}$	$18.11^{+0.71}_{-0.25}$
Leo IV	154	265.44, 56.51	$16.32^{+1.06}_{-1.70}$	$16.36^{+1.44}_{-1.65}$
Leo V	178	261.86, 58.54	$16.37^{+0.94}_{-0.87}$	$16.30^{+1.33}_{-1.16}$
Leo T	417	214.85, 43.66	$17.11^{+0.44}_{-0.39}$	$17.67^{+1.01}_{-0.56}$
Sculptor	86	287.53, -83.16	$18.57^{+0.07}_{-0.05}$	$18.63^{+0.14}_{-0.08}$
Segue I	23	220.48, 50.43	$19.36^{+0.32}_{-0.35}$	$17.52^{+2.54}_{-2.65}$
Segue II	35	149.43, -38.14	$16.21^{+1.06}_{-0.98}$	$19.50^{+1.82}_{-1.48}$
Sextans	86	243.50, 42.27	$17.92^{+0.35}_{-0.29}$	$18.04^{+0.50}_{-0.28}$
Ursa Major I	97	159.43, 54.41	$17.87^{+0.56}_{-0.33}$	$18.84^{+0.97}_{-0.43}$
Ursa Major II	32	152.46, 37.44	$19.42^{+0.44}_{-0.42}$	$20.60^{+1.46}_{-0.95}$
Ursa Minor	76	104.97, 44.80	$18.95^{+0.26}_{-0.18}$	$19.08^{+0.21}_{-0.13}$

797 to the source, is provided in Table 5.2.

798 5.4 Likelihood Methods

799 5.4.1 HAWC Likelihoods

800 For every analysis bin in energy, f_{hit} bins (1-9), and location, we can expect N signal events and
801 B background events. The expected number of excess signal events from dark matter annihilation,

Table 5.2 Summary of dSph observations by each experiment used in this work. A ‘-’ indicates the experiment did not observe the dSph for this study. For Fermi-LAT, the exposure at 1 GeV is given. For HAWC, $|\Delta\theta|$ is the absolute difference between the source declination and HAWC latitude. HAWC is more sensitive to sources with smaller $|\Delta\theta|$. For IACTs, we show the zenith angle range, the total exposure, the energy range, the angular radius θ of the signal or ON region, the ratio of exposures between the background-control (OFF) and signal (ON) regions (τ), and the significance of gamma-ray excess in standard deviations, σ .

Source name	Fermi-LAT	HAWC	H.E.S.S, MAGIC, VERITAS						
	Exposure (10^{11} s m 2)	$ \Delta\theta $ (°)	IACT	Zenith (°)	Exposure (h)	Energy range (GeV)	θ (°)	τ	S (σ)
Boötes I	2.6	4.5	VERITAS	15 – 30	14.0	100–41000	0.10	8.6	-1.0
Canes Venatici I	2.9	14.6	–	–	–	–	–	–	–
Canes Venatici II	2.9	15.3	–	–	–	–	–	–	–
Carina	3.1	–	H.E.S.S.	27 – 46	23.7	310 – 70000	0.10	18.0	-0.3
Coma Berenices	2.7	4.9	H.E.S.S.	47 – 49	11.4	550 – 70000	0.10	14.4	-0.4
			MAGIC	5 – 37	49.5	60 – 10000	0.17	1.0	–
			MAGIC	29 – 45	52.1	70 – 10000	0.22	1.0	–
Draco	3.8	38.1	VERITAS	25 – 40	49.8	120 – 70000	0.10	9.0	-1.0
Fornax	2.7	–	H.E.S.S.	11 – 25	6.8	230 – 70000	0.10	45.5	-1.5
Hercules	2.8	6.3	–	–	–	–	–	–	–
Leo I	2.5	6.7	–	–	–	–	–	–	–
Leo II	2.6	3.1	–	–	–	–	–	–	–
Leo IV	2.4	19.5	–	–	–	–	–	–	–
Leo V	2.4	–	–	–	–	–	–	–	–
Leo T	2.6	–	–	–	–	–	–	–	–
Sculptor	2.7	–	H.E.S.S.	10 – 46	11.8	200 – 70000	0.10	19.8	-2.2
Segue I	2.5	2.9	MAGIC	13 – 37	158.0	60 – 10000	0.12	1.0	-0.5
			VERITAS	15 – 35	92.0	80 – 50000	0.10	7.6	0.7
Segue II	2.7	–	–	–	–	–	–	–	–
Sextans	2.4	20.6	–	–	–	–	–	–	–
Ursa Major I	3.4	32.9	–	–	–	–	–	–	–
Ursa Major II	4.0	44.1	MAGIC	35 – 45	94.8	120 – 10000	0.30	1.0	-2.1
Ursa Minor	4.1	–	VERITAS	35 – 45	60.4	160 – 93000	0.10	8.4	-0.1

802 S , is estimated by convolving Equation (5.1) with HAWC's energy response and pixel point spread
 803 functions. I then compute the test statistic (TS) with the log-likelihood ratio test,

$$\text{TS} = -2 \ln \left(\frac{\mathcal{L}_0}{\mathcal{L}^{\max}} \right) \quad (5.6)$$

805 where \mathcal{L}_0 is the null hypothesis, or no DM emission, likelihood. \mathcal{L}^{\max} is the best fit signal
 806 hypothesis where $\langle \sigma v \rangle$ maximizes the likelihood. We calculate the likelihood of each source and
 807 model, assuming events are Poisson distributed, with

$$\mathcal{L} = \prod_i \frac{(B_i + S_i)^{N_i} e^{-(B_i + S_i)}}{N_i!} \quad (5.7)$$

808 where S_i is the sum of expected number of signal counts. B_i is the number of background counts
 809 observed. N_i is the total number of counts.

810 I also calculate an upper limit on $\langle \sigma v \rangle$ by calculating the 95% confidence level (CL). For the
 811 CL, we define a parameter, TS_{95} , as

$$\text{TS}_{95} \equiv \sum_{\text{bins}} \left[2N \ln \left(1 + \frac{\epsilon S_{\text{ref}}}{B} \right) - 2\epsilon S_{\text{ref}} \right] \quad (5.8)$$

812 where the expected signal counts from a dSph is scaled by ϵ . S_{ref} is the expected number of excess
 813 counts in a bin from DM emission from a dSph with a corresponding annihilation cross-section,
 814 $\langle \sigma v \rangle$. We scan ϵ such that

$$2.71 = \text{TS}_{\max} - \text{TS}_{95} \quad (5.9)$$

815 5.4.2 Glory Duck Joint Likelihood

816 The joint likelihood for the 5-experiment combination was done similarly as Section 5.4.1. We
 817 calculate upper limits on $\langle \sigma v \rangle$ from the TS, Eq. (5.6), and define the likelihood ratio more generally

$$\lambda(\langle \sigma v \rangle | \mathcal{D}_{\text{dSphs}}) = \frac{\mathcal{L}(\langle \sigma v \rangle; \hat{\nu} | \mathcal{D}_{\text{dSphs}})}{\mathcal{L}(\widehat{\langle \sigma v \rangle}; \hat{\nu} | \mathcal{D}_{\text{dSphs}})} \quad (5.10)$$

818 $\mathcal{D}_{\text{dSphs}}$ is the totality of observations across experiments and dSphs. ν are the nuisance parameters
 819 which are the J factors in this study. $\widehat{\langle \sigma v \rangle}$ and $\hat{\nu}$ are the respective estimate that maximize \mathcal{L}
 820 globally. Finally, $\hat{\nu}$ is the set of nuisance parameters that maximize \mathcal{L} for a fixed value of $\langle \sigma v \rangle$.

821 The *complete* joint likelihood, \mathcal{L} that encompasses all observations from all instruments and
 822 dSphs can be factorized into *partial* functions for each dSph l (with $\mathcal{L}_{\text{dSph},l}$) and its J factor (\mathcal{J}_l):

$$\mathcal{L} (\langle \sigma v \rangle; \nu | \mathcal{D}_{\text{dSphs}}) = \prod_{l=1}^{N_{\text{dSphs}}} \mathcal{L}_{\text{dSph},l} (\langle \sigma v \rangle; J_l, \nu_l | \mathcal{D}_l) \times \mathcal{J}_l (J_l | J_{l,\text{obs}}, \sigma_{\log J_l}). \quad (5.11)$$

823 For this study, $N_{\text{dSphs}} = 20$ is the number of dSphs studied. \mathcal{D}_l are the gamma-ray observations
 824 of dSph, l . ν_l are the nuisance parameters modifying the gamma-ray observations of dSph, l ,
 825 but excludes \mathcal{J}_l . \mathcal{J}_l is the J factor for dSph, l , as defined in Equation (5.2), and it is a nuisance
 826 parameter whose value is unknown. $\log_{10} J_{l,\text{obs}}$ and $\sigma_{\log J_l}$ are obtained from fitting a log-normal
 827 function of $J_{l,\text{obs}}$ to the posterior distribution of J_l [48]. $\log_{10} J_{l,\text{obs}}$ and $\sigma_{\log J_l}$ values are provided
 828 in Table 5.1. The term \mathcal{J}_l constraining J_l is written as:

$$\mathcal{J}_l (J_l | J_{l,\text{obs}}, \sigma_{\log J_l}) = \frac{1}{\ln(10) J_{l,\text{obs}} \sqrt{2\pi} \sigma_{\log J_l}} \exp\left(-\frac{(\log_{10} J_l - \log_{10} J_{l,\text{obs}})^2}{2\sigma_{\log J_l}^2}\right). \quad (5.12)$$

829 Both the \mathcal{GS} and \mathcal{B} , displayed in Table 5.1, sets of J factors are used in this analysis. Equation (5.12)
 830 is also normalized, so it can also be interpreted as a probability density function (PDF) for $J_{l,\text{obs}}$.
 831 From Equation (5.1), we can also see that $\langle \sigma v \rangle$ and J_l are degenerate when computing $\mathcal{L}_{\text{dSph},l}$.
 832 Therefore, as noted in [49], it is sufficient to compute $\mathcal{L}_{\text{dSph},l}$ versus $\langle \sigma v \rangle$ for a fixed value of J_l .
 833 We used $J_{l,\text{obs}}(\mathcal{GS})$ reported in Tab. 5.1, in order to perform the profile of \mathcal{L} with respect to J_l .
 834 The degeneracy implies that for any $J'_l \neq J_{l,\text{obs}}$ (in practice in our case we used $J'_l = J_{l,\text{obs}}(\mathcal{B})$ to
 835 compute results from a different set of J factors):

$$\mathcal{L}_{\text{dSph},l} (\langle \sigma v \rangle; J'_l, \nu_l | \mathcal{D}_l) = \mathcal{L}_{\text{dSph},l} \left(\frac{J'_l}{J_{l,\text{obs}}} \langle \sigma v \rangle; J_{l,\text{obs}}, \nu_l | \mathcal{D}_l \right), \quad (5.13)$$

836 which is a straightforward rescaling operation that reduces the computational needs of the profiling
 837 operation since:

$$\mathcal{L} (\langle \sigma v \rangle; \hat{\nu} | \mathcal{D}_{\text{dSphs}}) = \prod_{l=1}^{N_{\text{dSphs}}} \max_{J_l} \left[\mathcal{L}_{\text{dSph},l} (\langle \sigma v \rangle; J_l, \hat{\nu}_l | \mathcal{D}_l) \times \mathcal{J}_l (J_l | J_{l,\text{obs}}, \sigma_{\log J_l}) \right]. \quad (5.14)$$

838 In addition, Eq. (5.13) enables the combination of data from different gamma-ray instruments and
 839 observed dSphs via tabulated values of $\mathcal{L}_{\text{dSph},l}$, or equivalently of λ from Eq. (5.10) as was done in

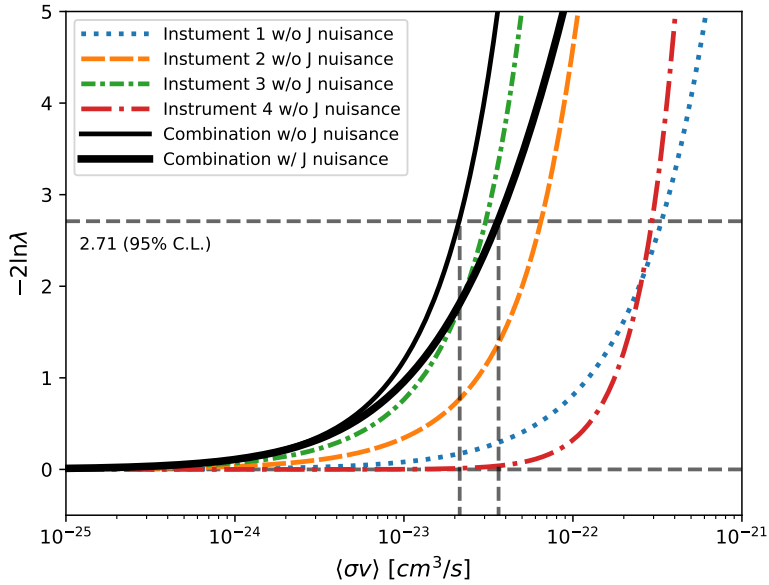


Figure 5.4 Illustration of the combination technique showing a comparison between $-2 \ln \lambda$ provided by four instruments (colored lines) from the observation of the same dSph without any J nuisance and their sum, *i.e.* the resulting combined likelihood (thin black line). According to the test statistics of Equation (5.6), the intersection of the likelihood profiles with the line $-2 \ln \lambda = 2.71$ indicates the 95% C.L. upper limit on $\langle \sigma v \rangle$. The combined likelihood (thin black line) shows a smaller value of upper limit on $\langle \sigma v \rangle$ than those derived by individual instruments. We also show how the uncertainties on the J factor effects the combined likelihood and degrade the upper limit on $\langle \sigma v \rangle$ (thick black line). All likelihood profiles are normalized so that the global minimum $\widehat{\langle \sigma v \rangle}$ is 0. We note that each profile depends on the observational conditions in which a target object was observed. The sensitivity of a given instrument can be degraded and the upper limits less constraining if the observations are performed in non-optimal conditions such as a high zenith angle or a short exposure time.

840 this work, versus $\langle \sigma v \rangle$. $\mathcal{L}_{\text{dSph},l}$ is computed for a fixed value of J_l and profiled with respect to all
 841 instrumental nuisance parameters ν_l , these nuisance parameters are discussed in more detail below.
 842 These values are produced by each detector independently and therefore there is no need to share
 843 sensitive low-level information used to produce them, such as event lists. Figure 5.4 illustrates the
 844 multi-instrument combination technique used in this study with a comparison of the upper limit
 845 on $\langle \sigma v \rangle$ obtained from the combination of the observations of four experiments towards one dSph
 846 versus the upper limit from individual instruments. It also shows graphically the effect of the
 847 J -factor uncertainty on the combined observations.

848 The *partial* joint likelihood function for gamma-ray observations of each dSph ($\mathcal{L}_{\text{dSph},l}$) is

written as the product of the likelihood terms describing the $N_{\text{exp},l}$ observations performed with any of our observatories:

$$\mathcal{L}_{\text{dSph},l} (\langle \sigma v \rangle; J_l, \nu_l | \mathcal{D}_l) = \prod_{k=1}^{N_{\text{exp},l}} \mathcal{L}_{lk} (\langle \sigma v \rangle; J_l, \nu_{lk} | \mathcal{D}_{lk}), \quad (5.15)$$

where each \mathcal{L}_{lk} term refers to an observation of the l -th dSph with associated k -th instrument responses. $N_{\text{exp},l}$ varies from dSph to dSph and can be inferred from Table 5.2.

Each collaboration separately analyzes their data for \mathcal{D}_{lk} corresponding to dSph l and gamma-ray detector k , using as many common assumptions as possible in the analysis. HAWC's treatment was described earlier in Section 5.4.1 whereas the specifics of the remaining experiments is left to the publication. We compute the values for the likelihood functions \mathcal{L}_{lk} (see Eq. (5.15)) for a fixed value of J_l and profile over the rest of the nuisance parameters ν_{lk} . Then, values of λ from Eq. (5.10) are computed as a function of $\langle \sigma v \rangle$, and shared using a common format. Results are computed for seven annihilation channels, W^+W^- , ZZ , $b\bar{b}$, $t\bar{t}$, e^+e^- , $\mu^+\mu^-$, and $\tau^+\tau^-$ over 62 m_χ values between 5 GeV and 100 TeV provided in [44]. The $\langle \sigma v \rangle$ range is defined between 10^{-28} and $10^{-18} \text{ cm}^3 \cdot \text{s}^{-1}$, with 1001 logarithmically spaced values. The likelihood combination, i.e. Equation (5.11), and profile over the J -factor to compute the profile likelihood ratio λ , Equation (5.10), are carried out with two different public analysis software packages, namely `gLike` [50] and `LklCom` [51], that provide the same results [52].

As mentioned previously, each experiment computes the \mathcal{L}_{lk} from Equation (5.10) differently. The remainder of this section highlights the differences in this calculation across the experiments. Four experiments, namely *Fermi*-LAT, H.E.S.S., HAWC and MAGIC, use a binned likelihood to compute the \mathcal{L}_{lk} . For these experiments, for each observation \mathcal{D}_{lk} of a given dSph l carried out using a given gamma-ray detector k , the binned likelihood function is:

$$\mathcal{L}_{lk} (\langle \sigma v \rangle; J_l, \nu_{lk} | \mathcal{D}_{lk}) = \prod_{i=1}^{N_E} \prod_{j=1}^{N_P} \left[\mathcal{P}(s_{lk,ij}(\langle \sigma v \rangle, J_l, \nu_{lk}) + b_{lk,ij}(\nu_{lk}) | N_{lk,ij}) \right] \times \mathcal{L}_{lk,\nu} (\nu_{lk} | \mathcal{D}_{\nu_{lk}}) \quad (5.16)$$

where N_E and N_P are the number of considered bins in reconstructed energy and arrival direction, respectively; \mathcal{P} represents a Poisson PDF for the number of gamma-ray candidate events $N_{lk,ij}$

872 observed in the i -th bin in energy and j -th bin in arrival direction, when the expected number is
 873 the sum of the expected mean number of signal events s_{ij} (produced by DM annihilation) and of
 874 background events b_{ij} ; $\mathcal{L}_{lk,\nu}$ is the likelihood term for the extra ν_{lk} nuisance parameters that vary
 875 from one instrument k to another. The expected counts for signal events s_{ij} for a given dSph l and
 876 detector k is given by:

$$s_{ij}(\langle\sigma\nu\rangle, J) = \int_{E'_{\min,i}}^{E'_{\max,i}} dE' \int_{P'_{\min,j}}^{P'_{\max,j}} d\Omega' \int_0^\infty dE \int_{\Delta\Omega_{tot}} d\Omega \int_0^{T_{\text{obs}}} dt \frac{d^2\Phi(\langle\sigma\nu\rangle, J)}{dEd\Omega} \text{IRF}(E', P' | E, P, t) \quad (5.17)$$

877 where E' and E are the reconstructed and true energies, P' and P the reconstructed and true
 878 arrival directions; $E'_{\min,i}$, $P'_{\min,j}$, $E'_{\max,i}$, and $P'_{\max,j}$ are their lower and upper limits of the i -th
 879 energy bin and the j -th arrival direction bin; T_{obs} is the (dead-time corrected) total observation
 880 time; t is the time along the observations; $d^2\Phi/dEd\Omega$ is the DM flux in the source region (see
 881 Equation (5.1)); and $\text{IRF}(E', P' | E, P, t)$ is the IRF, which can be factorized as the product of the
 882 effective collection area of the detector $A_{\text{eff}}(E, P, t)$, the PDFs for the energy estimator $f_E(E' | E, t)$,
 883 and arrival direction $f_P(P' | E, P, t)$ estimators. Note that for Fermi-LAT, HAWC, MAGIC, and
 884 VERITAS the effect of the finite angular resolution is taken into account through the convolution
 885 of $d\Phi/dEd\Omega$ with f_P in Equation (5.17), whereas in the cases of H.E.S.S. f_P is approximated by a
 886 delta function. This approximation has been made in order to maintain compatibility of the result
 887 with what has been previously published. The difference introduced by this approximation is $< 5\%$
 888 for all considered dSphs. A more comprehensive review of the differences between the analyses of
 889 different instruments can be found in [25].

890 5.5 HAWC Results

891 13 of the 20 dSphs considered for the Glory Duck analysis are within HAWC's field of view.
 892 These dSph are analyzed for emission from DM annihilation according to the likelihood method
 893 described in Section 5.4. The 13 likelihood profiles are then stacked to synthesize a combined
 894 limit on the dark matter cross-section, $\langle\sigma\nu\rangle$. This combination is done for the 7 SM annihilation
 895 channels used in the Glory Duck analysis. Figure 5.5 shows the combined limit for all annihilation
 896 channels with HAWC only observations. We also perform 300 studies of Poisson trials on the

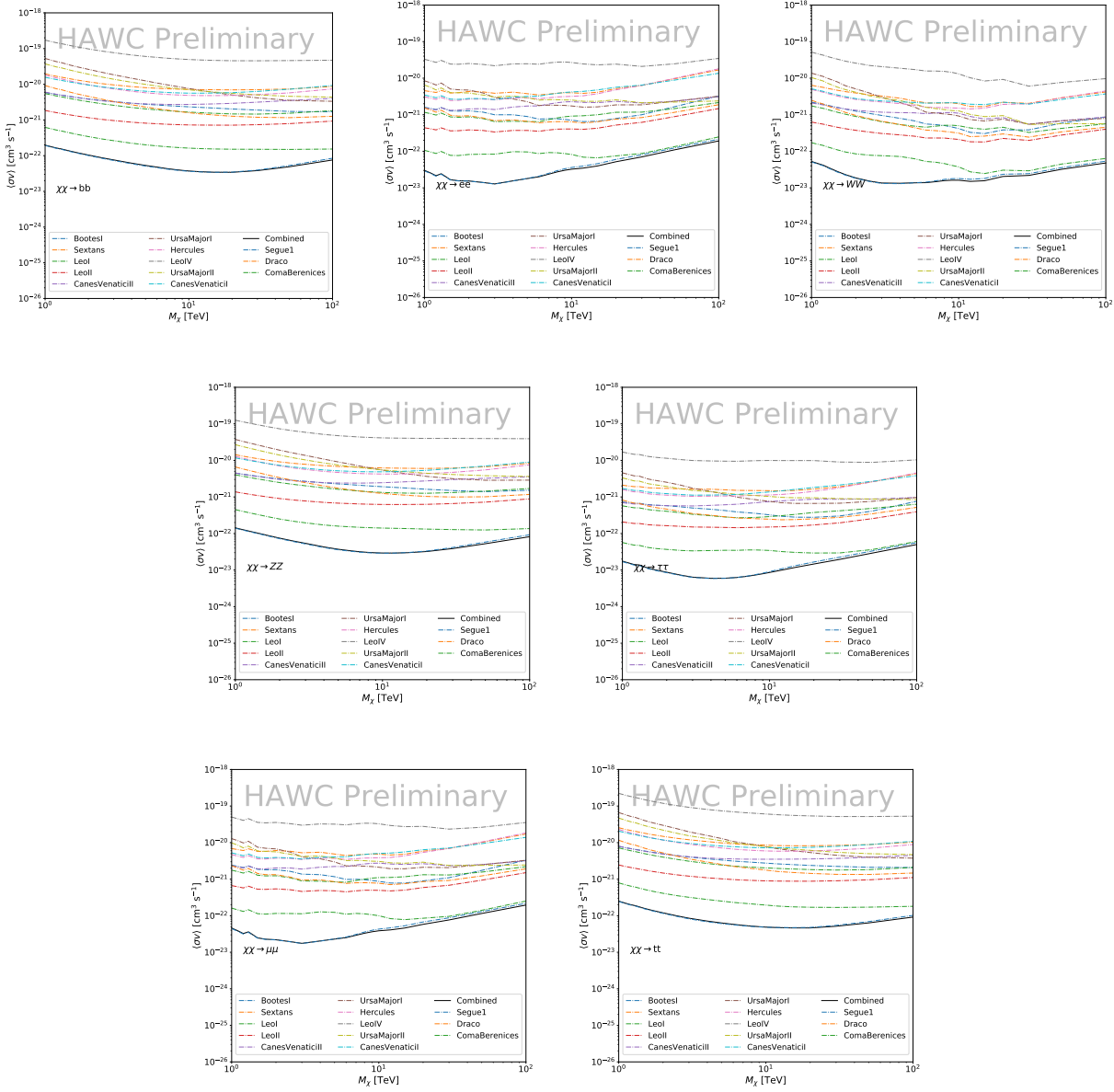


Figure 5.5

background. These trials are used to produce HAWC Brazil bands which were shared with the other collaborators for combined Brazil Bands. The results on fitting to HAWC's Poisson trials of the DM hypothesis is shown in Figure 5.7 for all the DM annihilation channels studied for Glory Duck.

No DM was found in HAWC observations. HAWC's limits are dominated by the dSphs Segue1 and Coma Berenices. The remaining 11 dSphs do not contribute significantly to the limit because

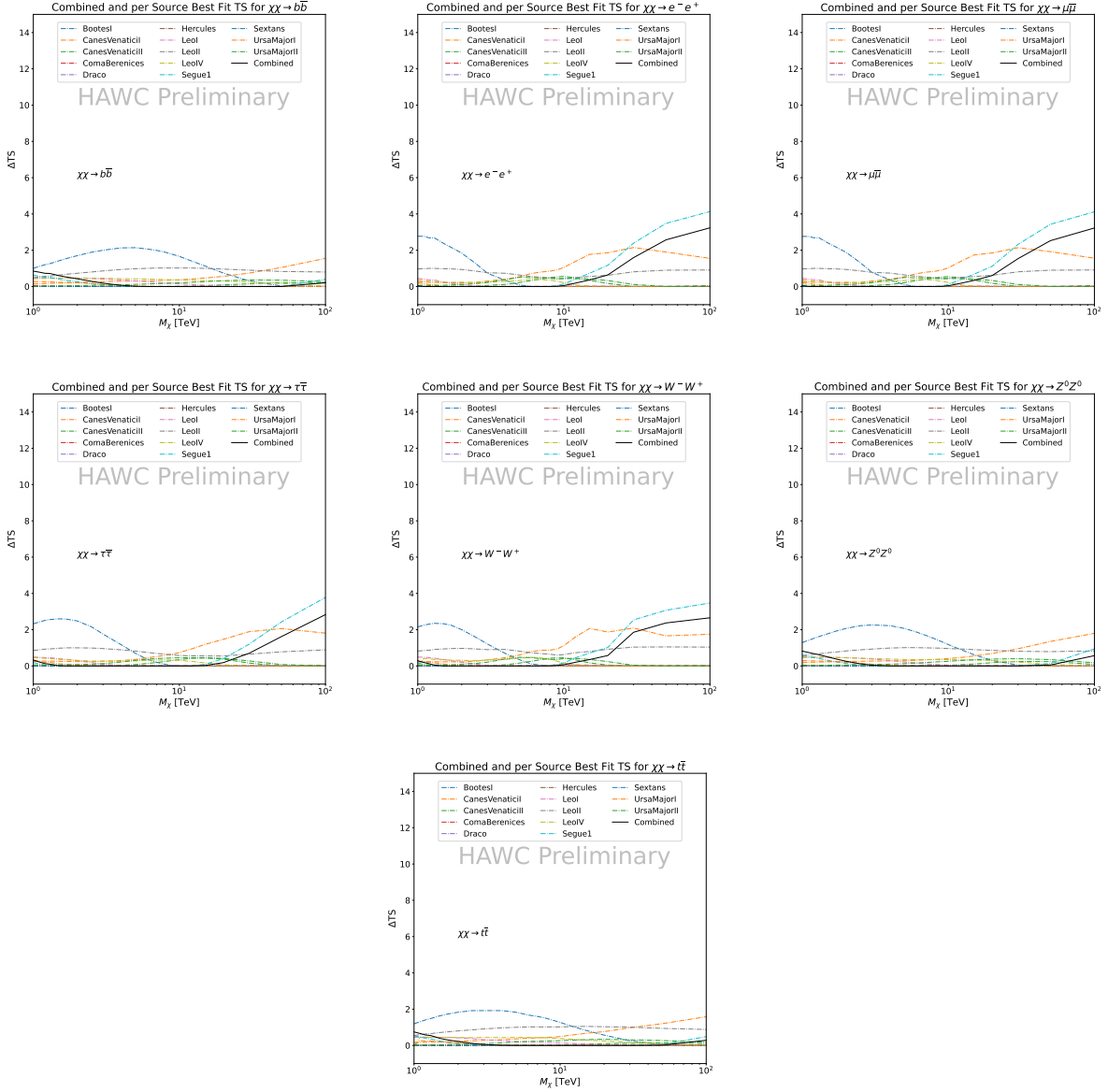


Figure 5.6 HAWC TS values for best fit $\langle \sigma v \rangle$ versus m_χ for seven SM annihilation channels with J factors from \mathcal{GS} . The solid black line shows the combined best fit TS values. The colored, dashed lines are the TS values for each of the 13 sources HAWC studied.

903 they are at high zenith and/or have much smaller J factors. Even though some remaining dSphs
 904 have large J factors, they are towards the edge of HAWC's field of view where HAWC analysis is
 905 less sensitive.

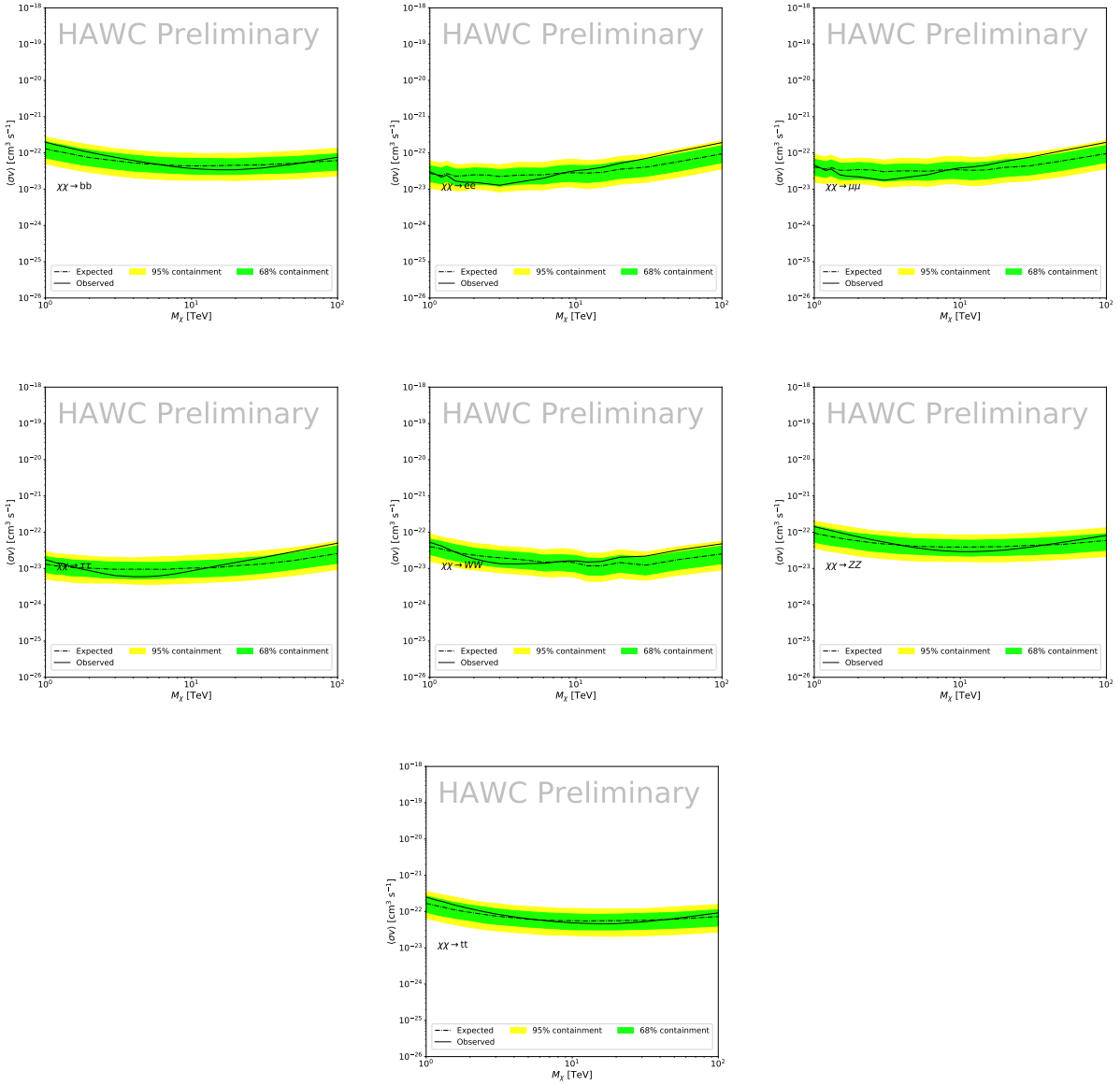


Figure 5.7 HAWC Brazil bands at 95% confidence level on $\langle\sigma v\rangle$ versus DM mass for seven annihilation channels with J -factors from \mathcal{GS} [53]. The solid line represents the combined limit from 13 dSphs. The dashed line is the expected limit. The green band is the 68% containment. The yellow band is the 95% containment.

906 5.6 Glory Duck Combined Results

907 The crux of this analysis is that HAWC's results are combined with 4 other gamma-ray observa-
 908 tories: Fermi-LAT, H.E.S.S., MAGIC, and VERITAS. No significant DM emission was observed
 909 by any of the five instruments. We present the upper limits on $\langle\sigma v\rangle$ assuming seven independent
 910 DM self annihilation channels, namely W^+W^- , Z^+Z^- , $b\bar{b}$, $t\bar{t}$, e^+e^- , $\mu^+\mu^-$, and $\tau^+\tau^-$. The 68%

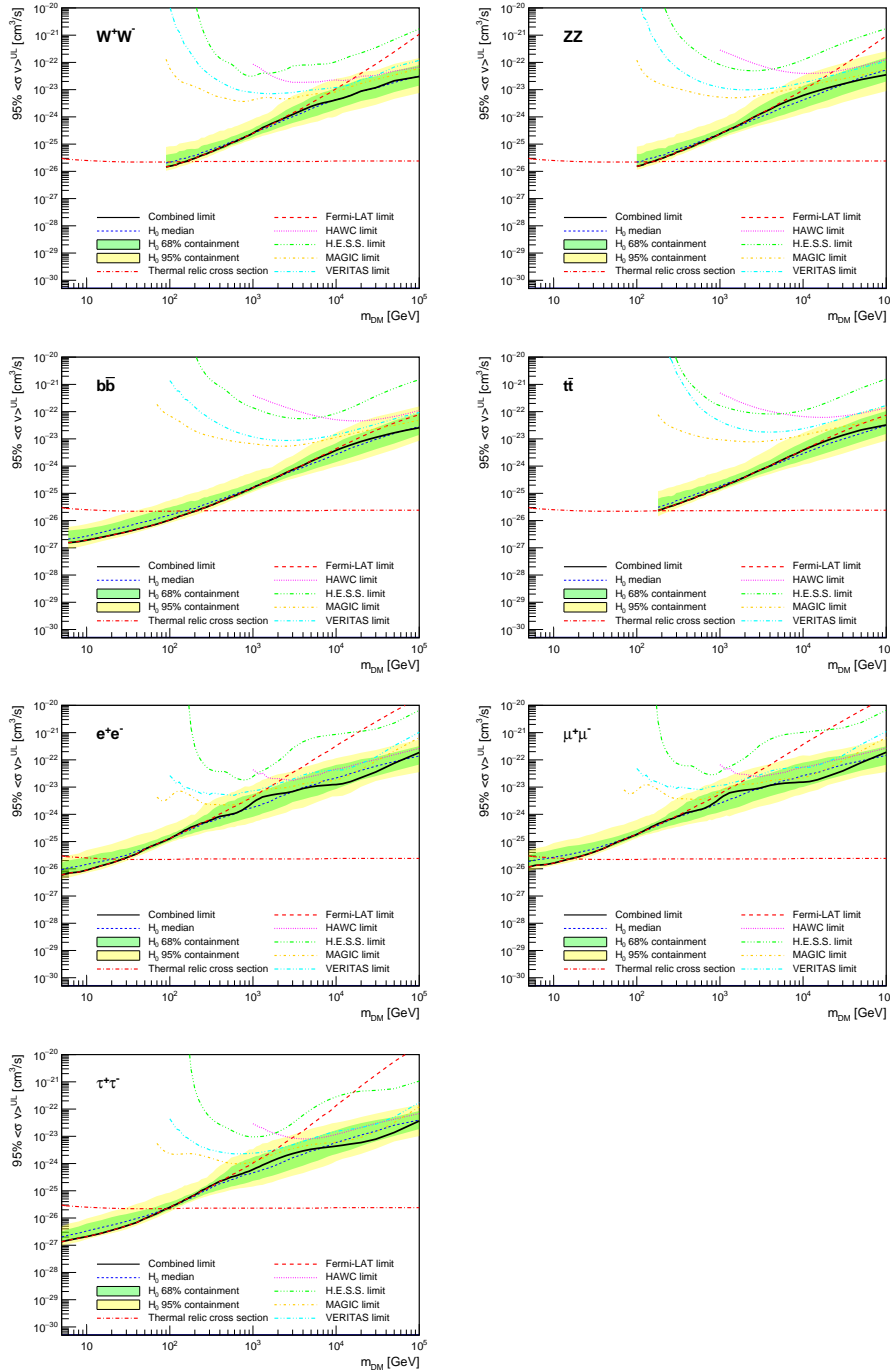


Figure 5.8 Upper limits at 95% confidence level on $\langle\sigma v\rangle$ in function of the DM mass for eight annihilation channels, using the set of J factors from Ref. [53] (\mathcal{GS} set in Table 5.1). The black solid line represents the observed combined limit, the black dashed line is the median of the null hypothesis corresponding to the expected limit, while the green and yellow bands show the 68% and 95% containment bands. Combined upper limits for each individual detector are also indicated as solid, colored lines. The value of the thermal relic cross-section in function of the DM mass is given as the red dotted-dashed line [54].

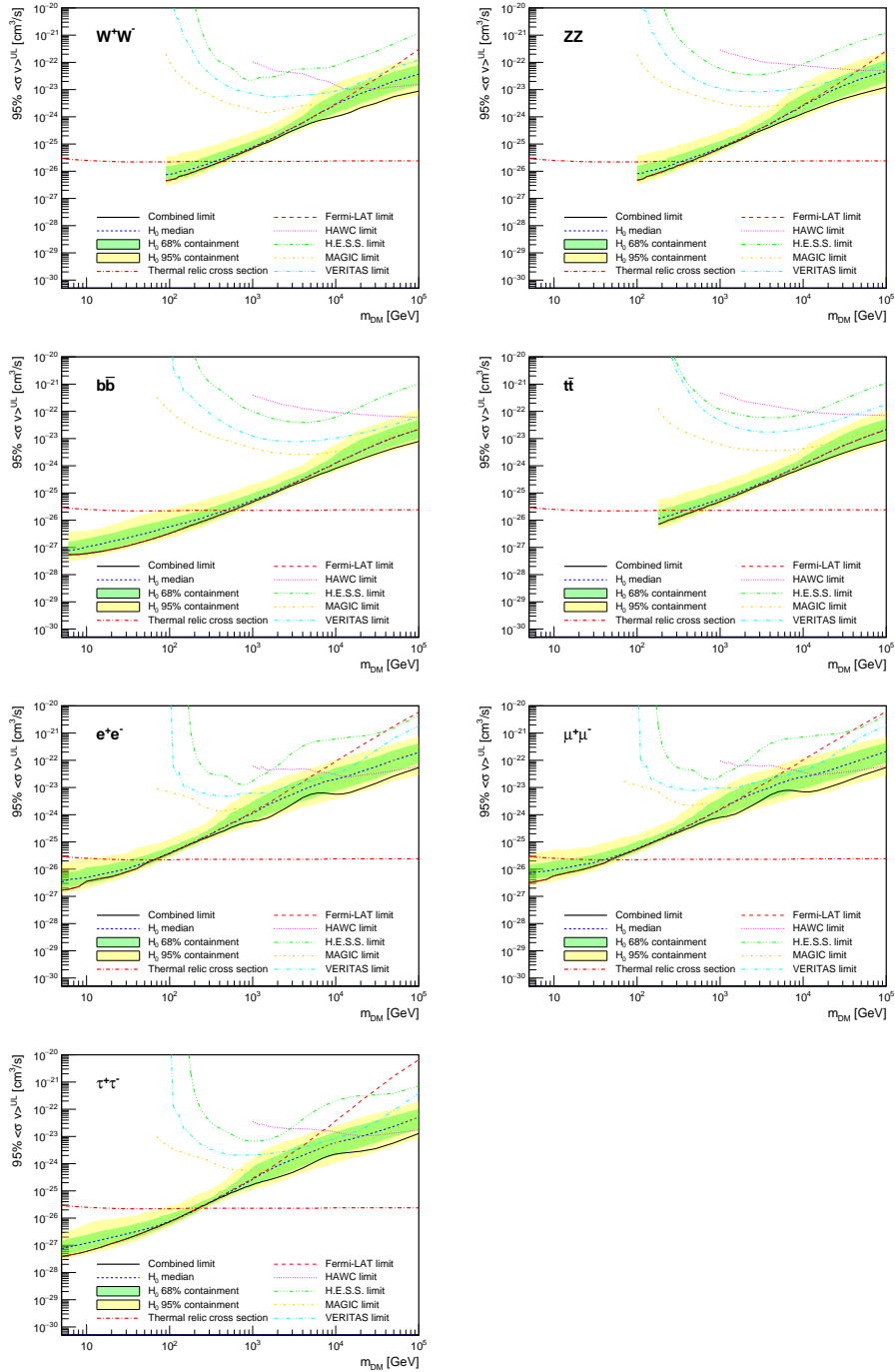


Figure 5.9 Same as Fig. 5.8, using the set of J factors from Ref. [47, 55] (\mathcal{B} set in Table 5.1).

and 95% containment bands are produced from 300 Poisson realizations of the null hypothesis corresponding to each of the combined datasets. These 300 realizations are combined identically to dSph observations. The containment bands and the median are extracted from the distribution of resulting limits on the null hypothesis. These 300 realizations are obtained either by fast simu-

915 lations of the OFF observations, for H.E.S.S., MAGIC, VERITAS, and HAWC, or taken from real
916 observations of empty fields of view in the case of Fermi-LAT [48, 56, 57].

917 The obtained limits are shown in Figure 5.8 for the $\mathcal{G}\mathcal{S}$ set of J -factors [53] and in Figure 5.9
918 for the \mathcal{B} set of J -factors [47, 55]. The combined limits are presented with their 68% and 95%
919 containment bands, and are expected to be close to the median limit when no signal is present.
920 We observe agreement with the null hypothesis for all channels, within 2σ standard deviations,
921 between the observed limits and the expectations given by the median limits. Limits obtained from
922 each detector are also indicated in the figures, where limits for all dSphs observed by the specific
923 instrument have been combined.

924 Below ~ 300 GeV, the *Fermi*-LAT dominates the DM limits for all annihilation channels. From
925 ~ 300 GeV to ~ 2 TeV, *Fermi*-LAT continues to dominate for the hadronic and bosonic DM channels,
926 yet the IACTs (H.E.S.S., MAGIC, and VERITAS) and *Fermi*-LAT all contribute to the limit for
927 leptonic DM channels. For DM masses between ~ 2 TeV to ~ 10 TeV, the IACTs dominate leptonic
928 DM annihilation channels, whereas both the *Fermi*-LAT and the IACTs dominate bosonic and
929 hadronic DM annihilation channels. From ~ 10 TeV to ~ 100 TeV, both the IACTs and HAWC
930 contribute significantly to the leptonic DM limit. For hadronic and bosonic DM, the IACTs and
931 *Fermi*-LAT both contribute strongly.

932 We notice that the limits computed using the \mathcal{B} set of J -factor are always better compared to the
933 ones calculated with the $\mathcal{G}\mathcal{S}$ set. For the W^+W^- , Z^+Z^- , $b\bar{b}$, and $t\bar{t}$ channels, the ratio between the
934 limits computed with the two sets of J -factor is varying between a factor of ~ 3 and ~ 5 depending
935 on the energy, with the largest ratio around 10 TeV. For the channels e^+e^- , $\mu^+\mu^-$, and $\tau^+\tau^-$, the
936 ratio lies between ~ 2 to ~ 6 , being maximum around 1 TeV. Examining Figure 5.16 and Figure 5.17
937 in Section 5.8, these differences are explained by the fact that the \mathcal{B} set provides higher J -factors
938 for the majority of the studied dSphs, with the notable exception of Segue I. The variation on the
939 ratio of the limits for the two sets is due to different dSph dominating the limits depending on the
940 energy. This pushes the range of thermal cross-section which can be excluded to higher mass. This
941 comparison demonstrates the magnitude of systematic uncertainties associated with the choice of

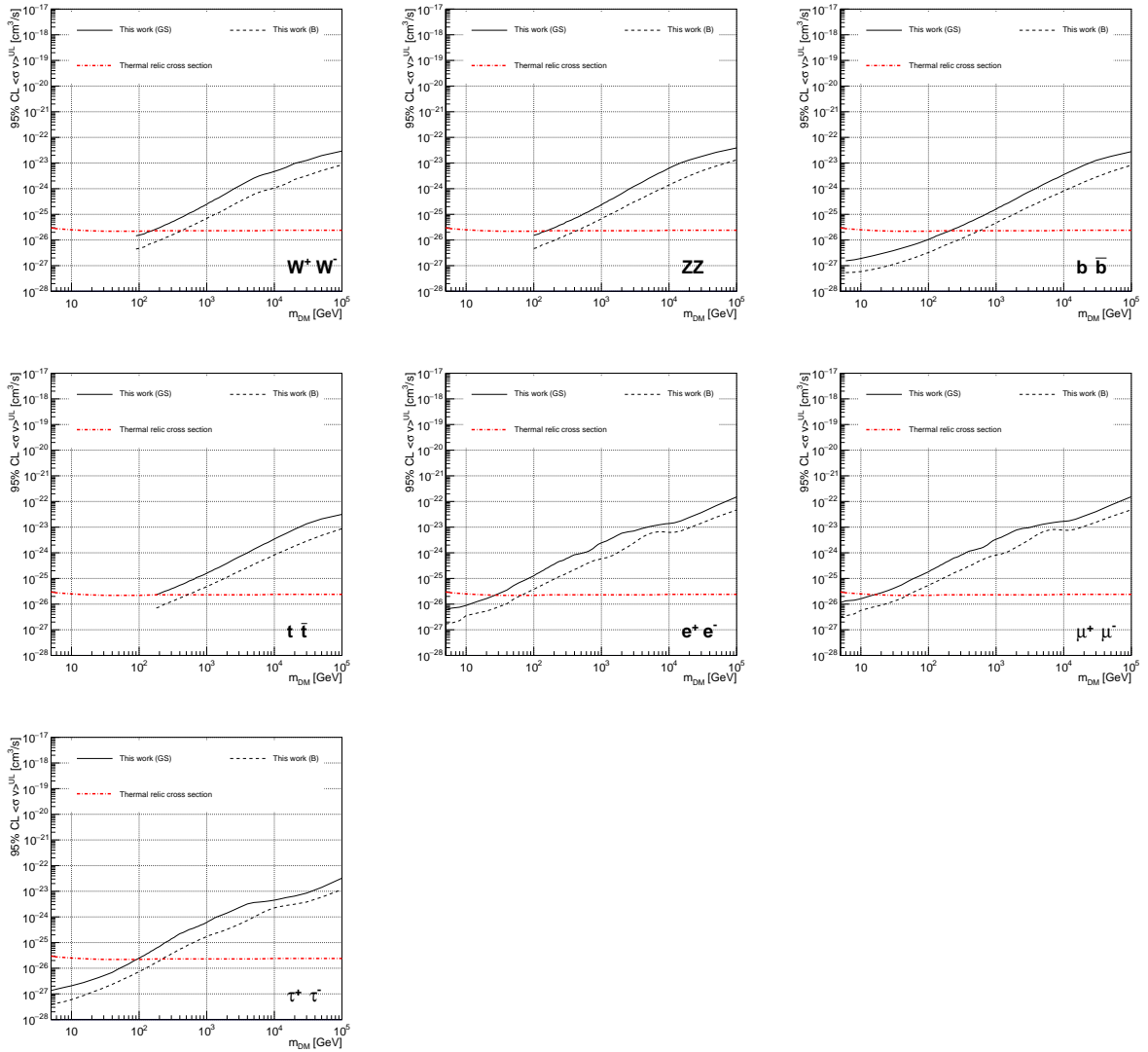


Figure 5.10 Comparisons of the combined limits at 95% confidence level for each of the eight annihilation channels when using the J factors from Ref. [53] (\mathcal{GS} set in Table 5.1), plain lines, and the J factor from Ref. [47, 55] (\mathcal{B} set in Table 5.1), dashed lines. The cross-section given by the thermal relic is also indicated [54].

942 the J -factor

943 This comparison demonstrates the magnitude of systematic uncertainties associated with the
 944 choice of the J -factor calculation. The \mathcal{GS} and \mathcal{B} sets present a difference in the limits for all
 945 channels of about This difference is explained, see Figure 5.16 and Figure 5.17 in Appendix, by the
 946 fact that the \mathcal{B} set provides higher J factors for all dSph except for Segue I. This pushes the range
 947 of thermal cross-section which can be excluded to higher mass.

948 **5.7 HAWC Systematics**

949 **5.7.1 Inverse Compton Scattering**

950 The DM-DM annihilation channels produce many high energy electrons regardless of the
951 primary annihilation channel. These high energy electrons can produce high energy gamma-rays
952 through Inverse Compton Scattering (ICS). If this effect is strong, it would change the morphology
953 of the source and increase the total expected gamma-ray counts from any source. The PPPC [44]
954 provides tools in Mathematica for calculating the impact of ICS for an arbitrary location in the
955 sky for a specified annihilation channel. We calculated the change in gamma-ray counts for DM
956 annihilation to primary $e\bar{e}$ for RA and Dec corresponding to Segue1 and Coma Berenices. These
957 dSphs were chosen because they are the strongest contributors to the limit. $e\bar{e}$ was selected because
958 it would have the largest number of high energy electrons. The effect was found to be on the order
959 of 10^{-7} on the gamma-ray spectrum. As a result, this systematic is not considered in our analysis.

960 **5.7.2 Point Source Versus Extended Source Limits**

961 The previous DM search toward dSph approximated the dSphs as point sources [46]. In
962 this analysis, the dSphs are implemented as extended with J-factor distributions following those
963 produced by [53]. The resolution of the cited map is much finer than HAWC's angular resolution.
964 The vast majority of the J-factor distribution is represented on the central HAWC pixel of the dSph
965 spatial map. However, the neighboring 8 pixels are not negligible and contribute to our limit.

966 Figure 5.11 shows a substantial improvement to the limit for Segue1. Fig. 5.12 however showed
967 identical limits. These disparities are best explained by the relative difference in their J-Factors.
968 Both dSphs pass almost overhead the HAWC detector, however Segue1 has the larger J-Factor
969 between the two. Adjacent pixels to the central pixel will therefore contribute to the limits. This is
970 the case for other dSph that are closer to overhead the HAWC detector.

971 Comparison plots for all sources and the combined limit can be found in the sandbox for the
972 Glory Duck project.

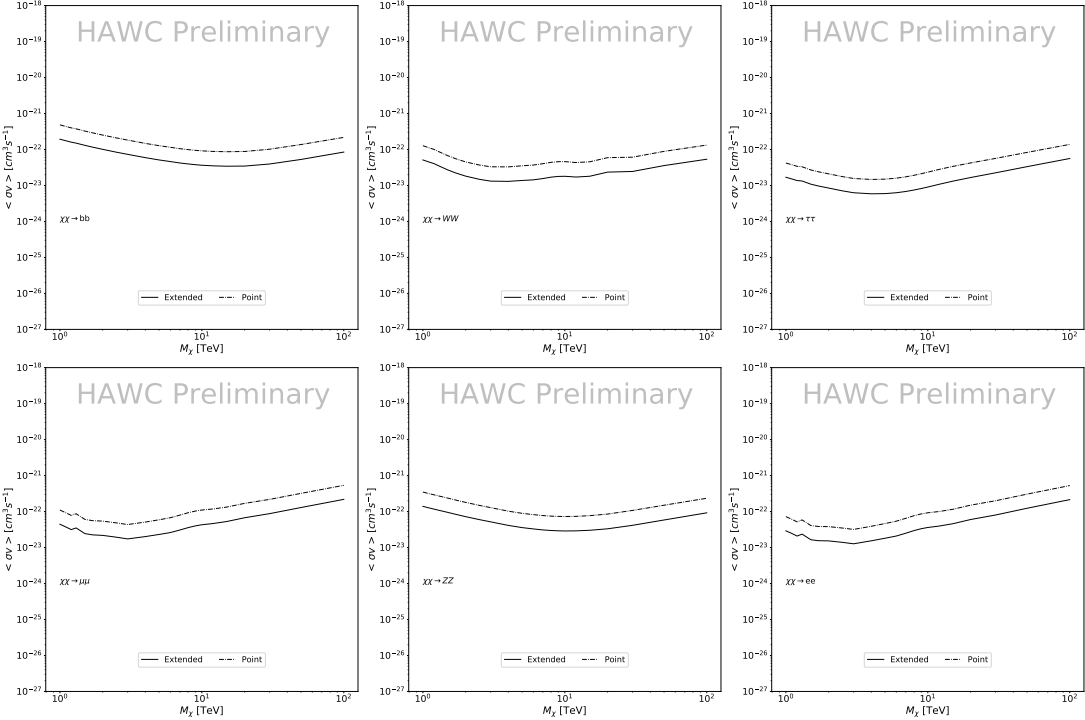


Figure 5.11 Comparisons of the combined limits at 95% confidence level for a point source analysis and extended source using [53] \mathcal{GS} J-factor distributions and PPPC [44] annihilation spectra. Shown are the limits for Segue1 which will have the most significant impact on the combined limit. 6 of the 7 DM annihilation channels are shown. Solid lines are extended source studies. Dashed lines are point source studies. Overall, the extended source analysis improves the limit by a factor of 2.

973 5.7.3 Impact of Pointing Systematic

974 During the analysis it was discovered that reconstruction of gamma-rays. Slides describing this
 975 systematic can be found [here](#). Shown on the presentation is dependence on the pointing systematic
 976 on declination. New spatial profiles were generated for every dSph and limits were computed for
 977 the adjusted declination.

978 Section 5.7.3 demonstrates the impact of this systematic for all DM annihilation channels
 979 studied by HAWC. The impact is a tiny improvement, yet mostly identical, to the combined limits.

980 5.8 J-factor distributions

981 5.8.1 Numerical integration of \mathcal{GS} maps

982 It was discovered well after the HAWC analysis was completed that the published tables from
 983 \mathcal{GS} [45] quoted median J-factors were computed in a non-trivial manner. The assumption myself

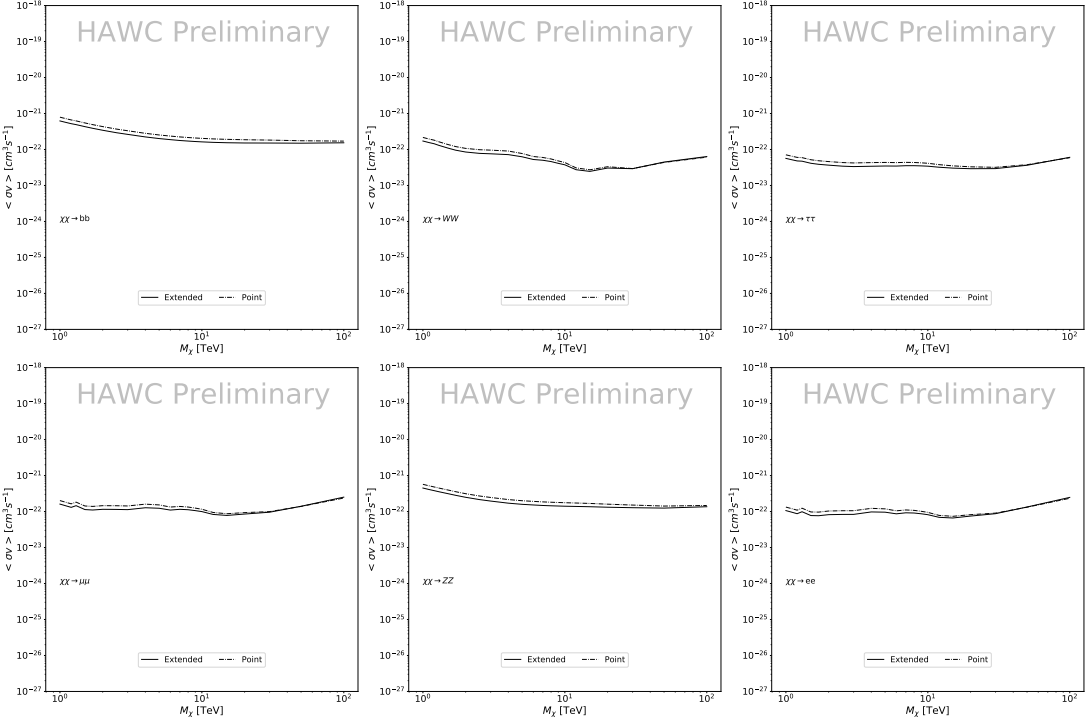


Figure 5.12 Same as Fig. 5.11 on Coma Berenices. This dSph also contributes significantly to the limit. The limits are identical in this case.

and collaborators had been that the published tables represented the J -factor as a function of θ for the best global fit model on a per-source basis. However, this is not the case. Instead, what is published are the best fit model for each dwarf that only considers stars up to the angular separation θ . Therefore, the model is changing for each value of θ for each dwarf. Yet, the introduced features from unique models at each θ are much smaller than the angular resolution of HAWC. It is not expected for these effects to impact the limits and TS greatly as a result.

Median J -factor model profiles were provided by the authors. New maps were generated and analyzed for Segue1 and Coma Berenices. Figure 5.14 shows the differential between maps generated with the method from Section 5.8.1 and from the authors of [45]. These maps were reanalyzed for all SM DM annihilation channels. Upper limits for these channels are shown in Figure 5.15

From Figure 5.15, we can see that the impact of these model difference was no substantial. The observed impact was a fractional effect which is much smaller than the impact from selecting another DM spatial distribution model as was shown in Figure 5.10.

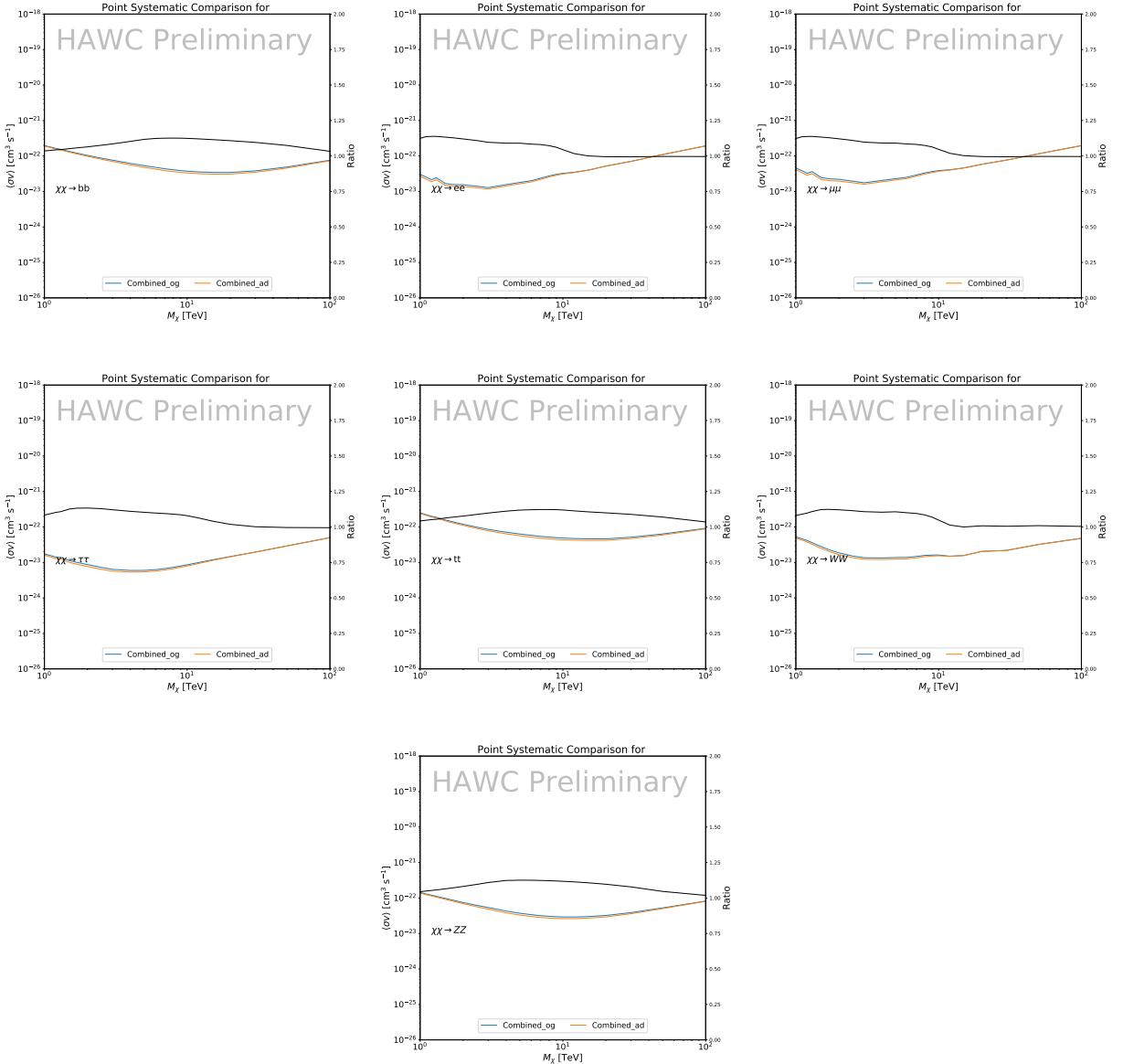


Figure 5.13 Comparison of combined limits when correcting for HAWC’s pointing systematic. All DM annihilation channels are shown. The solid black line is the ratio between published limit to the declination corrected limit. The blue solid line or “Combined_{og}” represented the limits computed for Glory Duck. The solid orange line or “Combined_{ad}” represented the limits computed after correcting for the pointing systematic.

998 5.8.2 $\mathcal{G}\mathcal{S}$ Versus \mathcal{B} spatial models

999 We show in this appendix a comparison between the J -factors computed by Geringer-Sameth
1000 *et al.* [53] (the $\mathcal{G}\mathcal{S}$ set) and the ones computed by Bonnivard *et al.* [47, 55] (the \mathcal{B} set). The
1001 $\mathcal{G}\mathcal{S}$ J -factors are computed through a Jeans analysis of the kinematic stellar data of the selected

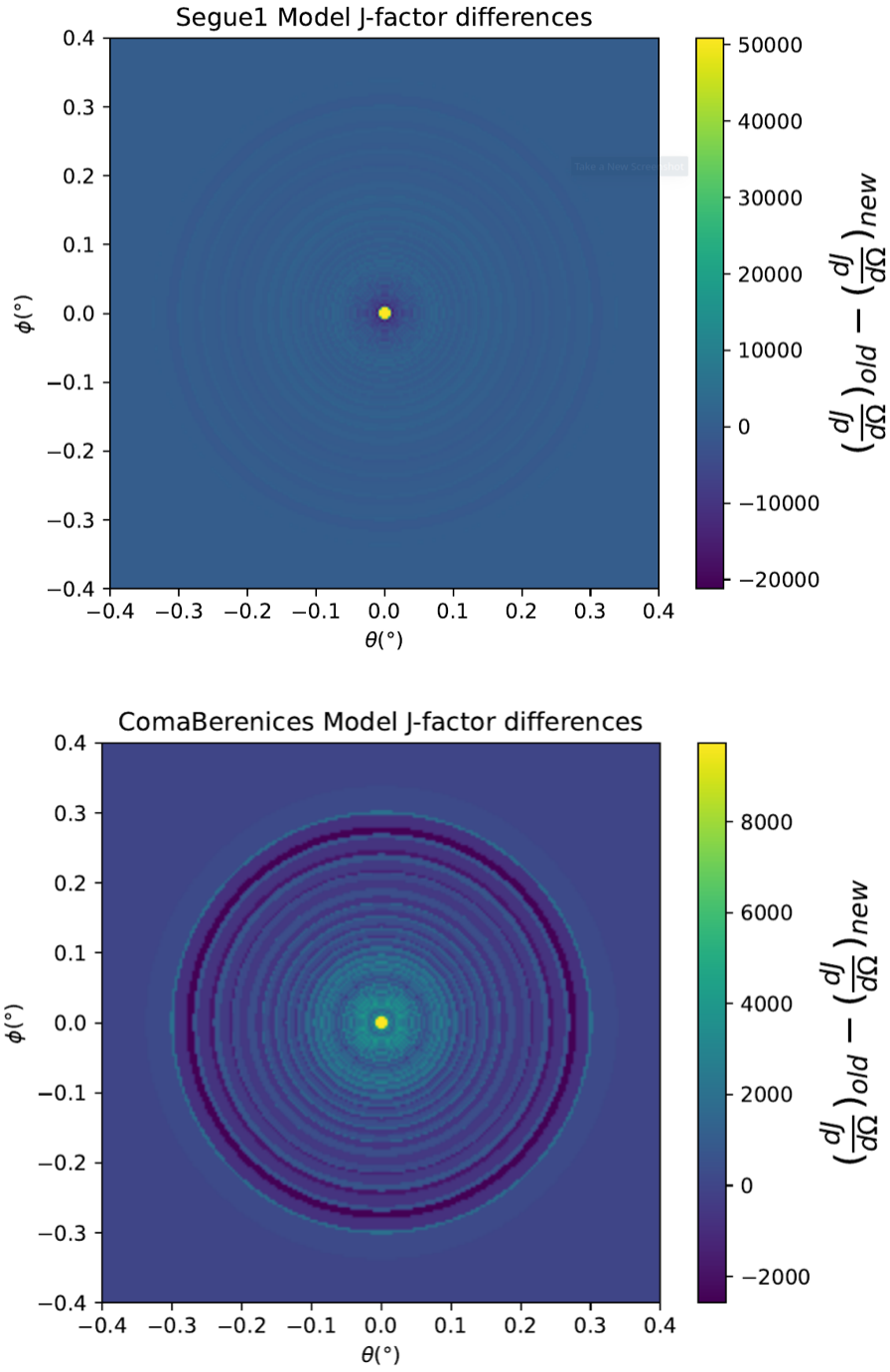


Figure 5.14 Differential map of dJ/Ω from model built in Section 5.8.1 and profiles provided directly from authors. (Top) Differential from Segue1. (bottom) Differential from Coma Berenices. Note that their scales are not the same. Segue1 shows the deepest discrepancies which is congruent with its large uncertainties. Both models show anuli where unique models become apparent.

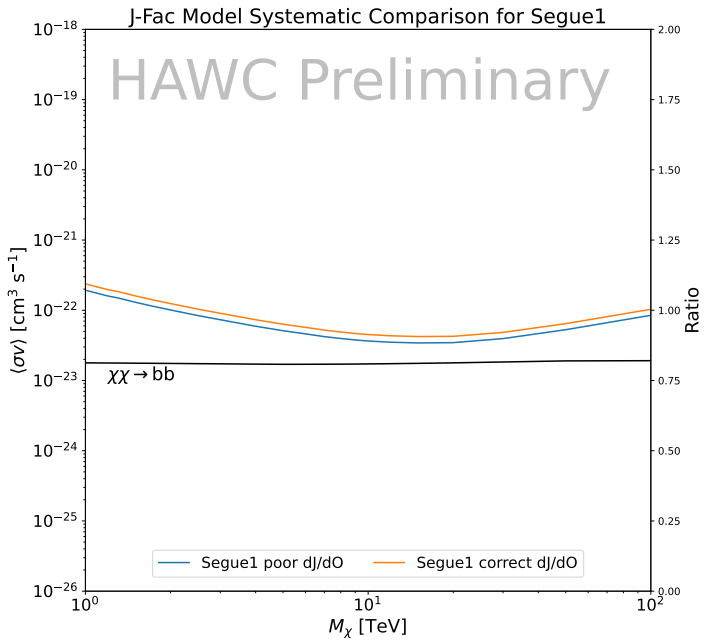
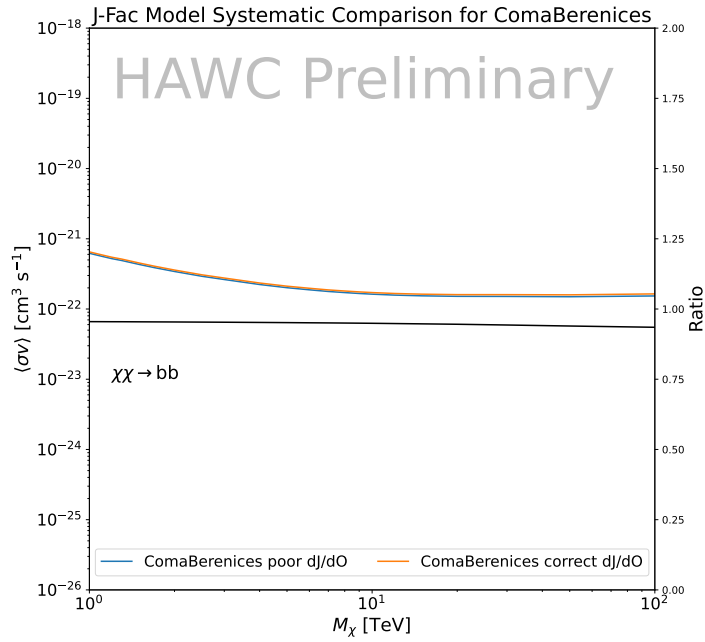


Figure 5.15 HAWC limits for Coma Berenices (top) and Segue1 (bottom) for two different map sets. Blue lines are limits calculated on maps with poor model representation. Orange lines are limits calculated on spatial profiles provided by the authors of [45]. Black line is the ratio of the poor spatial model limits to the corrected spatial models. The left y-axis measures $\langle \sigma v \rangle$ for the blue and orange lines. The right y-axis measures the ratio and is unitless.

1002 dSphs, assuming a dynamic equilibrium and a spherical symmetry for the dSphs. They adopted
1003 the generalized DM density distribution, known as Zhao-Hernquist, introduced by [58], carrying
1004 three additional index parameters to describe the inner and outer slopes, and the break of the
1005 density profile. Such a profile parametrization allows the reduction of the theoretical bias from
1006 the choice of a specific radial dependency on the kinematic data. In other words, the increase of
1007 free parameters with the use of the Zhao-Hernquist profile allows a better description of the mass
1008 density distribution of dark matter.

1009 In addition, a constant velocity anisotropy profile and a Plummer light profile [59] for the stellar
1010 distribution were assumed. The velocity anisotropy profile depends on the radial and tangential
1011 velocity dispersion. However, its determination remains challenging since only the line-of-sight
1012 velocity dispersion can be derived from velocity measurements. Therefore, the parametrization of
1013 the anisotropy profile is obtained from simulated halos (see [60] for more details). They provide the
1014 values of the J -factors of regions extending to various angular radius up to the outermost member
1015 star.

1016 The \mathcal{B} J -factors were computed through a Jeans analysis taking into account the systematic
1017 uncertainties induced by the DM profile parametrization, the radial velocity anisotropy profile, and
1018 the triaxiality of the halo of the dwarf galaxies. They performed a more complete study of the dSph
1019 kinematics and dynamics than \mathcal{GS} for the determination of the J -factor. Conservative values of the
1020 J -factors where obtained using an Einasto DM density profile [61], a realistic anisotropy profile
1021 known as the Baes & Van Hese profile [62] which takes into account that the inner regions can be
1022 significantly non-isotropic, and a Zhao-Hernquist light profile [58].

1023 For both sets, J -factor values are provided for all dSphs as a function of the radius of the
1024 integration region [53, 47, 55]. Table 5.1 shows the heliocentric distance and Galactic coordinates
1025 of the twenty dSphs, together with the two sets of J -factor values integrated up to the outermost
1026 observed star for \mathcal{GS} and the tidal radius for \mathcal{B} . Both J -factor sets were derived through a Jeans
1027 analysis based on the same kinematic data, except for Draco where the measurements of [63] have
1028 been adopted in the computation of the \mathcal{B} value. The computations for producing the \mathcal{GS} and \mathcal{B}

1029 samples differ in the choice of the DM density, velocity anisotropy, and light profiles, for which the
1030 set \mathcal{B} takes into account some sources of systematic uncertainties.

1031 Figure 5.16 and Figure 5.17 show the comparisons for the J -factor versus the angular radius
1032 for each of the 20 dSphs used in this study. The uncertainties provided by the authors are also
1033 indicated in the figures. For the \mathcal{GS} set, the computation stops at the angular radius corresponding
1034 to the outermost observed star, while for the \mathcal{B} set, the computation stops at the angular radius
1035 corresponding to the tidal radius.

1036 5.9 Discussion and Conclusions

1037 In this multi-instrument analysis, we have used observations of 20 dSphs from the gamma-ray
1038 telescopes Fermi-LAT, H.E.S.S., MAGIC, VERITAS, and HAWC to perform a collective DM
1039 search annihilation signals. The data were combined across sources and detectors to significantly
1040 increase the sensitivity of the search. We have observed no significant deviation from the null, no
1041 DM, hypothesis, and so present our results in terms of upper limits on the annihilation cross-section
1042 for seven potential DM annihilation channels.

1043 Fermi-LAT brings the most stringent constraints for continuum channels below approximately
1044 1 TeV. The remaining detectors dominate at higher energies. Overall, for multi-TeV DM mass,
1045 the combined DM constraints from all five telescopes are 2-3 times stronger than any individual
1046 telescope for multi-TeV DM.

1047 Derived from observations of many dSphs, our results produce robust limits given the DM
1048 content of the dSphs is relatively well constrained. The obtained limits span the largest mass
1049 range of any WIMP DM search. Our combined analysis improves the sensitivity over previously
1050 published results from each detector which produces the most stringent limits on DM annihilation
1051 from dSphs. These results are based on deep exposures of the most promising known dSphs with
1052 the currently most sensitive gamma-ray instruments. Therefore, our results constitute a legacy of
1053 a generation of gamma-ray instruments on WIMP DM searches towards dSphs. Our results will
1054 remain the reference in the field until a new generation of more sensitive gamma-ray instruments
1055 begin operations, or until new dSphs with higher J -factors are discovered.

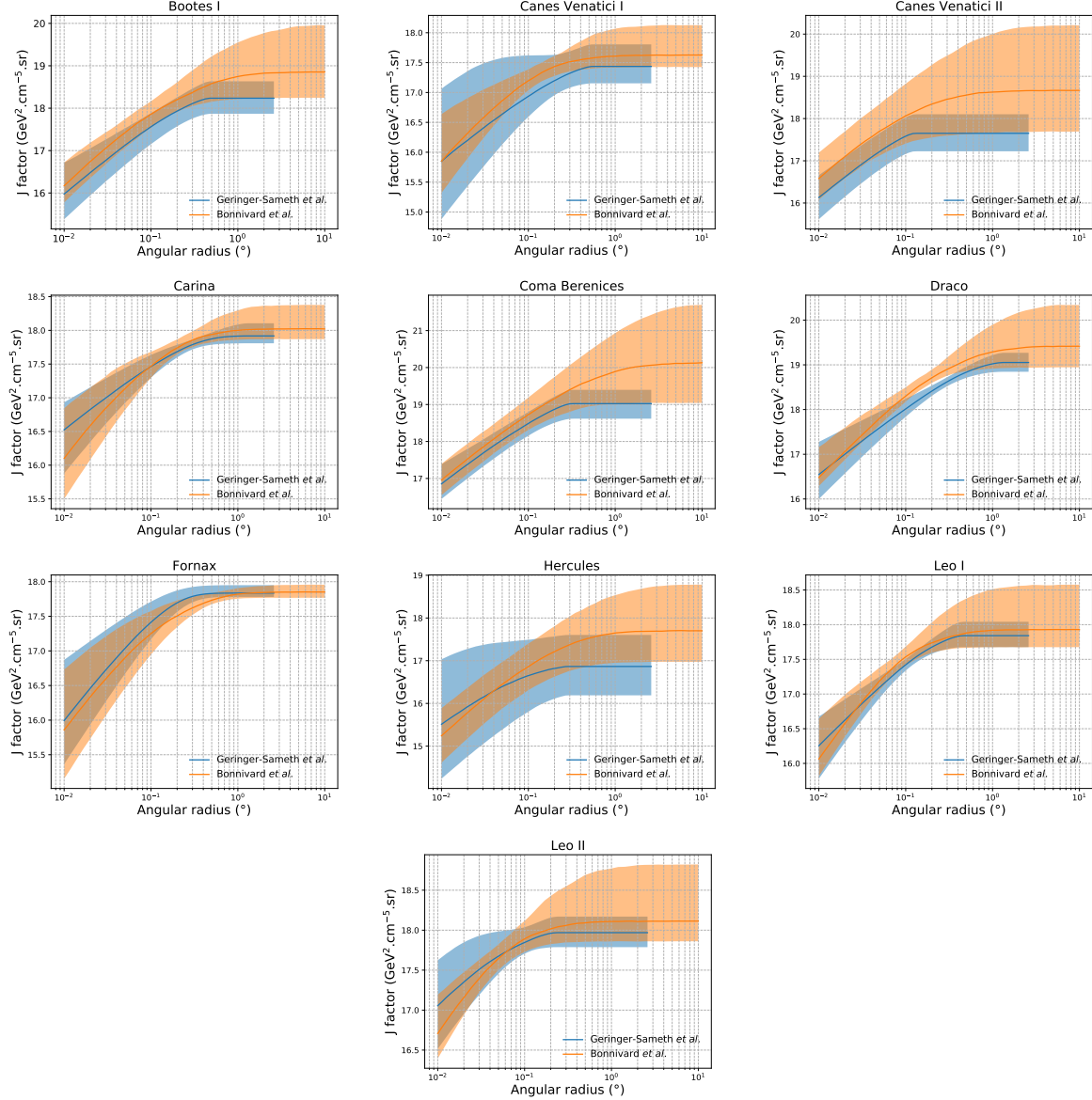


Figure 5.16 Comparisons between the J -factors versus the angular radius for the computation of J factors from Ref. [53] (\mathcal{GS} set in Table 5.1) in blue and for the computation from Ref. [47, 55] (\mathcal{B} set in Tab. 5.1) in orange. The solid lines represent the central value of the J -factors while the shaded regions correspond to the 1σ standard deviation.

This analysis serves as a proof of concept for future multi-instrument and multi-messenger combination analyses. With this collaborative effort, we have managed to sample over four orders in magnitude in gamma-ray energies with distinct observational techniques. Determining the nature of DM continues to be an elusive and difficult problem. Larger datasets with diverse measurement techniques could be essential to tackling the DM problem. A future collaboration using similar

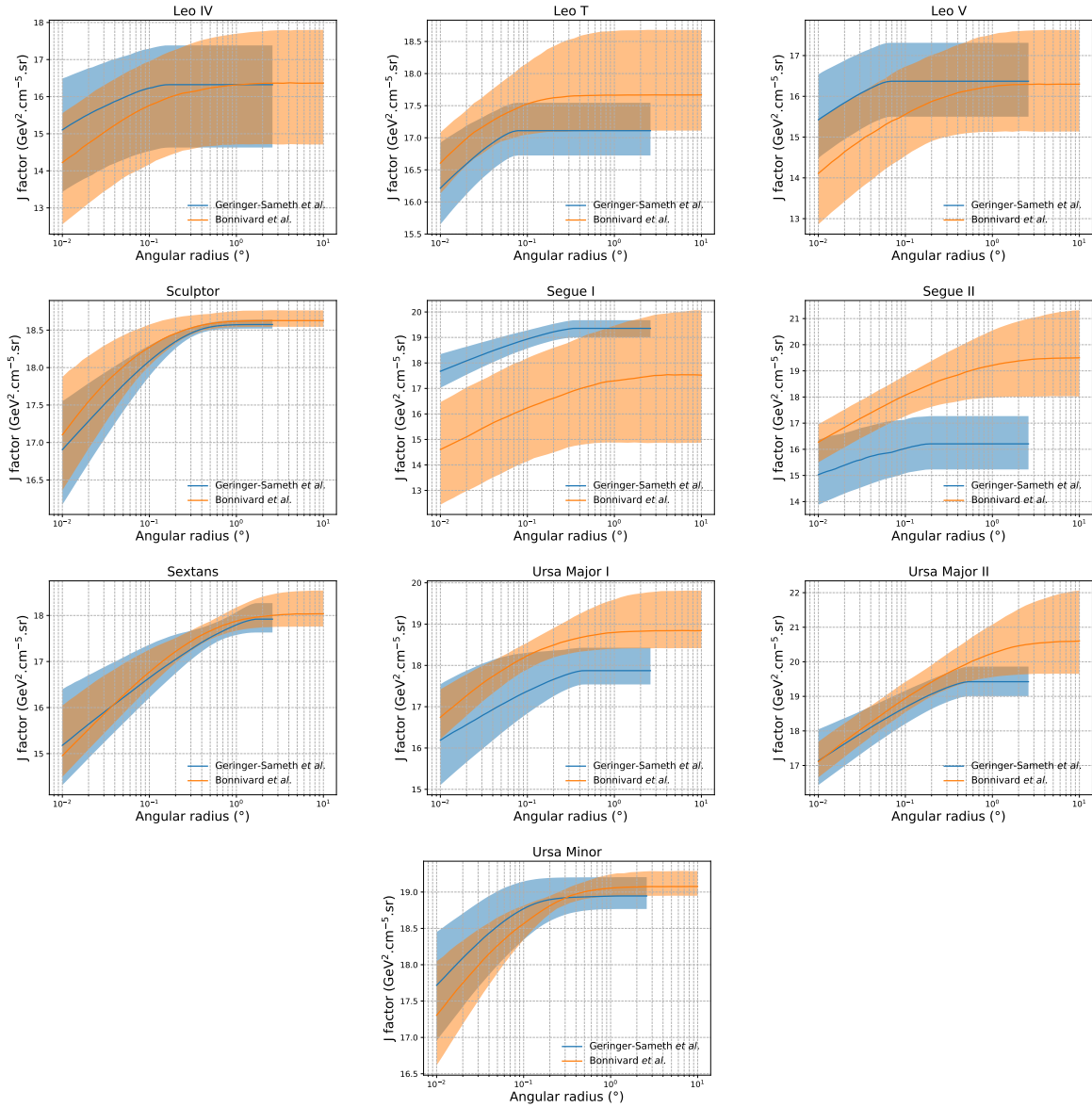


Figure 5.17 Comparisons between the J -factors versus the angular radius for the computation of J factors from Ref. [53] (\mathcal{GS} set in Tab. 5.1) in blue and for the computation from Ref. [47, 55] (\mathcal{B} set in Tab. 5.1) in orange. The solid lines represent the central value of the J -factors while the shaded regions correspond to the 1σ standard deviation.

1061 techniques as the ones described in this paper could grow even beyond gamma rays. The models we
 1062 used for this study include annihilation channels with neutrinos in the final state. Advanced studies
 1063 could aim to merge our results with those from neutrino observatories with large data sets. Efforts
 1064 are already underway to add data from the IceCube, ANTARES, and KM3NeT observatories to
 1065 these gamma-ray results.

1066 From this work, a selection of the best candidates for observations, according to the latest
1067 knowledge on stellar dynamics and modelling techniques for the derivation of the J -factors on
1068 the potential dSphs targets, is highly desirable at the time that new experiments are starting their
1069 dark matter programs using dSphs. Given the systematic uncertainty inherent to the derivation of
1070 the J -factors, an informed observational strategy would be to select both objects with the highest
1071 J -factors that could lead to DM signal detection, and objects with robust J -factor predictions, i.e.
1072 with kinematic measurements on many bright stars, which would strengthen the DM interpretation
1073 reliability of the observation outcome.

1074 This analysis combines data from multiple telescopes to produce strong constraints on astro-
1075 physical objects. From this perspective, these methods can be applied beyond just DM searches.
1076 Almost every astrophysical study can benefit from multi-telescope, multi-wavelength gamma-ray
1077 studies. We have enabled these telescopes to study the cosmos with greater precision and detail.
1078 Many astrophysical searches can benefit from multi-instrument gamma-ray studies, for which our
1079 analysis lays the foundation.

CHAPTER 6

MULTITHREADING HAWC ANALYSES FOR DARK MATTER SEARCHES

6.1 Introduction

HAWC's current software suite, plugins to 3ML, does not fully utilize computational advancements of recent decades. Said advancements include the proliferation of Graphical Processing Units (GPUs), and multithreading on multi-core processors. The analysis described in chapter 5 took up to 3 months of human time waiting for the full gambit of data analysis and simulation of background to run. Additionally, with the addition of a 2D binning scheme, f_{hit} and NN, the compute time is expected to grow. Although excessive computing time was, in part, from an intense use of a shared computing cluster, it was evident that there was room for improvement. In HAWC's next generation dSph DM search, I decided to develop codes that would utilize the multi-core processors on modern high performance computing clusters. The results of this work are featured in this chapter and brought a human timing improvement to computation that scales as $1/N$ where N is the number of threads.

6.2 Dataset and Background

This section enumerates the data and background methods used for HAWC's multi-threaded study of dSphs. Section 6.2.1 and Section 6.2.2 are most useful for fellow HAWC collaborators looking to replicate a multithreaded dSph DM search.

6.2.1 Itemized HAWC files

- Detector Resolution: `refit-Pass5-Final-NN-detRes-zenith-dependent.root`
- Data Map: `Pass5-Final-NN-maptree-ch103-ch1349-zenith-dependent.root`
- Spectral Dictionary: `HDMspectra_dict_gamma.npy`

6.2.2 Software Tools and Development

This analysis was performed using HAL and 3ML [42, 43] in Python version 3. I built software in collaboration with Michael Martin and Letrell Harris to implement the *Dark Matter Spectra from*

1104 *the Electroweak to the Planck Scale* (HDM) [64] and dSphs spatial model from [65] for HAWC
1105 analysis. A NumPy dictionary of HDM was made for Py3. The corresponding Python3 file is
1106 `HDMspectra_dict_gamma.npy`. These files can also be used for decay channels and tools are
1107 provided in HDM’s [git repository](#) [64]. The analysis was performed using the Neural Network
1108 energy estimator for Pass 5.F. A description of this estimator was provided in chapter 3. **TODO:**
1109 **define a subsection when it’s written**, and its key improvements are an improved energy estimation
1110 and improved sensitivities at higher zenith angles. All other software used for data analysis, DM
1111 profile generation, and job submission to SLURM are also kept in my sandbox in the [Dark Matter](#)
1112 [HAWC](#) project. The above repository also incorporates the model inputs used previously in Glory
1113 Duck, described in chapter 5

1114 **6.2.3 Data Set and Background Description**

1115 The HAWC data maps used for this analysis contain 2565 days of data between runs 2104 (
1116 **TODO: Day start**) and 7476 (**TODO: day end**). They were generated from pass 5.f reconstruction.
1117 The analysis is performed using the NN energy estimator with bin list:

1118 B1C0Ea, B1C0Eb, B1C0Ec, B1C0Ed, B1C0Ee, B2C0Ea, B2C0Eb, B2C0Ec, B2C0Ed, B2C0Ee,
1119 B3C0Ea, B3C0Eb, B3C0Ec, B3C0Ed, B3C0Ee, B3C0Ef, B4C0Eb, B4C0Ec, B4C0Ed, B4C0Ee,
1120 B4C0Ef, B5C0Ec, B5C0Ed, B5C0Ee, B5C0Ef, B5C0Eg, B6C0Ed, B6C0Ee, B6C0Ef, B6C0Eg,
1121 B6C0Eh, B7C0Ee, B7C0Ef, B7C0Eg, B7C0Eh, B7C0Ei, B8C0Ee, B8C0Ef, B8C0Eg, B8C0Eh,
1122 B8C0Ei, B8C0Ej, B9C0Ef, B9C0Eg, B9C0Eh, B9C0Ei, B9C0Ej, B10C0Eg, B10C0Eh,
1123 B10C0Ei, B10C0Ej, B10C0Ek, B10C0El

1124 Bin 0 was excluded as it has substantial hadronic contamination and poor angular resolution.

1125 Background considerations and source selection was identical to Section 5.2, and no additional
1126 arguments are provided here. Many of the HAWC systematics explored in Section 5.7 also apply
1127 for this DM search and are not added upon here.

1128 **6.3 Analysis**

1129 The analysis and its systematics are almost identical to Section 5.3. Importantly, we use the
1130 same Equation (5.1) and Equation (5.2) for estimating the gamma-ray flux at HAWC from our
1131 sources. We add on to the previous study with a search for DM decay. The flux equations for DM
1132 decay are

$$\frac{d\Phi_\gamma}{dE_\gamma} = \frac{1}{4\pi\tau m_\chi} \frac{dN_\gamma}{dE_\gamma} \times \int_{\text{source}} d\Omega \int_{l.o.s} \rho_\chi dl(r, \theta') \quad (6.1)$$

1133 with a new quantity, the D factor, defined as

$$D = \int d\Omega \int_{l.o.s} dl \rho_\chi(r, \theta') \quad (6.2)$$

1134 Software was written to accomodate DM decay from dSphs, however decay profiles were not
1135 received from $\mathcal{L}\mathcal{S}$ by the time of writing this tehsis.

1136 **6.3.1 $\frac{dN_\gamma}{dE_\gamma}$ - Particle Physics Component**

1137 For these spectra, we import HDM with Electroweak (EW) corrections and additional correc-
1138 tions for neutrinos above the EW scale [64]. The spectrum is implemented as a model script in
1139 astromodels for 3ML. A comprehensive description of EW corrections and neutrino considerations
1140 are provided later in **TODO: refeance MM nu duck**.

1141 Figure 6.1 demonstrates the impact of changes from HDM on DM annihilation to W bosons.
1142 A class in astromodels was developed to include HDM and is aptly named **HDMspectra** within
1143 **DM_models.py**. The SM DM annihilation channels studied here are $\chi\chi \rightarrow:$

1144 $e^+e^-, \mu^+\mu^-, \tau^+\tau^-, b\bar{b}, t\bar{t}, gg, W^+W^-, ZZ, c\bar{c}, u\bar{u}, d\bar{d}, s\bar{s}, \nu_e\bar{\nu}_e, \nu_\mu\bar{\nu}_\mu, \nu_\tau\bar{\nu}_\tau, \gamma\gamma, hh.$

1145 For $\gamma\gamma$ and ZZ , a substantial fraction of the signal photons are expected to have total energy equal
1146 m_χ [64]. This introduces a δ -function that is much narrower than the energy resolution of the
1147 HAWC detector. To ensure that this feature is not lost in the likelihood fits, the 'line' feature is
1148 convolved with a gaussian kernel with a 1σ width of $0.05 \cdot m_\chi$ and total kernel window of $\pm 4\sigma$.
1149 This difers from HAWC's previous line study where 30% of HAWC's energy resolution was used
1150 for the kernel [66]. The NN energy estimator's strength compared to f_{hit} at low gamma-ray energy

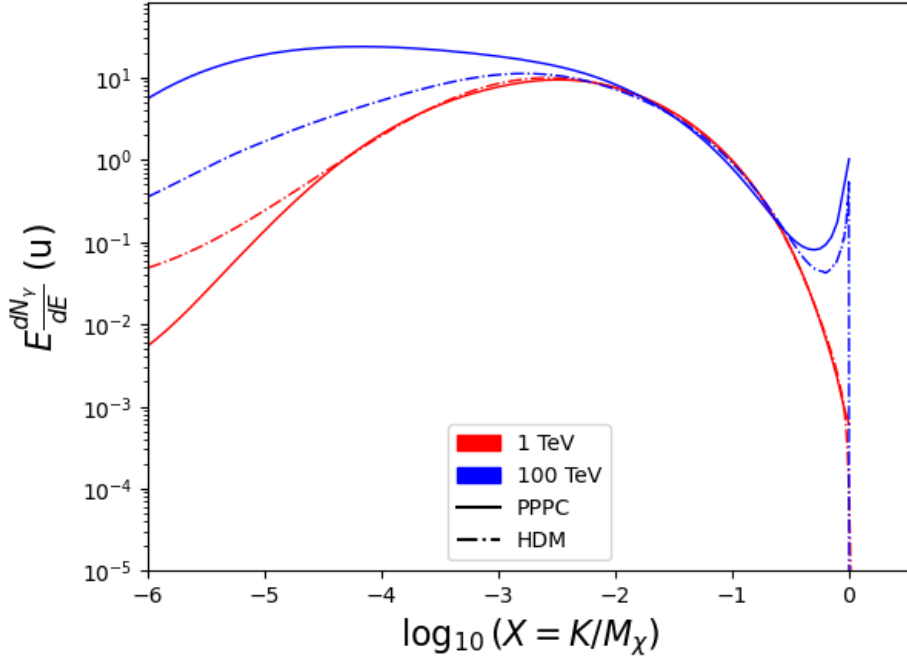


Figure 6.1 Difference between spectral hypotheses from PPPC [44] and HDM [64]. Shown is the expected DM annihilation spectrum for $\chi\chi \rightarrow W^-W^+$. Solid lines are spectral models with EW corrections from the PPPC. Dash-dot lines are spectral models from HDM. Red lines are models for $M_\chi = 1$ TeV. Blue lines represent models for $M_\chi = 100$ TeV.

enables smaller resolutions in addition to low energy tails in the spectral models [64]. $\chi\chi \rightarrow \gamma\gamma$ and ZZ spectral hypotheses are shown in Figure 6.2. Spectral models for the remaining annihilation channels are plotted for each m_χ in Figure B.1.

6.3.2 J and D- Astrophysical Components

The J-factor profiles for each source are imported from Louis Strigari et al. (referred to with \mathcal{LS}) [65]. Profiles in $\frac{dJ}{d\Omega}(\theta)$ up to $\theta = 0.5^\circ$ were provided directly from the authors. Map generation from these profiles were almost identical to Section 5.3.2 except that a higher order trapezoidal integral was used for the normalization of the square, uniformly-spaced map:

$$p^2 \cdot \sum_{i=0}^N \sum_{j=0}^M w_{i,j} \frac{d\mathcal{K}}{d\Omega}(\theta_{i,j}, \phi_{i,j}) \quad (6.3)$$

\mathcal{K} is either J or D for the spatial distributions of annihilation or decay respectively. p is the angular side of one pixel in the map. $w_{i,j}$ is a weight assigned the following ways:

$w_{i,j} = 1$ if $(\theta_{i,j}, \phi_{i,j})$ is fully within the region of integration

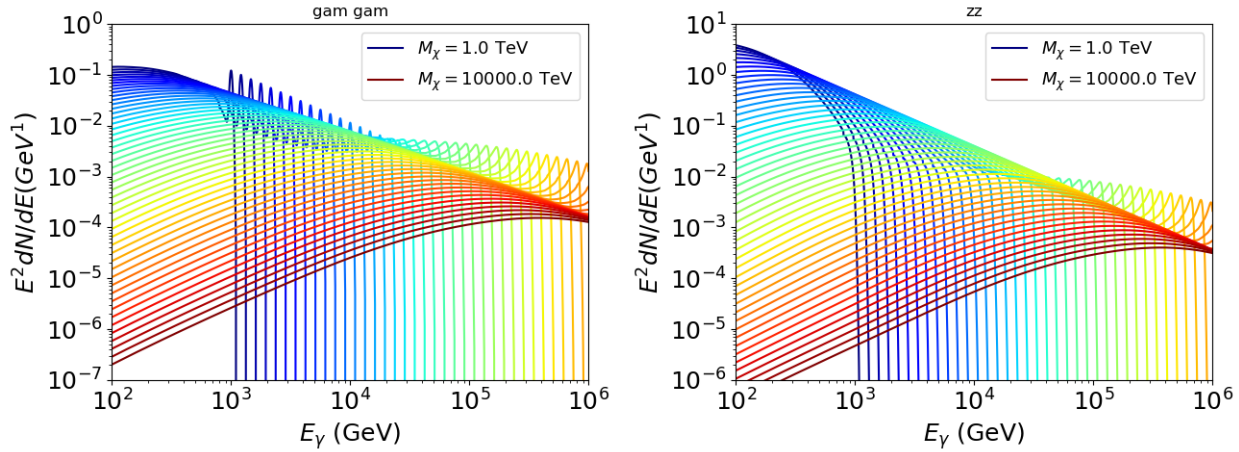


Figure 6.2 Photon spectra for $\chi\chi \rightarrow \gamma\gamma$ (left) and $\chi\chi \rightarrow ZZ$ (right) after gaussian convolution of line features. Both spectra have δ -features at photon energies equal to the DM mass. Bluer lines are annihilation spectra with lower DM mass. Redder lines are spectra from larger DM mass. All Spectral models are sourced from the Heavy Dark Matter models [64]. Axes are drawn roughly according to the energy sensitivity of HAWC.

1162 $w_{i,j} = 1/2$ if $(\theta_{i,j}, \phi_{i,j})$ is on an edge of the region of integration

1163 $w_{i,j} = 1/4$ if $(\theta_{i,j}, \phi_{i,j})$ is on a corner of the region of integration

1164 Figure 6.3 shows the median and $\pm 1\sigma$ maps used as input for DM annihilation studied by \mathcal{LS} .

1165 **6.3.3 Source Selection and Annihilation Channels**

1166 HAWC's sources for this multithreaded analysis include Coma Berenices, Draco, Segue 1, and
 1167 Sextans \mathcal{LS} observes up to 43 sources in its publication, however only 4 of the best fit profiles were
 1168 provided at the time this thesis was written. A full description of each source used in this analysis
 1169 is found in Table 6.1.

1170 This analysis improves on chapter 5 in the following ways. Previously, the particle physics
 1171 model used for gamma-ray spectra from DM annihilation was from the PPPC [44] which missed
 1172 important considerations relevant for the neutrino sector. HDM is used to account for this shortfall
 1173 [64]. HDM also models DM to the Planck scale which permits HAWC to probe PeV scale DM.
 1174 For this study, we sample DM masses: 1 TeV - 10 PeV with 6 mass bins per decade in DM mass.
 1175 In the case of line spectra ($\chi\chi \rightarrow \gamma\gamma$, or ZZ), we double the mass binning to 12 DM mass bins
 1176 per decade in DM mass. A larger source catalog is used that uses a Navarro–Frenk–White (NFW)

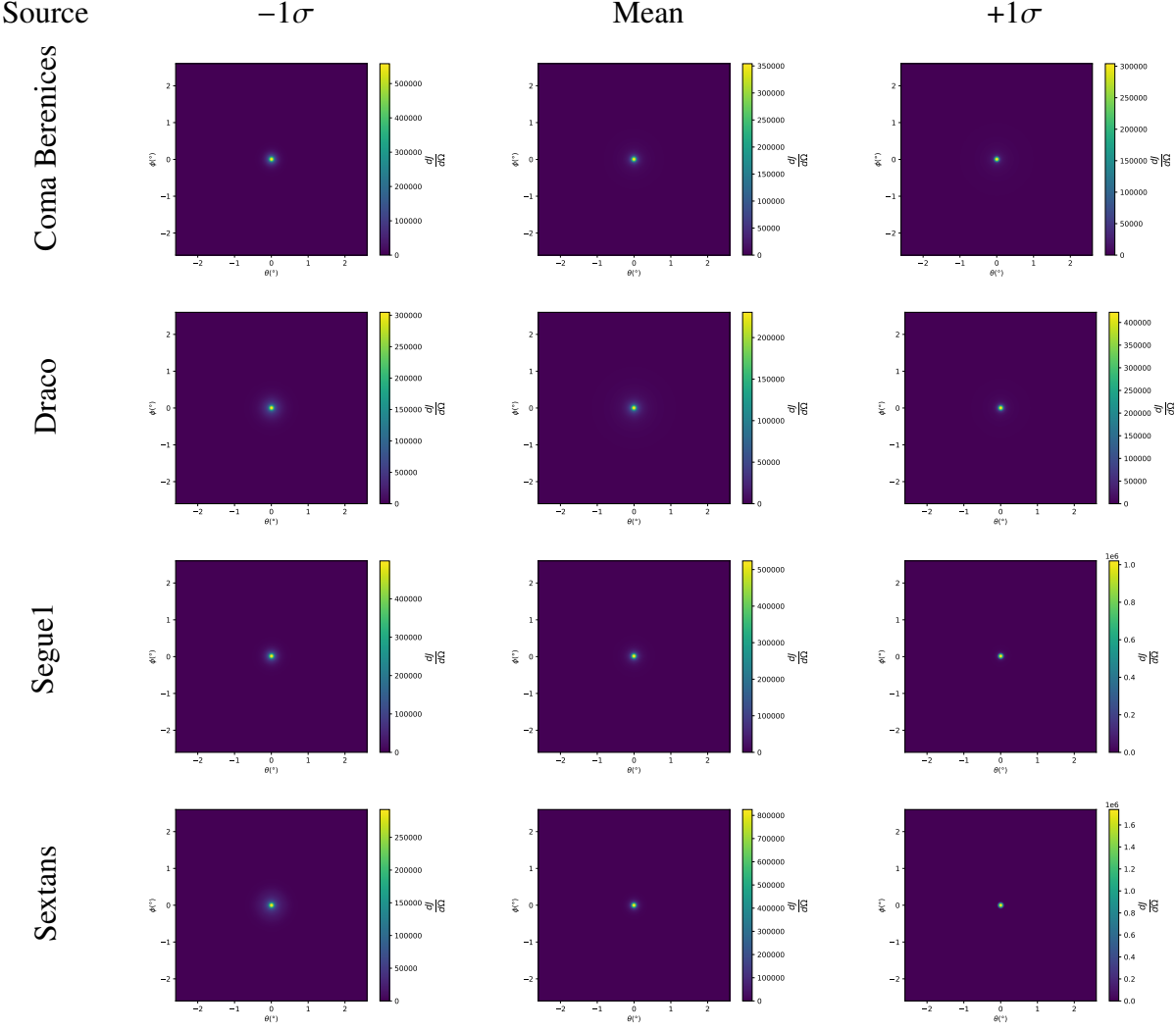


Figure 6.3 $\frac{dJ}{d\Omega}$ maps for Coma Berenices, Draco, Segue1, and Sextans. Columns are divided for the $\pm 1\sigma$ uncertainties in $dJ/d\Omega$ around the mean value from \mathcal{LS} [65]. Origin is centered on the specific dwarf spheroidal galaxies (dSph). θ and ϕ axes are the angular separation from the center of the dwarf

1177 spatial DM distribution from \mathcal{LS} [65]. Because NFW has fewer parameters than what is used
 1178 for \mathcal{GS} , \mathcal{LS} is able to fit ultra-faint dwarves, expanding the number of sources available for DM
 1179 searches. Finally, the gamma-ray ray dataset is much larger. The study performed here analyzes
 1180 2565 days of data compared to 1017 days analyzed in chapter 5.

1181 6.4 Likelihood Methods

1182 These are identical to Section 5.4.1 and no additional changes are made to the likelihood. Bins
 1183 in this analysis are expanded to include HAWC’s NN energy estimator.

1184 **6.5 Computational Methods: Multithreading**

1185 Previously, as in Section 5.3, the likelihood was minimized for one model at a time. One
 1186 model in this case representing a DM annihilation channel, DM mass, and dSph. In an effort
 1187 to conserve human and CPU time, jobs submitted for high performance computing contained a
 1188 list of DM masses to iterate over for likelihood fitting. Jobs were then trivially parallelized for
 1189 each permutation of the two lists: CHANS (SM annihilation channel) and SOURCES (dSph spatial
 1190 templates). The lists for CHANS and SOURCES are found in Section 6.3.1 and Table 6.1, respectively.
 1191 Initially, 11 DM mass bins were serially sampled for one job defined by a [SM channel, dSph] set.
 1192 Computing the likelihoods would take between 1.5 to 2 hrs, stocastically, for a job. We expect to
 1193 compute likelihoods for data and 300 Poisson background trials. The estimated CPU time based on
 1194 the above for all SM annihilation channels (17) and 25 sources (all \mathcal{LS} sources withing HAWC's
 1195 field of view) amounted to 127,925 jobs. In total, 1,407,175 likelihood fits and profiles would be
 1196 computed for the 11 mass bins we wished to study. The estimated CPU time ranged between 10k
 1197 CPU days - 8k CPU days. Human time is more challenging to estimate as job allocation is stochastic
 1198 and highly dependant on what other users are submitting, yet it is unlikely that all jobs would run
 1199 simultaneously. Therefore we can expect human time to be about as long as was seen in chapter 5
 1200 which was on the order of months to fully compute on a smaller analysis. A visual aid to describe
 1201 how jobs were organized is provided in Figure 6.4.

Name	Distance (kpc)	l, b ($^{\circ}$)	$\log_{10} J$ (\mathcal{LS} set) $\log_{10}(\text{GeV}^2\text{cm}^{-5}\text{sr})$
Coma Berenices	44	241.89, 83.61	$19.00^{+0.36}_{-0.35}$
Draco	76	86.37, 34.72	$18.83^{+0.12}_{-0.12}$
Segue I	23	220.48, 50.43	$19.12^{+0.49}_{-0.58}$
Sextans	86	243.50, 42.27	$17.73^{+0.13}_{-0.12}$

Table 6.1 Summary of the relevant properties of the dSphs used in the present work. Column 1 lists the dSphs. Columns 2 and 3 present their heliocentric distance and galactic coordinates, respectively. Column 4 reports the J -factors of each source given from the \mathcal{LS} studies and estimated $\pm 1\sigma$ uncertainties. The values $\log_{10} J$ (\mathcal{LS} set) [65] correspond to the mean J -factor values for a source extension truncated at 0.5° .

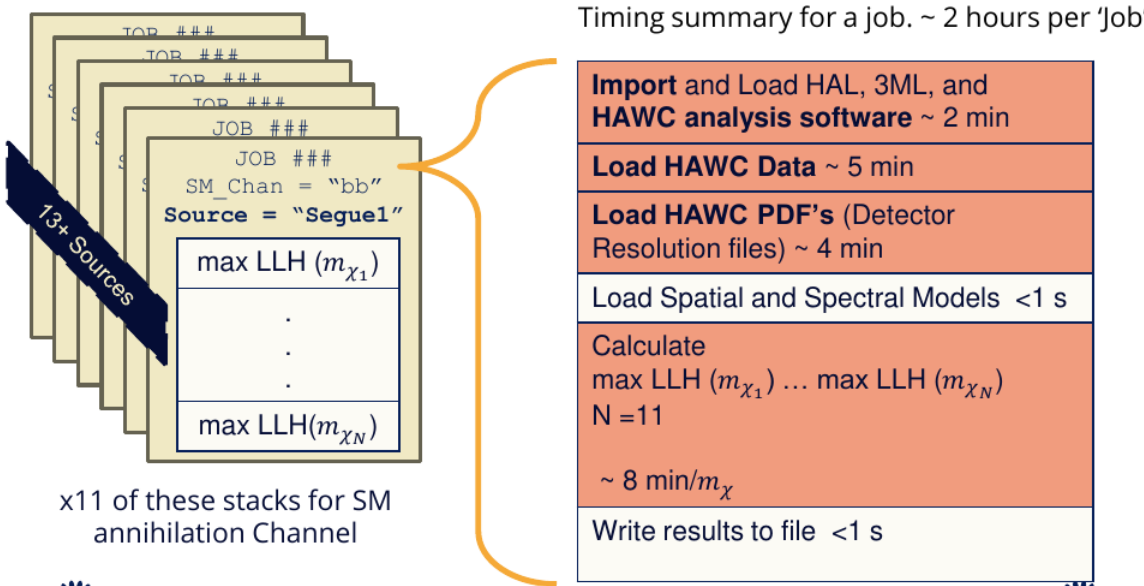


Figure 6.4 Infographic on how jobs and DM computation was organized in Section 5.3. Jobs were built for each permutation of CHANS and SOURCES shown by the left block in the figure. Each job, which took on the order 2 hrs to compute, had the following work flow: 1. Import HAWC analysis software, 2 min to run. 2. Load HAWC count maps, 5 min to run. 3. Load HAWC energy and spatial resolutions, 4 min. 5. Load DM spatial source templates and spectral models, less than 1 s. 6. Perform likelihood fit on data and model, about 8 min per DM mass. 7. Write results to file, less than 1s.

1202 The computational needs for this next generation DM analysis are extreme and is unlike other
 1203 analyses performed on HAWC. It became clear that there was a lot to gain from optimzing how
 1204 the likelihoods are computed. This section discusses how multi-threading was applied to solve and
 1205 reduce HAWC's computing of likelihoods for large parameter spaces like in DM searches.

1206 6.5.1 Relevant Foundational Information

1207 The profiling of the likelihood for HAWC is done via gradient descent where the nomarilization
 1208 of Equation (5.1) (linearly correlated with $\langle \sigma v \rangle$) is rescaled in the descent. Additionaly, we sample
 1209 the likelihood space for a defined list of $\langle \sigma v \rangle$'s described in Section 5.4.2. The time to compute
 1210 these values is not predictable or consistent because many variables can change across the full
 1211 model-space. comprehensively, these variables are:

- 1212 • m_{χ} : DM rest mass
- 1213 • CHAN : DM SM annihilation channel.

1214 • SOURCE : dSph within HAWC's field of view. This involves a spatial template AND coordinate
1215 in HAWC data.

1216 • $\langle\sigma v\rangle$: Effectevly the flux normalization and free parameter in the likelihood fit.

1217 Therefore, we develop an asynchronous, functional-parallel coding pattern. Asynchronous meaning
1218 that the instructions and computing within a function are independent and permitted to be out of sync
1219 with sibling computations. Functional-parallel meaning that instructions are the subject of parral-
1220 lelization rather than threading the likelihood computation. This is close to trivial parametrization
1221 seen in Figure 6.4 except that we seek to consolidate the loading stages (software, data, and detector
1222 resolution loading). Reducing the total instances of loading stages and distributing access to the
1223 reduced loads across multiple asynchronous threads is expected to reduce serial processing time and
1224 the overhead implicit to each job in addition to saving human time.

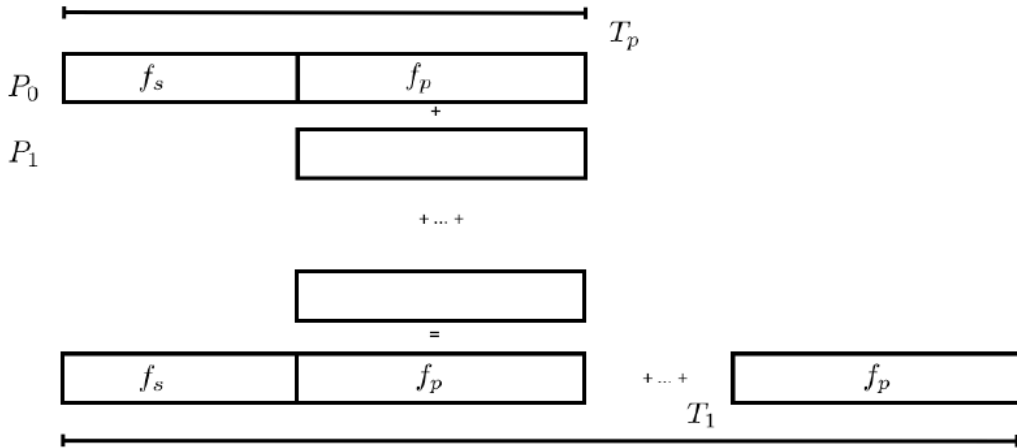


Figure 6.5 Graphic of Gustafson parallel coding pattern. f_s is the fraction of a program, in time, spent on serial computation. f_p is the fraction of computing time that is parallelizable. T_p is the total time for a parallel program to run. T_1 is the total time for a parallel program to run if only 1 processor is allocated. P_N is the N -th processor where it's row is the computation the processor performs. The Gustafson pattern is most similar to what is implemented for this analysis. Figure is pulled from [67].

1225 We need a way to measure and compare the expected speedup and efficiency gain for this
1226 asynchronous coding pattern. I pull inspiration for timing measurement from [67] and use *Amdahl's
1227 law with hybrid programming*. Hybrid programming meaning that the computation is a mix of

1228 distributed and shared memory programming. If we assume the code is fully parallelizable over p
1229 processors and c threads, the ideal speedup is simply pc and ideal run-time is $T_1/(pc)$. T_1 is the
1230 total time for a parallel program to run if only 1 processor is allocated. However, the coding pattern
1231 contains some amount of unavoidable serial computation, as shown in Figure 6.5. In our case, the
1232 run time is estimated to be

$$T_{p,c} = \frac{T_1}{pc} (1 + F_s(c - 1)). \quad (6.4)$$

1233 F_s is the fraction of CPU time dedicated to serial computation. The expected speedup is

$$S_{p,c} \equiv \frac{T_1}{T_{p,c}} = \frac{pc}{1 + F_s(c - 1)}. \quad (6.5)$$

1234 From Equation (6.5), we can see that the speed up scales with p/F_s . We are free to minimize
1235 F_s asymptotically by enlarging the total models that are submitted to the thread pool, thereby
1236 shrinking the CPU fraction dedicated to serial operation. We are also free to define exactly how
1237 many threads and processors we utilize, yet eventually hit a hard cap at the hardware available on
1238 our computing cluster. HAWC uses Intel Xeon processors with 48 cores and 96 threads. This
1239 means when N-threads (c) are defined, $N \bmod 2$ cores (p) are needed. We see that a successful
1240 code scales well as the expected speedup is inversely correlated with F_s . As the total number of
1241 models sampled grows, the speedup will also.

1242 6.5.2 Implementation

1243 The multithreaded code was written in Python3 and is documented in the `dark_matter_hawc`
1244 [repository](#) within the script named `mpu_analysis.py`. A version of the script as of April 25
1245 **TODO: make sure to update on this date** is also provided in Section B.2 It has many dependancies
1246 including the HAWC analysis software. Figure 6.6 displays the workflow of a job with 3 threads.
1247 Within a job, SOURCE is kept fixedh . CHAN(S) remains 17 elements long. More m_χ are sampled
1248 from 11 bins up to 49 (for $\gamma\gamma$ and ZZ) and 25 (for remaining CHANS) which amounts to 12 or 6
1249 mass bins per decade. The DM mass, m_χ , and SM annihilation channels, CHANS, are permuted into
1250 a 473 element list which is split evenly across N threads where N ranges between 5 - 16. Within a
1251 thread, for each m_χ -CHAN tuple, 1001 $\langle\sigma v\rangle$ values are sampled in the likelihood, and the value of

Timing summary for a multi-threaded job.

Import and Load HAL, 3ML, and HAWC analysis software ~ 2 min		
Load HAWC Data ~ 5 min		
Load HAWC PDF's (Detector Resolution files) ~ 4 min		
Load Spatial Model < 1s		
Load Spectra Models <1 s	Load Spectra Models <1 s	Load Spectra Models <1 s
Calculate max LLH (Chan_0, m_{χ_1}) ... max LLH (Chan_?, m_{χ_N}) N = TOTAL/N_THREADS ~ 8 min/Spec_model	Calculate max LLH (Chan_?, m_{χ_1}) ... max LLH (Chan_?, m_{χ_N}) N = TOTAL/N_THREADS ~ 8 min/Spec_model	Calculate max LLH (Chan_?, m_{χ_1}) ... max LLH (Chan_?, m_{χ_N}) N = TOTAL/N_THREADS ~ 8 min/Spec_model
Write results to file <1 s	Write results to file <1 s	Write results to file <1 s
Join Threads and terminate < 1s		

Figure 6.6 Task chart for one multi-threaded job developed for this project. Green blocks indicate a shared resource across the threads AND computation performed serially. Red blocks indicate functional parallel processing within each thread. 3 threads are represented here, yet many more can be employed during the full analysis. Jobs are defined by the SOURCE as these require unique maps to be loaded into the likelihood estimator. The m_{χ} , CHAN, and $\langle \sigma v \rangle$ variables are entered into the thread pool and allocated as evenly as possible across the threads.

1252 $\langle \sigma v \rangle$ that maximizes the likelihood is found. Although rare, fits that failed are handled on a case
1253 by case basis.

1254 6.5.3 Performance

M Tasks	$T_{p,c}$ (hr:min:s)			
	$T_{1,1}$	$T_{1,2}$	$T_{1,8}$	$T_{1,16}$
50	1:40:37.5	0:52:43.7	0:19:13.8	0:13:44.0
74	2:22:30.0	1:15:00.6	0:25:21.3	0:15:49.8
100	(3:07:51.9)	1:40:10.5	0:30:44.4	0:20:01.4
200	(6:02:20.6)	-	1:00:32.0	0:30:35.0
473	(13:58:40.3)	-	TODO: run this	1:07:53.2

Table 6.2 Timing summaries for analyses for serial and multithreaded processes. M tasks is the number of functional-parallel tasks ran for the computation. $T_{p,c}$ is a single run time in hours:minutes:seconds for runs utilizing p nodes and c threads. Runs are run interactively on the same computer to maximize consistency. Empty entries are indicated with '-'. (·) entries are estimated entries extrapolated from data earlier in the column.

1255 We see a tremendous reduction to human time waiting for our dSph analyses to run. Table 6.2

1256 shows the timing summaries for analyses of different sizes and thread counts. Additionally, the
 1257 efficiency gained when consolidating the serial loading of data is also apparent in our ability to
 1258 study many more tasks in about the same amount of wall time as a smaller serial computation. Trials
 1259 represented in the table were run on an AMD Opteron® processor 6344 with 48 cores, 2 threads
 1260 per core; 2.6 GHz clock. This is not the same architecture used for analysis on the computing
 1261 cluster however they are similar enough that results shown here are reasonably representative of
 1262 computing on the HAWC computing cluster. I use the Tab. 6.2 for the inferences and conclusions
 1263 in the following paragraphs.

1264 First, we want to find T_s , the time of serial computation. From Fig. 6.5, the timing for our
 1265 coding pattern can be written as

$$T_s + Mt_p = T_{1,1}^M. \quad (6.6)$$

1266 M is the number of functional-parallel tasks (represented as column 1 of Tab. 6.2), and t_p is the
 1267 average time to complete a single parallel task. $T_{1,1}^M$ is the total time for a parallel program to run if
 1268 only 1 processor is allocated for M parallel task. With two runs of different M ($M1$ and $M2$), we
 1269 can use a system of equations to derive

$$T_s = T_{1,1}^{M1} - M1 \left(\frac{T_{1,1}^{M1} - T_{1,1}^{M2}}{M1 - M2} \right). \quad (6.7)$$

1270 We also extract t_p using the same methods:

$$t_p = \frac{T_{1,1}^{M1} - T_{1,1}^{M2}}{M1 - M2}. \quad (6.8)$$

1271 From Tab. 6.2, we set $M1 = 50$ and $M2 = 74$ and take their corresponding $T_{1,1}$ from the table to
 1272 calculate T_s and t_p .

$$T_s = 803.1\text{s} \text{ and } t_p = 104.6\text{s} \quad (6.9)$$

1273 Now, we have specific estimation for the fraction of serial computing time, F_s :

$$F_s = \frac{803.1}{803.1 + 104.6 \cdot M}. \quad (6.10)$$

1274 The maximum M for this study is 473 which evaluates using Eq. (6.10): $F_s = 0.016$ or 1.6% of
 1275 computing time. Table 6.3 shows the resulting speedups.

M Tasks	F_s	$S_{1,2}$	$S_{1,8}$	$S_{1,16}$
50	1.33 E-1	1.90 [1.76]	5.23 [4.14]	6.35 [5.34]
74	9.40 E-2	1.90 [1.83]	5.62 [4.82]	9.00 [6.64]
100	7.13 E-2	1.88 [1.87]	6.11 [5.34]	9.38 [7.73]
200	3.70 E-2	- [1.93]	5.98 [6.36]	11.85 [10.29]
473	1.60 E-2	- [1.97]	[7.20]	12.35 [12.91]

Table 6.3 Speed up summaries for analyses for serial and multithreaded processes. M tasks is the number of functional-parallel tasks ran for the computation. $S_{p,c}$ is a single speedup comparison for runs utilizing p nodes and c threads. [·] are the estimated speedups calculated from Tab. 6.2, Eq. (6.10), and Eq. (6.5). Empty entries are indicated with '-'.

1276 We see a speedup that generally exceeds expectations from Eq. (6.5) for real trail runs. We also
 1277 see that there are diminishing returns as the number of threads increases. For small jobs with large c ,
 1278 both the expected and observed speedup are significantly smaller than c . One thing not considered
 1279 in Eq. (6.5) is the time incurred via communication latency. Communication latency increases
 1280 with the number of threads and contributes to diminishing returns. Additionally, these values are
 1281 for single runs and do not consider the stochastic variation expected in a shared high performance
 1282 computing resource. Therefor, these results are not strictly conclusive, yet demonstrate the merits
 1283 of multi-threading. We see very clearly that there is a lot to gain, and this new coding pattern will
 1284 expand HAWC's analysis capabilities.

1285 **6.6 Analysis Results**

1286 3 of the 43 \mathcal{LS} dSphs considered for the multithreaded analysis. These dSph are analyzed for
 1287 emission from DM annihilation according to the likelihood method described in Section 5.4. The 3
 1288 likelihood profiles are then stacked to synthesize a combined limit on the dark matter cross-section,
 1289 $\langle\sigma v\rangle$. This combination is done for the 17 SM annihilation channels. Figure 6.7 and Fig. 6.8 show
 1290 the combined limits for all annihilation channels with HAWC's observations. Test statistics of the
 1291 best fit $\langle\sigma v\rangle$ values for each DM mass and SM annihilation channels are shown in Fig. 6.9 and
 1292 Fig. 6.10. We also compare these limits to HAWC's Glory Duck limits shown in Section 5.5. The
 1293 comparison to Glory Duck are featured in Fig. 6.11 for all the DM annihilation channels studied
 1294 for Glory Duck. A full comparison is provided in the appendix in Fig. B.2, Fig. B.3, and Fig. B.4.
 1295 Here, we show updated limits for $\chi\chi \rightarrow b\bar{b}, e\bar{e}, \mu\bar{\mu}, \tau\bar{\tau}, t\bar{t}, W^+W^-$, $\gamma\gamma$ and ZZ . For the first time

1296 ever, we show limits for $\chi\chi \rightarrow c\bar{c}$, $s\bar{s}$, $u\bar{u}$, $d\bar{d}$, $\nu_e\bar{\nu}_e$, $\nu_\mu\bar{\nu}_\mu$, $\nu_\tau\bar{\nu}_\tau$, gg , and hh .

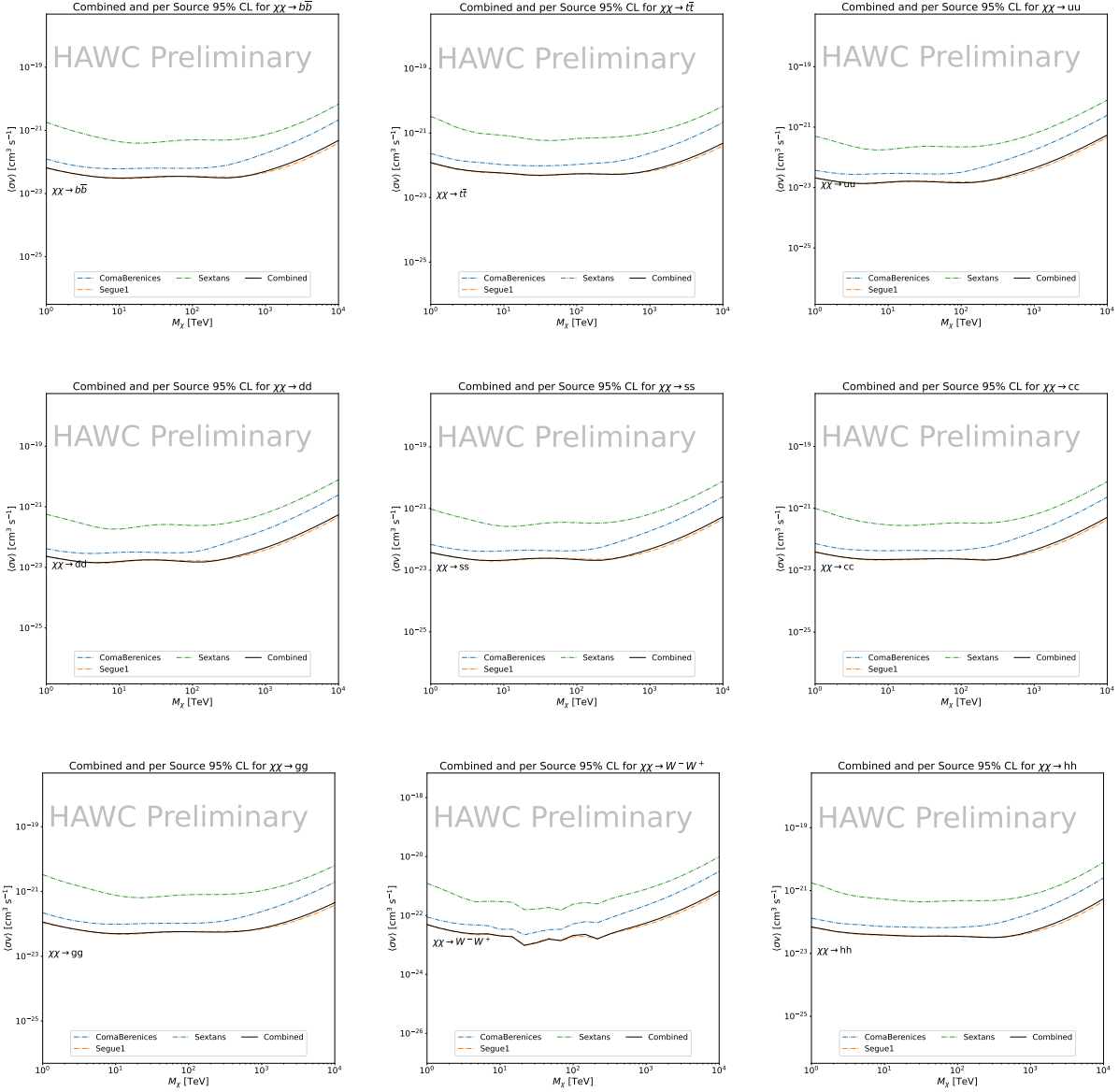


Figure 6.7 HAWC upper limits at 95% confidence level on $\langle\sigma v\rangle$ versus DM mass for $\chi\chi \rightarrow b\bar{b}$, $t\bar{t}$, $u\bar{u}$, $d\bar{d}$, $s\bar{s}$, $c\bar{c}$, gg , W^+W^- , and hh . Limits are with \mathcal{LS} J -factors [65]. The solid line represents the observed combined limit. Dashed lines represent limits from individual dSphs.

1297 No DM was found in HAWC observations. The largest excess found in HAWC data was for DM
 1298 annihilating to W -bosons for $m_\chi = 10\text{TeV}$ at 2σ . HAWC's limits and acesses are dominated by
 1299 Segue1. Coma Berenices shows excess at higher DM mass, yet no similar excesses were observed
 1300 in Segue1. Sextans did not contribute significantly to signal excess or the combined limit as it is

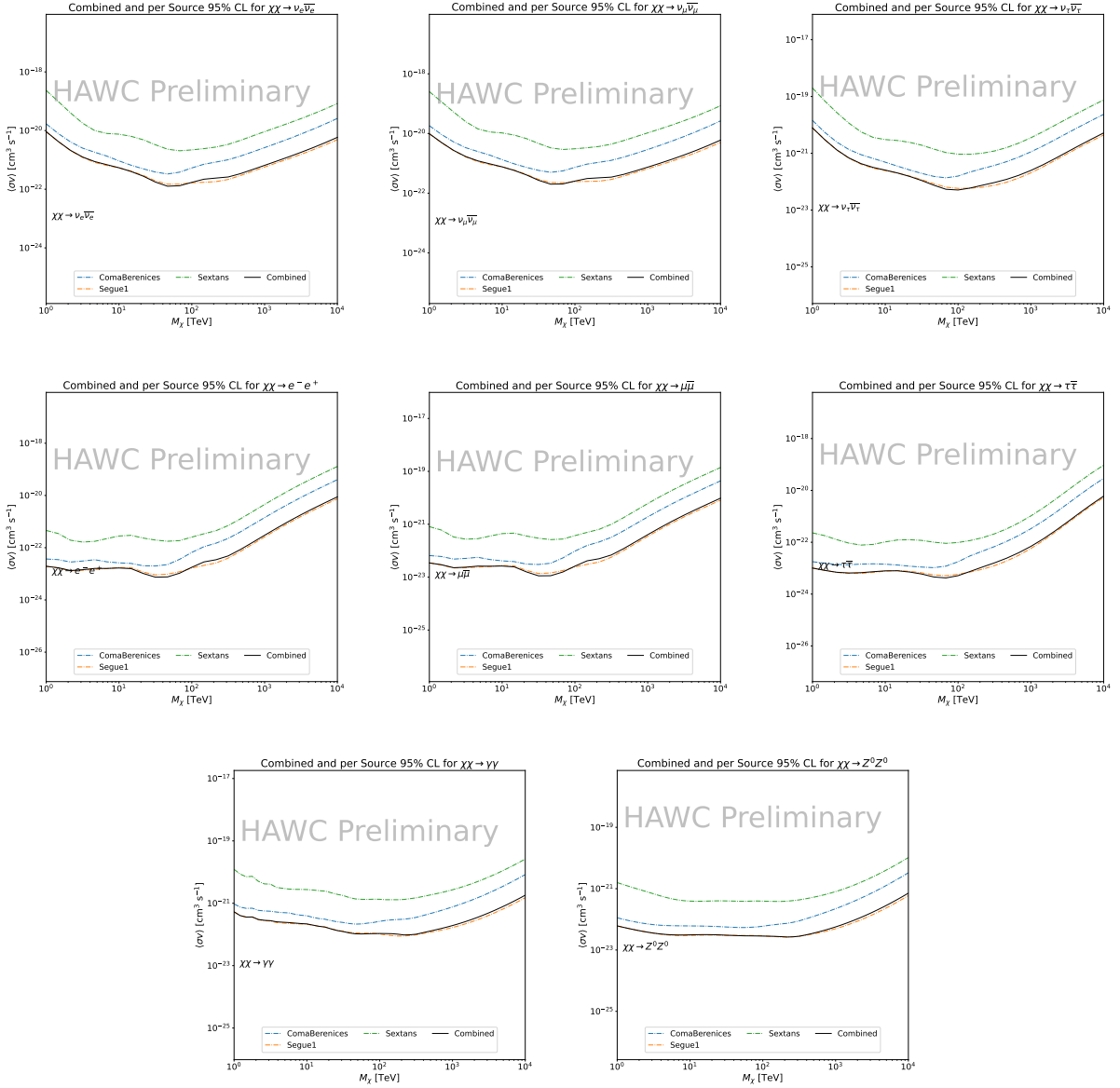


Figure 6.8 HAWC upper limits at 95% confidence level on $\langle\sigma v\rangle$ versus DM mass for $\chi\chi \rightarrow \nu_e \bar{\nu}_e$, $\nu_\mu \bar{\nu}_\mu$, $\nu_\tau \bar{\nu}_\tau$, $e^- e^+$, $\mu \bar{\mu}$, $\tau \bar{\tau}$, $\gamma \gamma$ and ZZ . Limits use $\mathcal{L}S J$ factors [65]. The solid line represents the observed combined limit. Dashed lines represent limits from individual dSphs.

at high zenith. Draco was not included as the PDF of some of our analysis bins were wider than what is reasonable for a point source analysis. Draco is at a high zenith for HAWC, so the effort required to include it was not justified by the benefits.

We were not able to generate background trials in time of writing this thesis. These are not shown and are an immediate next step for this analysis before publication.

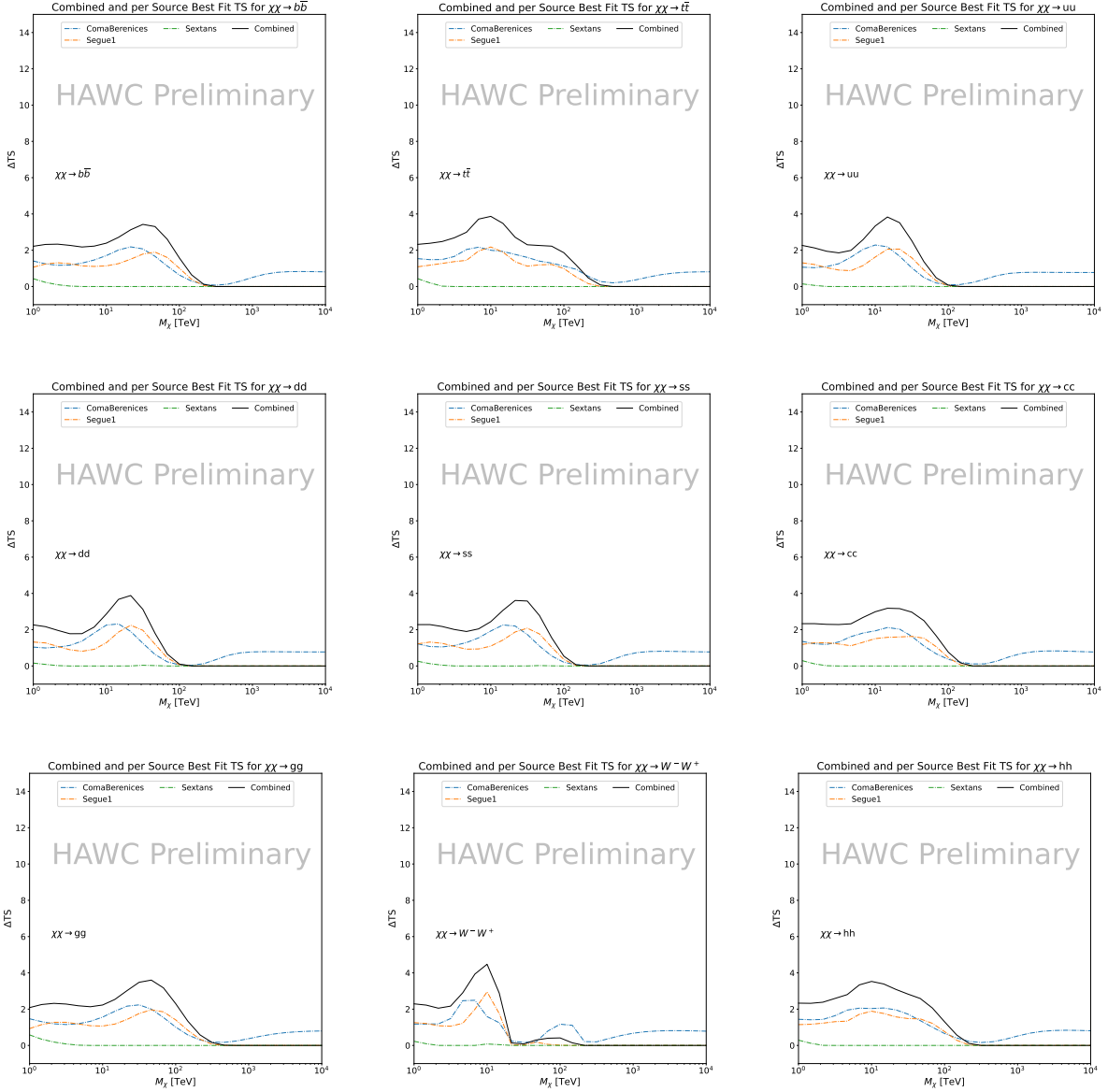


Figure 6.9 HAWC TS values for best fit $\langle\sigma v\rangle$ versus m_χ for SM annihilation channels: $\chi\chi \rightarrow b\bar{b}$, $t\bar{t}$, $u\bar{u}$, $d\bar{d}$, $s\bar{s}$, $c\bar{c}$, gg , W^-W^+ , and hh . Limits use $\mathcal{L}\mathcal{S} J$ factors. The solid black line shows the combined best fit TS values. The colored, dashed lines are the TS values from each dSph.

When comparing these results to Section 5.5, we see an overall decrease to the confidence limit therefore improvement to HAWC's expected sensitivity. This improvement is generally stronger than a doubling of data, or a factor $\sqrt{2}$ decrease. The comparison is somewhat complex and dependant on the dSph and SM annihilation channel. Figure 6.11 shows the comparisons of limits calculated for this analysis and Glory Duck (Section 5.5). Segue 1 and Coma Berenices are low

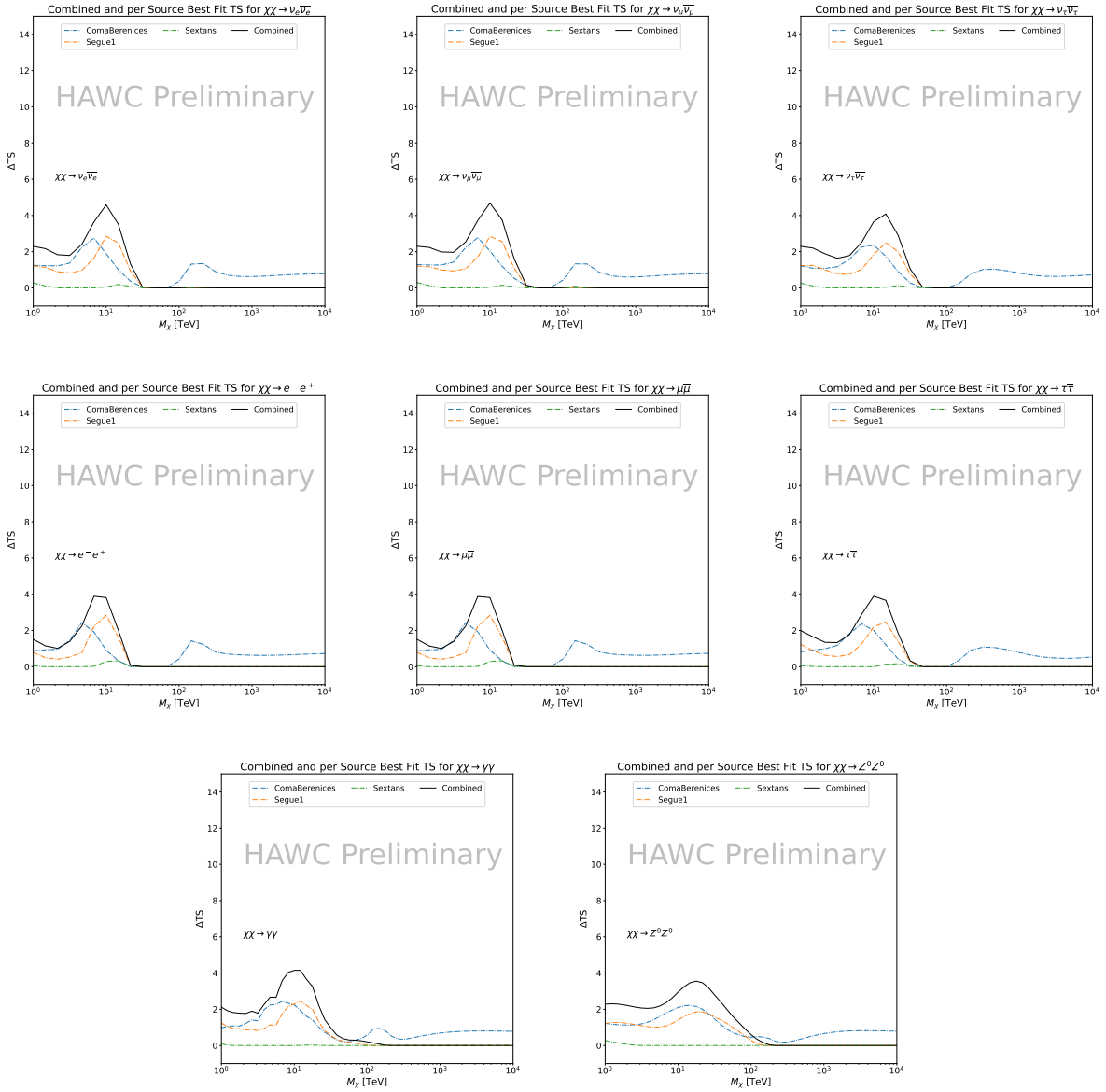


Figure 6.10 HAWC TS values for best fit $\langle\sigma v\rangle$ versus m_χ for SM annihilation channels: $\chi\chi \rightarrow \nu_e \bar{\nu}_e$, $\nu_\mu \bar{\nu}_\mu$, $\nu_\tau \bar{\nu}_\tau$, $e \bar{e}$, $\mu \bar{\mu}$, $\tau \bar{\tau}$, $\gamma\gamma$ and ZZ . Limits use $\mathcal{L}\mathcal{S} J$ factors. The solid black line shows the combined best fit TS values. The colored, dashed lines are the TS values from each dSph.

zenith where improvements to HAWC's analysis come only from energy estimation. Differences between these two are dominately from their differences in J -factor, half-light radii of the dSphs, and the particle physics inputs. Substantial gains in HAWC's analysis methods (pass 5.F) were made at high zenith which is important for sources like Sextans. The HDM particle physics model produces almost identical spectra to the PPPC for $\chi\chi \rightarrow e^- e^+$, so can be used to compare limits

1316 between dSph. Overhead sources see minimal improvement to the limits, while high zenith sources
1317 see an order of magnitude improvement for all DM masses. Softer SM annihilation channels see
1318 broad improvements to the limit compared to harder channels.

1319 **6.7 Systematics**

1320 These are identical to what was performed earlier in Glory Duck, Section 5.7. We are also
1321 sensitive to the choice in spatial template, and this was explored in Section 5.7.2 and Section 5.8.2.

1322 **6.8 Conclusion and Discussion**

1323 In this multithreaded analysis, we have used observations of 3 dSphs from HAWC to perform
1324 a collective DM search for annihilation signals. The data were combined across sources to signifi-
1325 cantly increase the sensitivity of the search. Advanced computational techniques were deployed to
1326 accelerate wall-time spent analyzing by an order of magnitude. We have observed no significant
1327 deviation from the null, no DM, hypothesis, and so present our results in terms of upper limits on
1328 the annihilation cross-section for seventeen potential DM annihilation channels across four decade
1329 of DM mass.

1330 This analysis serves as a proof of concept for multithreaded HAWC analyses with large parameter
1331 spaces. Larger datasets with fast techniques will be essential to tackling the DM problem. The
1332 models we used for this study include annihilation channels with neutrinos in the final state.
1333 Advanced studies could aim to merge our results with those from neutrino observatories with large
1334 data sets.

1335 A full HAWC analysis will include systematic studies of the J -factor distributions. Additionally,
1336 because of the timing reduction, the study can be doubled in size to include DM decay. We have no
1337 yet received the remaining spatial profiles to the $\mathcal{L}\mathcal{S}$ catalog, and limits can be quickly computed
1338 once these are received. Finally, statistical studies with Poission variation of HAWC's background
1339 are essential to a comprehensive understanding of our observed excesses.

Segue1

Coma Berenices

Sextans

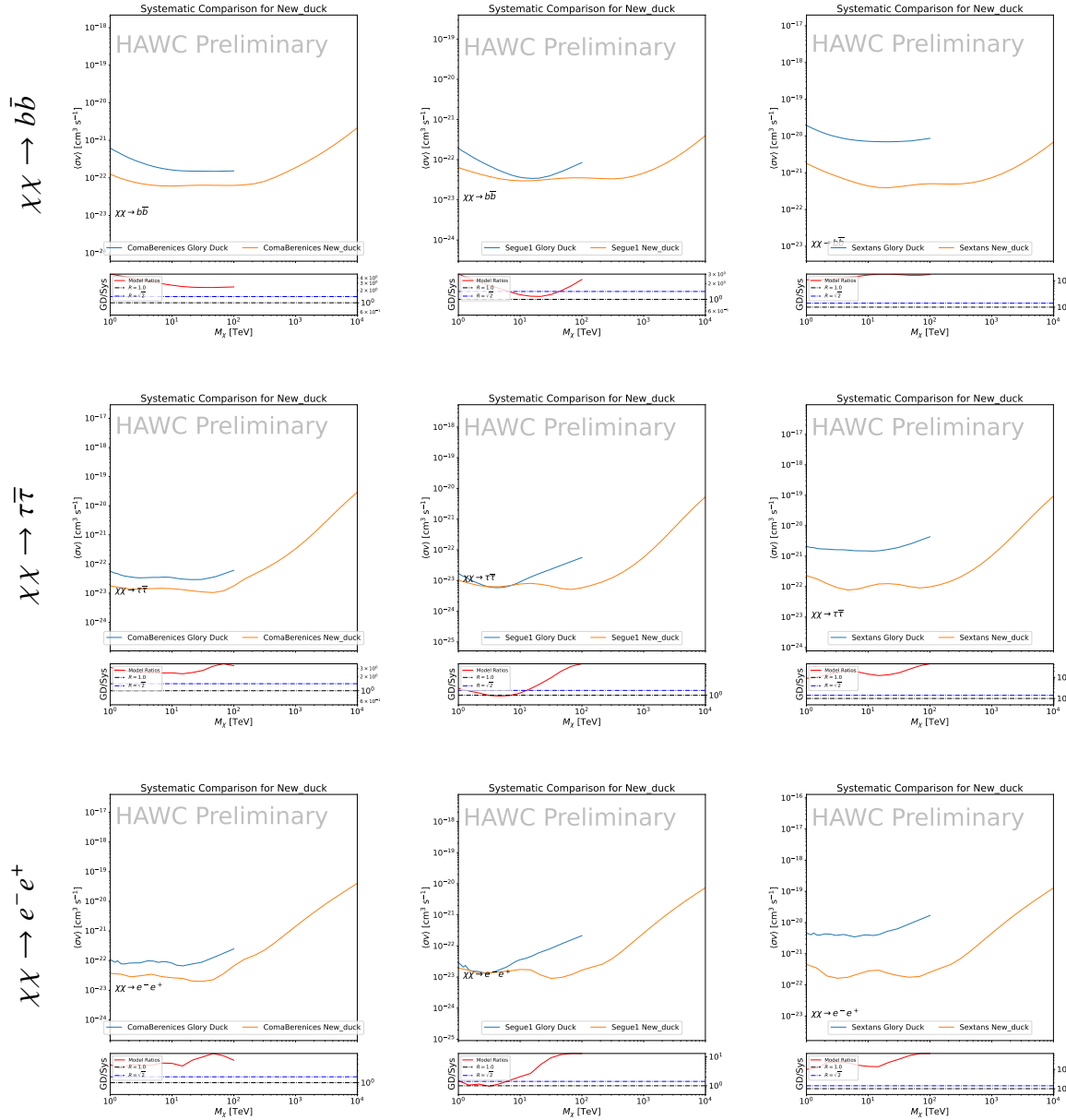


Figure 6.11 Comparison of HAWC limits from this analysis to Glory Duck (Fig. 5.5) for 3 dSphs and 3 SM annihilation channels: $b\bar{b}$, $\tau\bar{\tau}$, and $e\bar{e}$. Each sector shows the 95% confidence limit from Glory Duck (blue line) and this analysis (orange line) in the top plot. The lower plot features the ratio in log scale of Glory Duck to this analysis in a red solid line. Horizontal dashed lines are for ratios of 1.0 (black) and $\sqrt{2}$ (blue). Ratios larger than 1.0 are for limits smaller, or stricter, than Glory Duck. Ratios larger than $\sqrt{2}$ indicates limits are stricter than a simple doubling of the Glory Duck data.

CHAPTER 7

1340 **HEAVY DARK MATTER ANNIHILATION SEARCH WITH ICECUBE'S NORTH SKY**
1341 **TRACK DATA**

1342

CHAPTER 8

NU DUCK

APPENDIX A

MULTI-EXPERIMENT SUPPLEMENTARY FIGURES

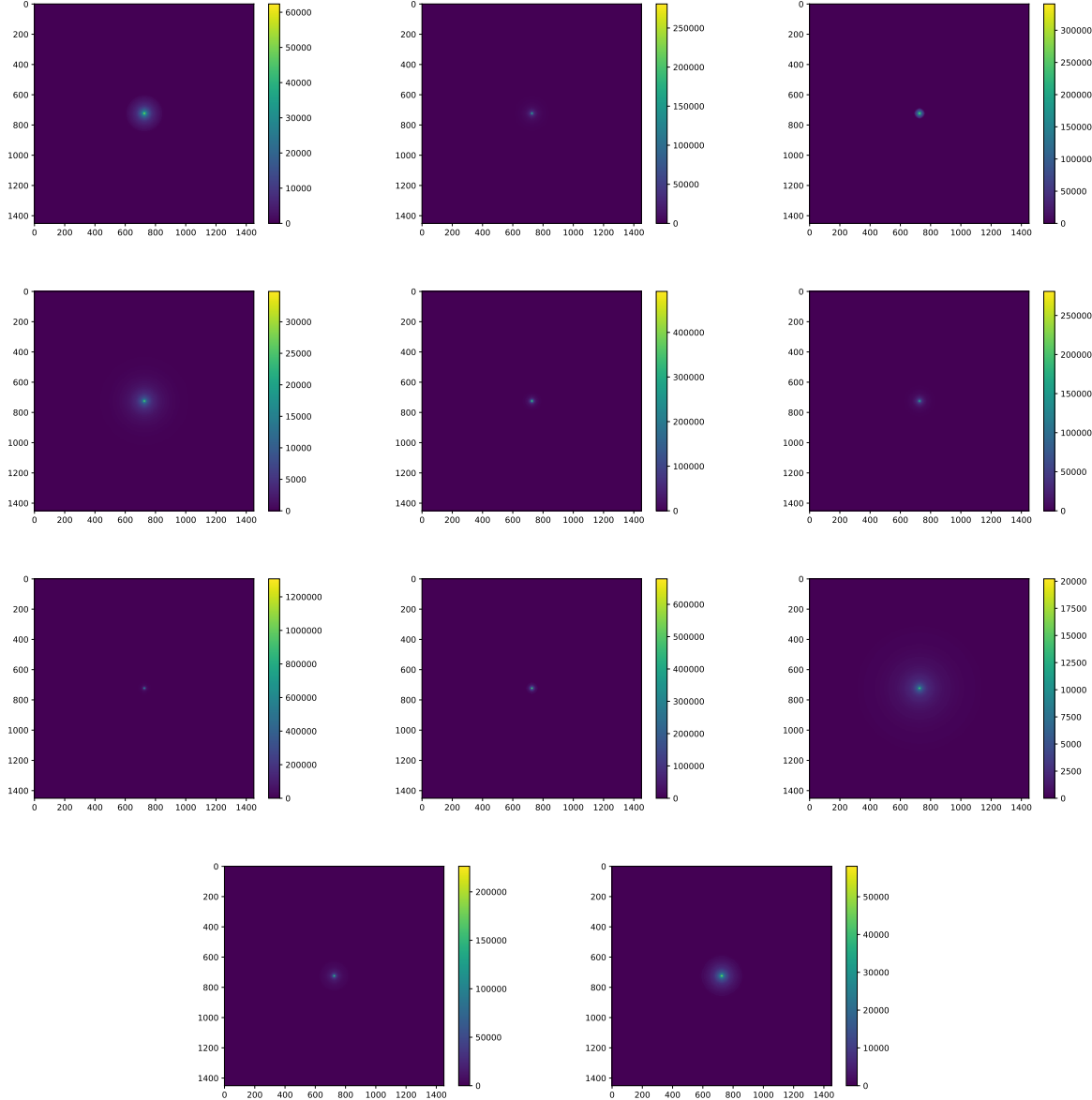


Figure A.1 Sister figure to Figure 5.3. Sources in the first row from left to right: Bootes I, Canes Venatici I, II. In second row: Draco, Hercules, Leo I. In the first row: Leo II, Leo IV, Sextans. In the final row: Ursa Major I, Ursa Major II.

APPENDIX B

1344 MULTITHREADING DARK MATTER ANALYSES SUPPLEMENTARY MATERIAL

1345 B.1 Remaining Spectral Models

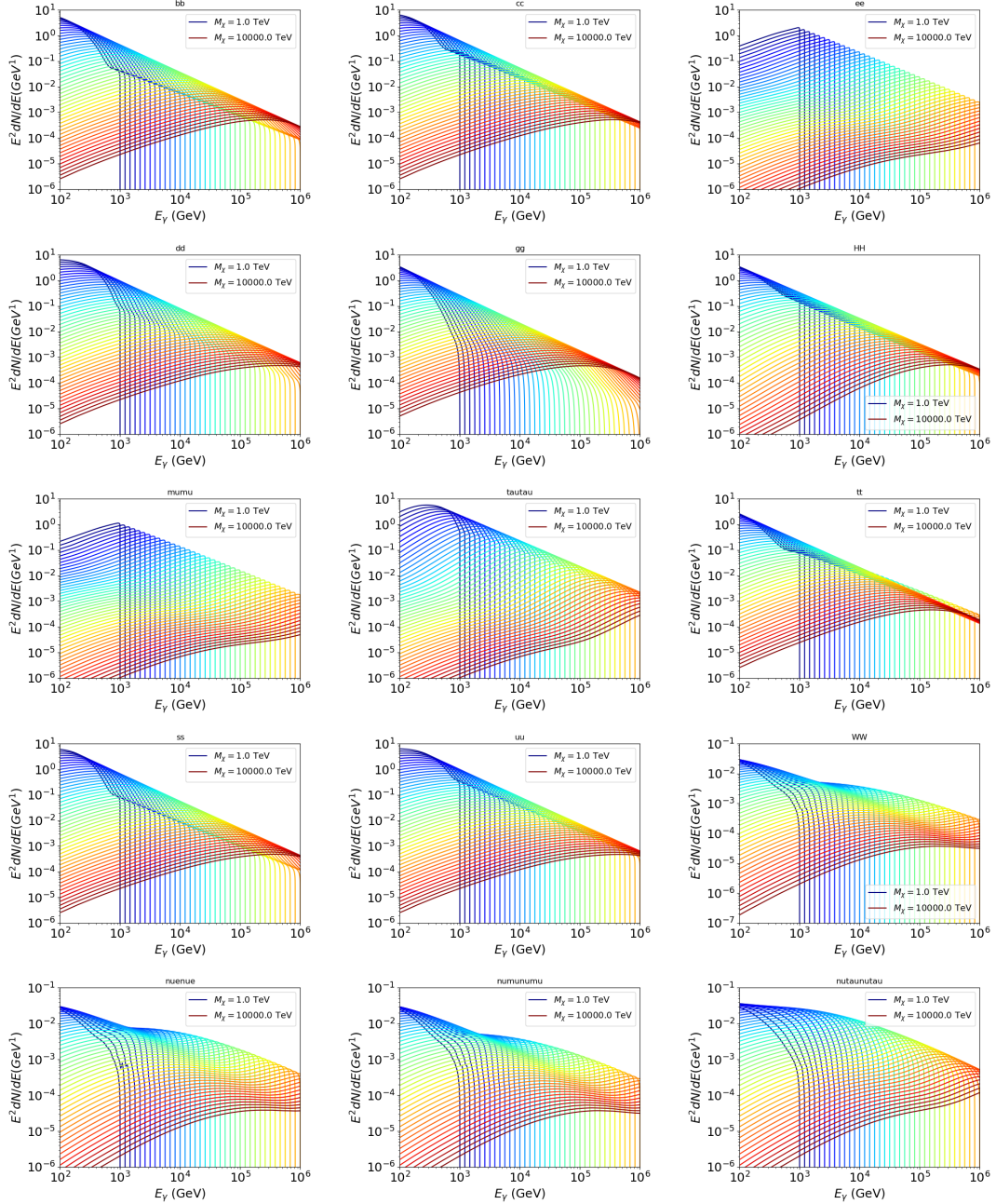


Figure B.1 Sister figure to Figure 6.2 for remaining SM primary annihilation channels studied for this thesis. These did not require any post generation smoothing and so are directly pulled from [64] with a binning scheme most helpful for a HAWC analysis.

1346 B.2 mpu_analysis.py

```
13471 import warnings
13482 with warnings.catch_warnings():
13493     warnings.simplefilter("ignore")
13504 # Python base libraries
13515 import os
13526 import sys
13537 import time
13548 # Import general libraries with namespace
13559 import matplotlib
13560 # Necessary for computing on cluster
13571 matplotlib.use("agg")
13582 import numpy as np
13593 import multiprocessing as mp
13604 # Import HAWC software
13615 sys.path.insert(1, os.path.join(os.environ['HOME'], 'hawc_software', 'threeML-
1362     analysis-scripts', 'fitModel'))
13636 from analysis_modules import *
13647 from threeML import *
13658 from hawc_hal import HAL, HealpixConeROI
13669 from threeML.minimizer.minimization import FitFailed
13670 # Import Dark Matter HAWC Libraries
13681 import analysis_utils as au
13692 import spectra as spec
13703 import sources as srcs
13714
13725 #* READ ONLY PATHS This block will change eventually
13736 MASS_LIST = './plotting/studies/nd/masses.txt'
13747 CHAN_LIST = './plotting/studies/nd/chans.txt'
13758
13769 #* WRITE PATHS, default location is to scratch
13770 OUT_PATH = os.path.join(os.environ["SCRATCH"], os.environ["USER"], 'New_duck')
```

```

13781 print('Our out path is going to be {}'.format(OUT_PATH))
13792
13803 # Define parallel Function. Can also be run serially
13814 def some_mass_fit(sigVs, datalist, shape, dSph, jfactor, mass_chan,
13825                 progress=None, log_file='', queue=None, i_job=0):
13836
13847     if progress is None:
13858         progress = [0]
13869     else: # Create log files for each thread
13870         log_file = log_file.replace('.log', '_ThreadNo_')
13881         log_file = log_file + str(i_job) + ".log"
13892         sys.stdout = open(log_file, "w")
13903
13914     fits = []
13925
13936     try:
13947         for m_c in mass_chan:
13958             print(f'Mass chan tuple: {m_c}')
13969             mass = int(m_c[0])
13970             ch = m_c[1]
13981             # Build path to output files
13992             outPath = os.path.join(OUT_PATH, ch, dSph)
14003             au.ut.ensure_dir(outPath)
14014
14025             if progress[i_job] < 0:
14036                 # If the master gets a Keyboard interrupt, commit suicide.
14047                 break
14058
14069                 ### Start Model Building for DM mass and SM channel #####
14070                 spectrum = spec.DM_models.HDMSpectra()
14081                 spectrum.set_channel(ch)
14092
14103                 myDwarf = ExtendedSource(dSph, spatial_shape=shape,

```

```

141b4                     spectral_shape=spectrum)

14125

14136     spectrum.J = jfactor * u.GeV**2 / u.cm**5
14147     spectrum.sigmav = 1e-24 * u.cm**3 / u.s
14158     spectrum.set_dm_mass(mass * u.GeV)

14169

14170     spectrum.sigmav.bounds = (1e-30, 1e-12)
14181     model = Model(myDwarf)
14192     ##### End model Building #####
14203
14214     jl = JointLikelihood(model, datalist, verbose=False)
14225

14236     try:
14247         result, lhdf = jl.fit(compute_covariance=False)
14258         ts = -2.* (jl.minus_log_like_profile(1e-30) - jl.
1426         _current_minimum)
14279         # Also profile the LLH vs sv
14280         ll = jl.get_contours(spectrum.sigmav, sigVs[0],
14291                         sigVs[-1], len(sigVs),
14302                         progress=False, log=['False'])
14313
14324         sigv_ll = au.ut.calc_95_from_profile(ll[0], ll[2])
14335         # Write results to file
14346         outFileLL = outPath+f"/LL_{dSph}_{ch}_mass{int(mass)}_GD.txt"
14357         np.savetxt(outFileLL, (sigVs, ll[2]),
14368                         delimiter='\t', header='sigV\tLL\n')
14379
14380         with open(outPath+f"/results_{dSph}_{ch}_mass{int(mass)}_GD.
1439         txt", "w") as results_file:
14401             results_file.write("mDM [GeV]\tsigV_95\tsigV_B.F.\n")
14412
14423             results_file.write("%i\t%.5E\t%.5E\t%.5E"%(mass, sigv_ll,
14434                                         ts, result.value[0]))

```

```

14445         # End write to file
14456     except FitFailed: # Don't kill all threads if a fit fails
14467         print("Fit failed. Go back and calculate this spectral model
1447         later")
14488             fits.append((ch, mass, -1, -1))
14499                 with open(log_file+'.fail', 'w') as f_file:
14500                     f_file.write(f'{ch}, {mass}\n')
14511
14522                     progress[i_job] += 1
14533                         matplotlib.pyplot.close() # Prevent leaky memory
14544
14555                     fits.append((ch, mass, result.value[0], ts))
14566                     progress[i_job] += 1
14577                         matplotlib.pyplot.close()
14588             except KeyboardInterrupt:
14599                 progress[i_job] = -1
14600
14611             fits = np.array(fits)
14622             if queue is None:
14633                 return fits
14644             else:
14655                 queue.put((i_job, fits))
14666
14677 def main(args):
14688     masses = np.loadtxt(MASS_LIST, dtype=int)
14699     chans = np.loadtxt(CHAN_LIST, delimiter=',', dtype=str)
14700     mass_chan = au.ut.permute_lists(chans, masses)
14711
14722     print(f"DM masses for this study are: {masses}")
14733     print(f"SM Channels for this study are XX -> {chans}")
14744     print(mass_chan)
14755
14766     # extract information from input argument

```

```

14777 dSph = args.dSph
14788 data_mngr = au.ut.Data_Selector('P5_NN_2D')
14799 dm_profile = srcts.Spatial_DM(args.catalog, dSph, args.sigma, args.decay)
14800
14811 ##### Extract Source Information #####
14822 if dm_profile.get_dec() < -22.0 or dm_profile.get_dec() > 62.0:
14833     raise ValueError("HAWC can't see this source D: Exitting now...")
14844
14855 print(f'{dSph} information')
14866 print(f'jfac: {dm_profile.get_factor()}\tRA: {dm_profile.get_ra()}\tDec: {dm_profile.get_dec()}\n')
14877
14888 shape = SpatialTemplate_2D(fits_file=dm_profile.get_src_fits())
14899 ##### Finish Extract Source Information #####
14910
14921 ##### LOAD HAWC DATA #####
14932 roi = HealpixConeROI(data_radius=2.0, model_radius=8.0,
14943                         ra=dm_profile.get_ra(), dec=dm_profile.get_dec())
14954 bins = choose_bins.analysis_bins(args, dec=dm_profile.get_dec())
14965
14976 hawc = HAL(dSph, data_mngr.get_datmap(), data_mngr.get_detres(), roi)
14987 hawc.set_active_measurements(bin_list=bins)
14998 datalist = DataList(hawc)
15009 ##### FINISH LOAD HAWC DATA #####
15010
15021 # set up SigV sampling. This sample is somewhat standardized
15032 sigVs = np.logspace(-28,-18, 1001, endpoint=True) # NOTE This will change
15043 whith HDM
15053
15064 if args.n_threads == 1:
15075     # No need to start || programming just iterate over the masses
15086     kw_arg = dict(sigVs=sigVs, datalist=datalist, shape=shape, dSph=dSph,
15097                     jfactor=dm_profile.get_factor(), mass_chan=mass_chan,

```

```

15108                 log_file=args.log)
15109             some_mass_fit(**kw_arg)
15120         else:
15131             # I Really want to suppress TQMD output
15142             from tqdm import tqdm
15153             from functools import partialmethod
15164             tqdm.__init__ = partialmethod(tqdm.__init__, disable=True)
15175
15186             x = np.array_split(mass_chan, args.n_threads)
15197             n_jobs = len(x)
15208
15219             print("Thread jobs summary by mass and SM channel")
15220             for xi in x:
15231                 print(f'{xi}')
15242
15253             queue = mp.Queue()
15264             progress = mp.Array('i', np.zeros(n_jobs, dtype=int))
15275
15286             # Define task pool that will be split amongsts threads
15297             kw_args = [dict(sigVs=sigVs, datalist=datalist, shape=shape,
15308                             dSph=dSph, jfactor=dm_profile.get_factor(),
15319                             mass_chan=mass_chan, progress=progress,
15320                             queue=queue, i_job=i, log_file=args.log)
15331                 for i, mass_chan in enumerate(x)]
15342
15353             # Define each process
15364             procs = [mp.Process(target=some_mass_fit, kwargs=kw_args[i]) \
15375                 for i in range(n_jobs)]
15386
15397             ### Start MASTER Thread only code block ###
15408             # Begin running all child threads
15419             for proc in procs: proc.start()
15420

```

```

15431     try:
15442         # In this case, the master does nothing except monitor progress of
1545         the threads
15463         # In an ideal world, the master thread also does some computation.
15474         n_complete = np.sum(progress)
15485         while_count = 0
15496
15507             while n_complete < len(mass_chan):
15518
15529                 if np.any(np.asarray(progress) < 0):
15530                     # This was no threads are stranded when killing the script
15541                     raise KeyboardInterrupt()
15552                 if while_count%1000 == 0:
15563                     print(f"{np.sum(progress)} of {len(mass_chan)} finished")
15574
15585             n_complete = np.sum(progress)
15596             time.sleep(.25)
15607             while_count += 1
15618
15629         except KeyboardInterrupt:
15630             # signal to jobs that it's time to stop
15641                 for i in range(n_jobs):
15652                     progress[i] = -2
15663                     print('\nKeyboardInterrupt: terminating early.')
15674             ### End MASTER Thread only code block ###
15685
15696             fitss = [queue.get() for proc in procs]
15707             print(fitss)
15718             print(f'Thread statuses: {progress[:]}')
15729
15730             # putting results in a file
15741
15752             print("QUACK! All Done!")

```

```

15763
15774
15785 if __name__ == '__main__':
15796     import argparse
15807
15818     p = argparse.ArgumentParser(description="Run a DM annihilation analysis on
1582         a dwarf spheroidal for a specific SM channel for DM masses [1 TeV to 10
1583         PeV]")
15849
15850     # Dwarf spatial modeling arguements
15861     p.add_argument("-ds", "--dSph", type=str,
15872             help="dwarf spheroidal galaxy to be studied", required=
1588     True)
15893     p.add_argument("-cat", "--catalog", type=str, choices=['GS15', 'LS20'],
15904             default='LS20', help="source catalog used")
15915     p.add_argument("-sig", "--sigma", type=int, choices=[-1, 0, 1], default=0,
15926             help="Spatial model uncertainty. 0 corresponds to the
1593 median. +/-1 correspond to the +/-1sigma uncertainty respectively.")
15947
15958     # Arguements for the energy estimators
15969     p.add_argument("-e", "--estimator", type=str,
15970             choices=['P5_NHIT', 'P5_NN_2D'],
15981             default="P5_NN_2D", required=False,
15992             help="The energy estimator choice. Options are: P5_NHIT,
1600 P5_NN_2D. GP not supported (yet).")
16013     p.add_argument("--use-bins", default=None, nargs="*",
16024             help="Bins to use for the analysis", dest="use_bins")
16035     p.add_argument('--select_bins_by_energy', default=None, nargs="*",
16046             help="Does nothing. May fill in later once better
1605 understood")
16067     p.add_argument('--select_bins_by_fhit', default=None, nargs="*",
16078             help="Also does nothing see above")
16089     p.add_argument( '-ex', "--exclude", default=None, nargs="*",

```

```

16090         help="Exclude Bins", dest="exclude")

16101

16102     # Computing and logging arguements.

16103     p.add_argument('-nt', '--n_threads', type=int, default=1,
16104                     help='Maximum number of threads spawned by script. Default
16105                     is 4')

16106     p.add_argument('-log', '--log', type=str, required=True,
16107                     help='Name for log files. Especially needed for threads')

16108     p.add_argument('--decay', action="store_true",
16109                     help='Set spectral DM hypothesis to decay')

16110

16111     args = p.parse_args()

16112     print(args.decay)

16113     if args.exclude is None: # default exclude bins 0 and 1
16114         args.exclude = ['B0C0Ea', 'B0C0Eb', 'B0C0Ec', 'B0C0Ed', 'B0C0Ee']

16115

16116     if args.decay: OUT_PATH += '_dec'
16117     else: OUT_PATH += '_ann'

16118

16119     OUT_PATH = OUT_PATH + '_' + args.catalog
16120     if args.sigma != 0: OUT_PATH += f'_{args.sigma}sig'

16121

16122     main(args)

```

1633 B.3 Comparison with Glory Duck

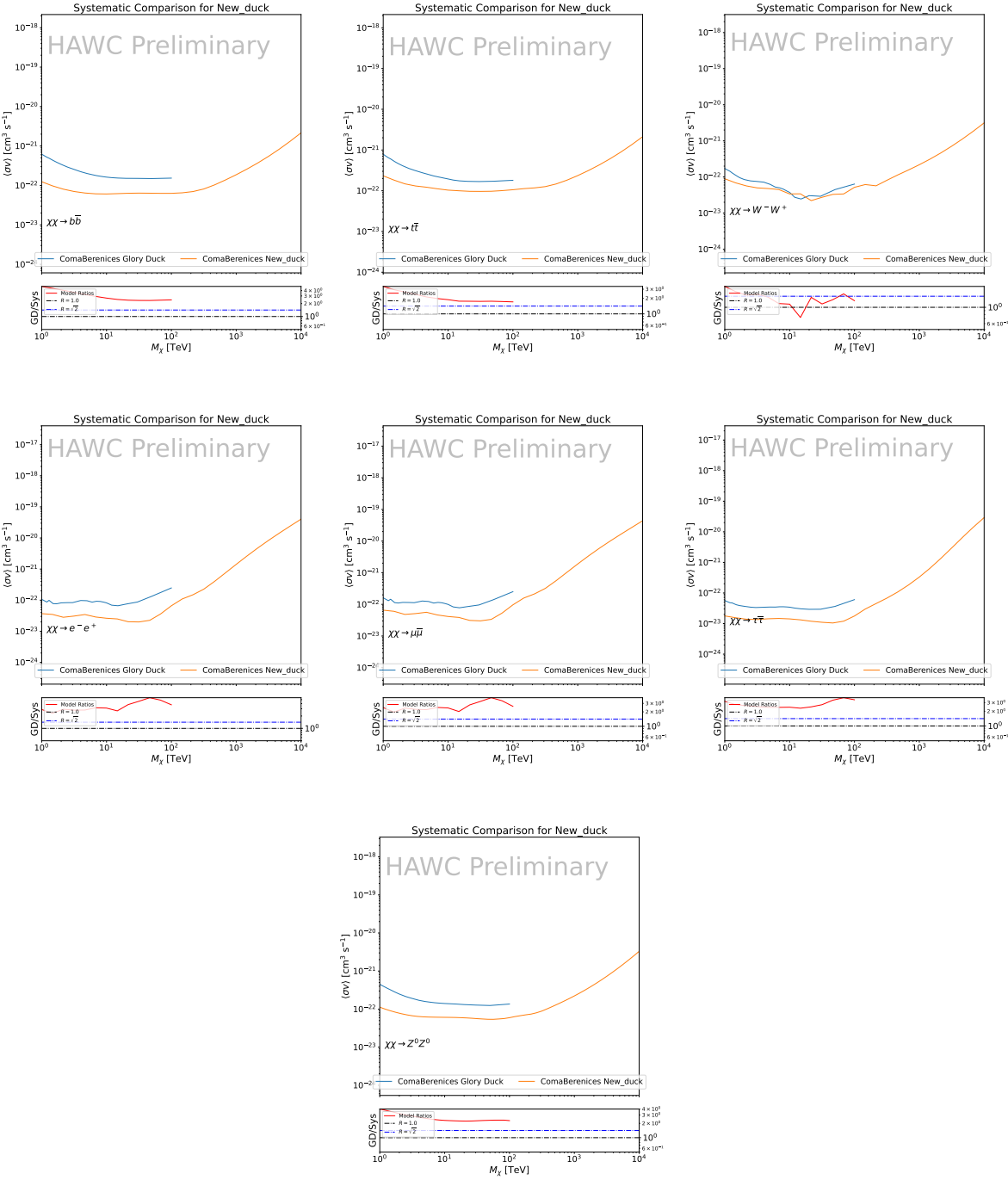


Figure B.2 TODO: fill this out

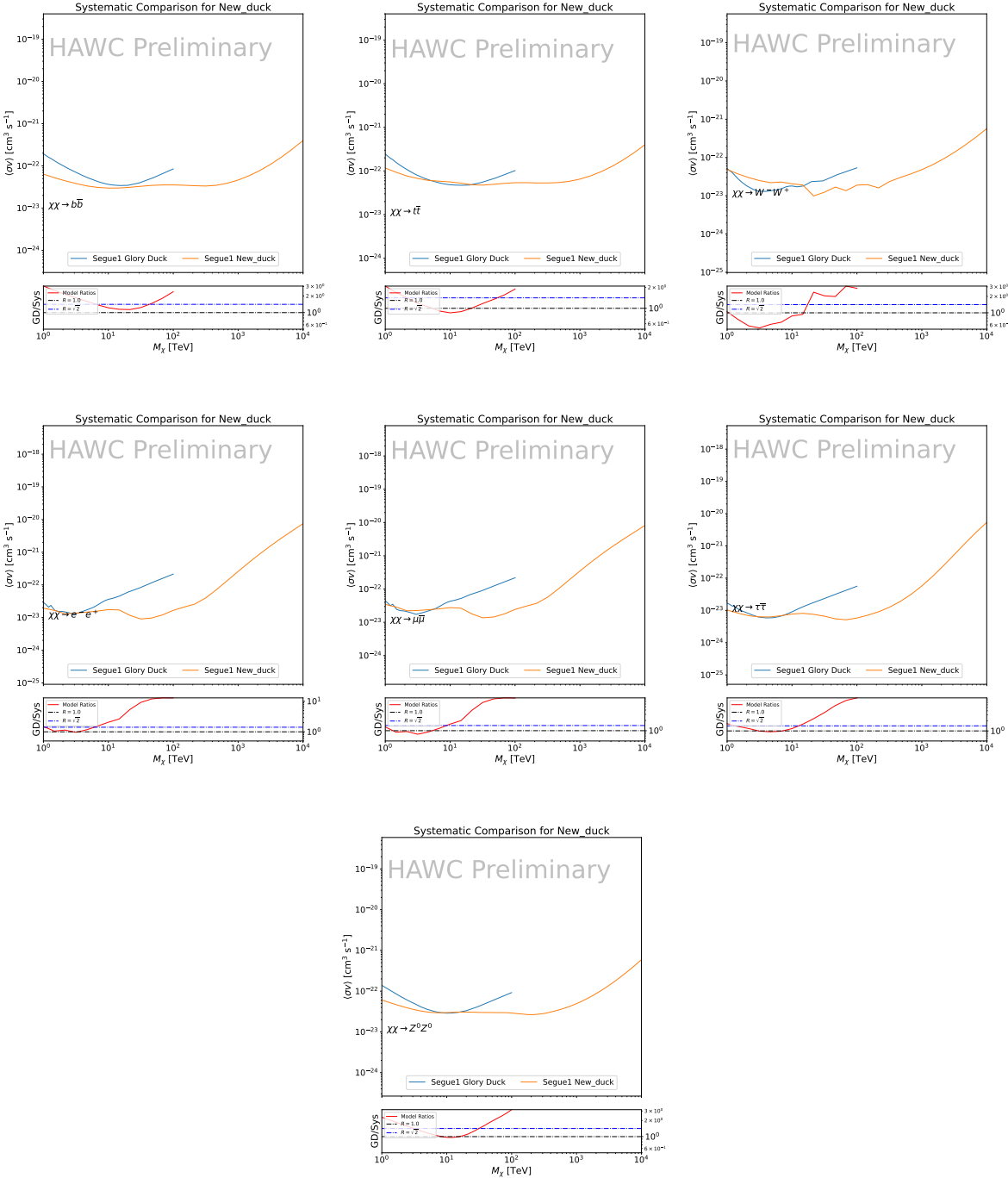


Figure B.3 TODO: fill this out

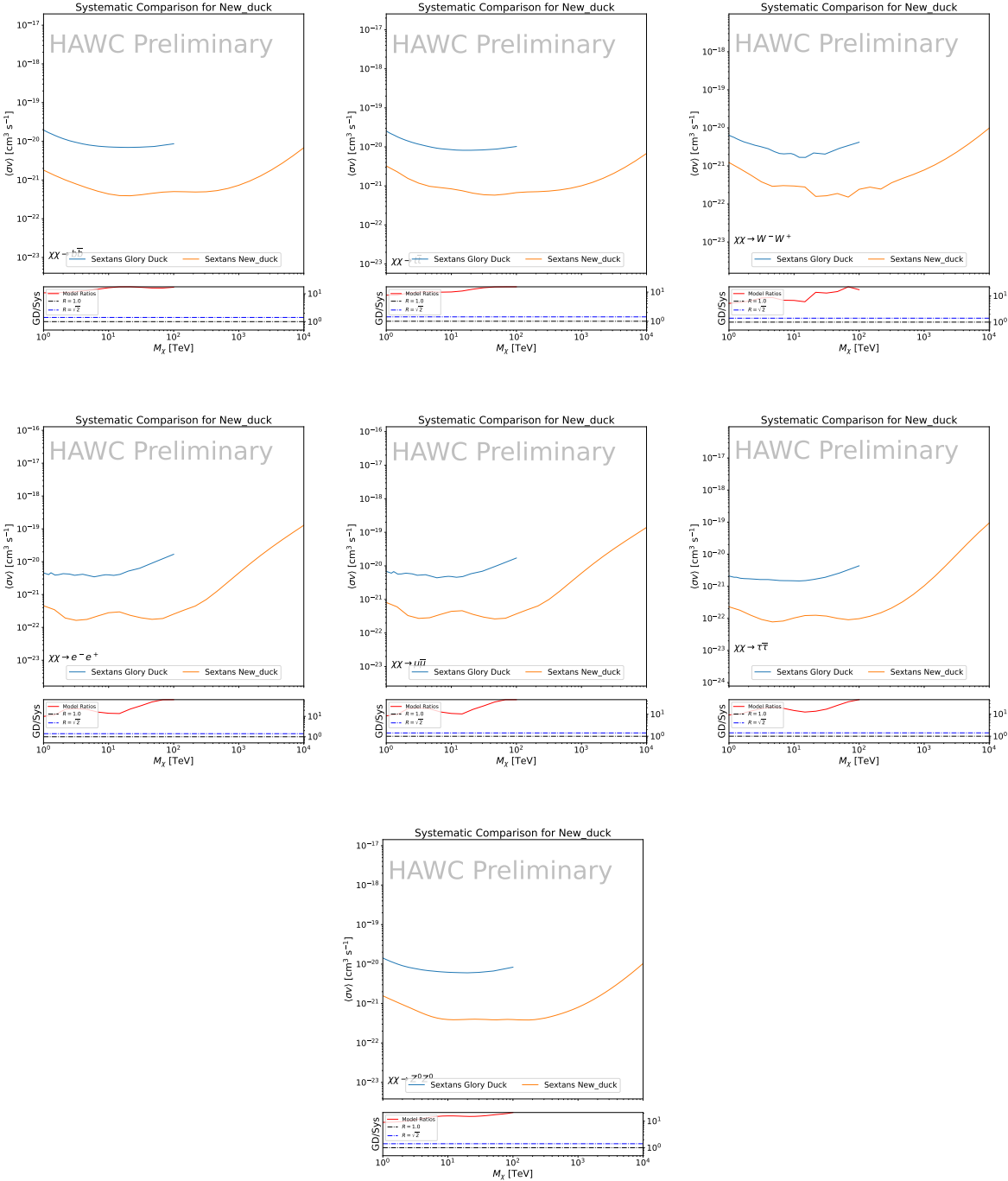


Figure B.4 TODO: fill this out

BIBLIOGRAPHY

- 1635 [1] Anne M. Green. “Dark matter in astrophysics/cosmology”. In: *SciPost Phys. Lect.*
 1636 *Notes* (2022), p. 37. doi: [10.21468/SciPostPhysLectNotes.37](https://doi.org/10.21468/SciPostPhysLectNotes.37). URL: <https://scipost.org/10.21468/SciPostPhysLectNotes.37>.
- 1638 [2] Bing-Lin Young. “A survey of dark matter and related topics in cosmology”. In: *Frontiers*
 1639 *of Physics* 12 (Oct. 2016). doi: <https://doi.org/10.1007/s11467-016-0583-4>.
 1640 URL: <https://doi.org/10.1007/s11467-016-0583-4>.
- 1641 [3] Gianfranco Bertone, Dan Hooper, and Joseph Silk. “Particle dark matter: evidence,
 1642 candidates and constraints”. In: *Physics Reports* 405.5 (2005), pp. 279–390. ISSN:
 1643 0370-1573. doi: <https://doi.org/10.1016/j.physrep.2004.08.031>. URL:
 1644 <https://www.sciencedirect.com/science/article/pii/S0370157304003515>.
- 1645 [4] Gianfranco Bertone and Dan Hooper. “History of dark matter”. In: *Rev. Mod. Phys.*
 1646 90 (4 Aug. 2018), p. 045002. doi: [10.1103/RevModPhys.90.045002](https://doi.org/10.1103/RevModPhys.90.045002). URL: <https://link.aps.org/doi/10.1103/RevModPhys.90.045002>.
- 1648 [5] Fritz Zwicky. “The Redshift of Extragalactic Nebulae”. In: *Helvetica Physica Acta* 6.
 1649 (1933), pp. 110–127. doi: [10.5169/seals-110267](https://doi.org/10.5169/seals-110267).
- 1650 [6] Vera C. Rubin and Jr. Ford W. Kent. “Rotation of the Andromeda Nebula from a
 1651 Spectroscopic Survey of Emission Regions”. In: *ApJ* 159 (Feb. 1970), p. 379. doi:
 1652 [10.1086/150317](https://doi.org/10.1086/150317).
- 1653 [7] K. G. Begeman, A. H. Broeils, and R. H. Sanders. “Extended rotation curves of spiral galax-
 1654 ies: dark haloes and modified dynamics”. In: *Monthly Notices of the Royal Astronomical So-*
 1655 *ciety* 249.3 (Apr. 1991), pp. 523–537. ISSN: 0035-8711. doi: [10.1093/mnras/249.3.523](https://doi.org/10.1093/mnras/249.3.523).
 1656 eprint: <https://academic.oup.com/mnras/article-pdf/249/3/523/18160929/mnras249-0523.pdf>. URL: <https://doi.org/10.1093/mnras/249.3.523>.
- 1658 [8] *Different types of gravitational lenses*. website. Feb. 2004. URL: <https://esahubble.org/images/heic0404b/>.
- 1660 [9] Douglas Clowe et al. “A Direct Empirical Proof of the Existence of Dark Matter”. In: *apjl*
 1661 648.2 (Sept. 2006), pp. L109–L113. doi: [10.1086/508162](https://doi.org/10.1086/508162). arXiv: [astro-ph/0608407](https://arxiv.org/abs/astro-ph/0608407)
 1662 [[astro-ph](https://arxiv.org/abs/astro-ph/0608407)].
- 1663 [10] Planck Collaboration and N. et. al. Aghanim. “Planck 2018 results I. Overview and the
 1664 cosmological legacy of Planck”. In: *A&A* 641 (2020). doi: [10.1051/0004-6361/201833880](https://doi.org/10.1051/0004-6361/201833880). URL: <https://doi.org/10.1051/0004-6361/201833880>.
- 1666 [11] Wayne Hu. *Matter Density Animation*. web. 2024. URL: <http://background.uchicago.edu/~whu/animbut/anim2.html>.

- 1668 [12] Wenlong Yuan et al. “A First Look at Cepheids in a Type Ia Supernova Host with JWST”. in:
1669 *The Astrophysical Journal Letters* 940.1 (Nov. 2022). doi: [10.3847/2041-8213/ac9b27](https://doi.org/10.3847/2041-8213/ac9b27).
1670 URL: <https://dx.doi.org/10.3847/2041-8213/ac9b27>.
- 1671 [13] Wendy L. Freedman. “Measurements of the Hubble Constant: Tensions in Perspective”. In:
1672 *The Astrophysical Journal* 919.1 (Sept. 2021), p. 16. doi: [10.3847/1538-4357/ac0e95](https://doi.org/10.3847/1538-4357/ac0e95).
1673 URL: <https://dx.doi.org/10.3847/1538-4357/ac0e95>.
- 1674 [14] Jodi Cooley. “Dark Matter direct detection of classical WIMPs”. In: *SciPost Phys. Lect.
1675 Notes* (2022), p. 55. doi: [10.21468/SciPostPhysLectNotes.55](https://doi.org/10.21468/SciPostPhysLectNotes.55). URL: <https://scipost.org/10.21468/SciPostPhysLectNotes.55>.
- 1677 [15] “Search for new phenomena in events with an energetic jet and missing transverse momentum
1678 in pp collisions at $\sqrt{s} = 13$ TeV with the ATLAS detector”. In: *Phys. Rev. D* 103
1679 (11 July 2021), p. 112006. doi: [10.1103/PhysRevD.103.112006](https://doi.org/10.1103/PhysRevD.103.112006). URL: <https://link.aps.org/doi/10.1103/PhysRevD.103.112006>.
- 1681 [16] *Jetting into the dark side: a precision search for dark matter*. website. July 2020. URL:
1682 <https://atlas.cern/updates/briefing/precision-search-dark-matter>.
- 1683 [17] Celine Armand et. al. “Combined dark matter searches towards dwarf spheroidal galaxies
1684 with Fermi-LAT, HAWC, H.E.S.S., MAGIC, and VERITAS”. in: *Proceedings of Science*.
1685 Vol. 395. Mar. 2022. doi: <https://doi.org/10.22323/1.395.0528>.
- 1686 [18] Tracy R. Slatyer. “Les Houches Lectures on Indirect Detection of Dark Matter”. In: *SciPost
1687 Phys. Lect. Notes* (2022), p. 53. doi: [10.21468/SciPostPhysLectNotes.53](https://doi.org/10.21468/SciPostPhysLectNotes.53). URL:
1688 <https://scipost.org/10.21468/SciPostPhysLectNotes.53>.
- 1689 [19] Christian W Bauer, Nicholas L. Rodd, and Bryan R. Webber. “Dark matter spectra from
1690 the electroweak to the Planck scale”. In: *Journal of High Energy Physics* 2021.1029-8479
1691 (June 2021). doi: [https://doi.org/10.1007/JHEP06\(2021\)121](https://doi.org/10.1007/JHEP06(2021)121).
- 1692 [20] Riccardo Catena and Piero Ullio. “A novel determination of the local dark matter density”.
1693 In: *Journal of Cosmology and Astroparticle Physics* 2010.08 (Aug. 2010), p. 004. doi:
1694 [10.1088/1475-7516/2010/08/004](https://doi.org/10.1088/1475-7516/2010/08/004). URL: <https://dx.doi.org/10.1088/1475-7516/2010/08/004>.
- 1696 [21] B. P. Abbott et al. “Observation of Gravitational Waves from a Binary Black Hole Merger”.
1697 In: *Phys. Rev. Lett.* 116 (6 Feb. 2016), p. 061102. doi: [10.1103/PhysRevLett.116.061102](https://doi.org/10.1103/PhysRevLett.116.061102). URL: <https://link.aps.org/doi/10.1103/PhysRevLett.116.061102>.
- 1699 [22] R. Abbasi et. al. “Observation of high-energy neutrinos from the Galactic plane”. In: *Science*
1700 380.6652 (June 2023), pp. 1338–1343.
- 1701 [23] NASA Goddard Space Flight Center. *Fermi’s 12-year view of the gamma-ray sky*. website.

- 1702 2022. URL: <https://svs.gsfc.nasa.gov/14090>.
- 1703 [24] Marco Cirelli et al. “PPPC 4 DM ID: a poor particle physicist cookbook for dark matter
1704 indirect detection”. In: *Journal of Cosmology and Astroparticle Physics* 2011.03 (Mar.
1705 2011), p. 051. doi: [10.1088/1475-7516/2011/03/051](https://doi.org/10.1088/1475-7516/2011/03/051). URL: <https://dx.doi.org/10.1088/1475-7516/2011/03/051>.
- 1707 [25] Javier Rico. “Gamma-Ray Dark Matter Searches in Milky Way Satellites—A Comparative
1708 Review of Data Analysis Methods and Current Results”. In: *Galaxies* 8.1 (Mar. 2020), p. 25.
1709 doi: [10.3390/galaxies8010025](https://doi.org/10.3390/galaxies8010025). arXiv: [2003.13482](https://arxiv.org/abs/2003.13482) [astro-ph.HE].
- 1710 [26] W. B. Atwood et al. “The Large Area Telescope on the Fermi Gamma-Ray Space Telescope
1711 Mission”. In: *apj* 697.2 (June 2009), pp. 1071–1102. doi: [10.1088/0004-637X/697/2/1071](https://doi.org/10.1088/0004-637X/697/2/1071). arXiv: [0902.1089](https://arxiv.org/abs/0902.1089) [astro-ph.IM].
- 1713 [27] M. Ackermann et al. “Searching for Dark Matter Annihilation from Milky Way Dwarf
1714 Spheroidal Galaxies with Six Years of Fermi Large Area Telescope Data”. In: *prl* 115.23,
1715 231301 (Dec. 2015), p. 231301. doi: [10.1103/PhysRevLett.115.231301](https://doi.org/10.1103/PhysRevLett.115.231301). arXiv:
1716 [1503.02641](https://arxiv.org/abs/1503.02641) [astro-ph.HE].
- 1717 [28] Mattia Di Mauro, Martin Stref, and Francesca Calore. “Investigating the effect of Milky
1718 Way dwarf spheroidal galaxies extension on dark matter searches with Fermi-LAT data”.
1719 In: *Phys. Rev. D* 106 (12 Dec. 2022), p. 123032. doi: [10.1103/PhysRevD.106.123032](https://doi.org/10.1103/PhysRevD.106.123032).
1720 URL: <https://link.aps.org/doi/10.1103/PhysRevD.106.123032>.
- 1721 [29] F. et al. Aharonian. “Observations of the Crab Nebula with H.E.S.S.”. In: *Astron. Astrophys.*
1722 457 (2006), pp. 899–915. doi: [10.1051/0004-6361:20065351](https://doi.org/10.1051/0004-6361:20065351). arXiv: [astro-ph/0607333](https://arxiv.org/abs/astro-ph/0607333).
- 1724 [30] J. Albert et al. “VHE γ -Ray Observation of the Crab Nebula and its Pulsar with the MAGIC
1725 Telescope”. In: *The Astrophysical Journal* 674.2 (Feb. 2008), p. 1037. doi: [10.1086/525270](https://doi.org/10.1086/525270). URL: <https://dx.doi.org/10.1086/525270>.
- 1727 [31] N. Park. “Performance of the VERITAS experiment”. In: *Proceedings, 34th International
1728 Cosmic Ray Conference (ICRC2015): The Hague, The Netherlands, July, 30th July - 6th
1729 August*. Vol. 34. 2015, p. 771. arXiv: [1508.07070](https://arxiv.org/abs/1508.07070) [astro-ph.IM].
- 1730 [32] A. Abramowski et al. “H.E.S.S. constraints on Dark Matter annihilations towards the Sculptor
1731 and Carina Dwarf Galaxies”. In: *Astropart. Phys.* 34 (2011), pp. 608–616. doi: [10.1016/j.astropartphys.2010.12.006](https://doi.org/10.1016/j.astropartphys.2010.12.006). arXiv: [1012.5602](https://arxiv.org/abs/1012.5602) [astro-ph.HE].
- 1733 [33] A. Abramowski et al. “Search for dark matter annihilation signatures in H.E.S.S. observations
1734 of Dwarf Spheroidal Galaxies”. In: *Phys. Rev. D* 90 (2014), p. 112012. doi: [10.1103/PhysRevD.90.112012](https://doi.org/10.1103/PhysRevD.90.112012). arXiv: [1410.2589](https://arxiv.org/abs/1410.2589) [astro-ph.HE].

- 1736 [34] H. Abdalla et al. “Searches for gamma-ray lines and ‘pure WIMP’ spectra from Dark
1737 Matter annihilations in dwarf galaxies with H.E.S.S”. in: *JCAP* 11 (2018), p. 037. doi:
1738 [10.1088/1475-7516/2018/11/037](https://doi.org/10.1088/1475-7516/2018/11/037). arXiv: [1810.00995 \[astro-ph.HE\]](https://arxiv.org/abs/1810.00995).
- 1739 [35] J. Aleksić et al. “Optimized dark matter searches in deep observations of Segue 1 with
1740 MAGIC”. in: *JCAP* 1402 (2014), p. 008. doi: [10.1088/1475-7516/2014/02/008](https://doi.org/10.1088/1475-7516/2014/02/008).
1741 arXiv: [1312.1535 \[hep-ph\]](https://arxiv.org/abs/1312.1535).
- 1742 [36] V.A. Acciari et al. “Combined searches for dark matter in dwarf spheroidal galaxies observed
1743 with the MAGIC telescopes, including new data from Coma Berenices and Draco”. In: *Physics of the Dark Universe* (2021), p. 100912. issn: 2212-6864. doi: <https://doi.org/10.1016/j.dark.2021.100912>. URL: <https://www.sciencedirect.com/science/article/pii/S2212686421001370>.
- 1747 [37] M. L. Ahnen et al. “Indirect dark matter searches in the dwarf satellite galaxy Ursa Major II
1748 with the MAGIC Telescopes”. In: *JCAP* 1803.03 (2018), p. 009. doi: [10.1088/1475-7516/2018/03/009](https://doi.org/10.1088/1475-7516/2018/03/009). arXiv: [1712.03095 \[astro-ph.HE\]](https://arxiv.org/abs/1712.03095).
- 1750 [38] S. et al. Archambault. “Dark matter constraints from a joint analysis of dwarf Spheroidal
1751 galaxy observations with VERITAS”. in: *prd* 95.8 (Apr. 2017). doi: [10.1103/PhysRevD.95.082001](https://doi.org/10.1103/PhysRevD.95.082001). arXiv: [1703.04937 \[astro-ph.HE\]](https://arxiv.org/abs/1703.04937).
- 1753 [39] Louise Oakes et al. “Combined Dark Matter searches towards dwarf spheroidal galaxies with
1754 Fermi-LAT, HAWC, HESS, MAGIC and VERITAS”. in: *Proceedings of Science*. 2019.
- 1755 [40] Celine Armand et al. on behalf of the Fermi-LAT, HAWC, HESS, MAGIC, VERITAS.
1756 “Combined Dark Matter searches towards dwarf spheroidal galaxies with Fermi-LAT,
1757 HAWC, HESS, MAGIC and VERITAS”. in: *Proceedings of Science*. 2021.
- 1758 [41] Daniel Kerszberg et al. on behalf of the Fermi-LAT, HAWC, HESS, MAGIC, and VER-
1759 TIAS collaborations. “Search for dark matter annihilation with a combined analysis of
1760 dwarf spheroidal galaxies from Fermi-LAT, HAWC, H.E.S.S., MAGIC and VERITAS”. in:
1761 *Proceedings of Science*. 2023.
- 1762 [42] A. U. Abeysekara et al. “Observation of the Crab Nebula with the HAWC Gamma-Ray
1763 Observatory”. In: *The Astrophysical Journal* 843.1 (June 2017), p. 39. doi: [10.3847/1538-4357/aa7555](https://doi.org/10.3847/1538-4357/aa7555). URL: <https://doi.org/10.3847/1538-4357/aa7555>.
- 1765 [43] Giacomo Vianello et al. *The Multi-Mission Maximum Likelihood framework (3ML)*. 2015.
1766 arXiv: [1507.08343 \[astro-ph.HE\]](https://arxiv.org/abs/1507.08343).
- 1767 [44] Marco Cirelli et al. “PPPC 4 DM ID: a poor particle physicist cookbook for dark matter
1768 indirect detection”. In: *Journal of Cosmology and Astroparticle Physics* 2011.03 (Mar.
1769 2011). issn: 1475-7516. doi: [10.1088/1475-7516/2011/03/051](https://doi.org/10.1088/1475-7516/2011/03/051). URL: <http://dx.doi.org/10.1088/1475-7516/2011/03/051>.

- 1771 [45] Alex Geringer-Sameth, Savvas M. Koushiappas, and Matthew Walker. “DWARF GALAXY
1772 ANNIHILATION AND DECAY EMISSION PROFILES FOR DARK MATTER EXPERI-
1773 MENTS”. in: *The Astrophysical Journal* 801.2 (Mar. 2015), p. 74. ISSN: 1538-4357. doi:
1774 [10.1088/0004-637X/801/2/74](https://doi.org/10.1088/0004-637X/801/2/74). URL: <http://dx.doi.org/10.1088/0004-637X/801/2/74>.
- 1776 [46] A. Albert et al. “Dark Matter Limits from Dwarf Spheroidal Galaxies with the HAWC
1777 Gamma-Ray Observatory”. In: *The Astrophysical Journal* 853.2 (Feb. 2018), p. 154. ISSN:
1778 1538-4357. doi: [10.3847/1538-4357/aaa6d8](https://doi.org/10.3847/1538-4357/aaa6d8). URL: <http://dx.doi.org/10.3847/1538-4357/aaa6d8>.
- 1780 [47] V. Bonnivard et al. “Spherical Jeans analysis for dark matter indirect detection in dwarf
1781 spheroidal galaxies - Impact of physical parameters and triaxiality”. In: *Mon. Not. Roy.
1782 Astron. Soc.* 446 (2015), pp. 3002–3021. doi: [10.1093/mnras/stu2296](https://doi.org/10.1093/mnras/stu2296). arXiv:
1783 [1407.7822 \[astro-ph.HE\]](https://arxiv.org/abs/1407.7822).
- 1784 [48] M. Ackermann et al. “Searching for Dark Matter Annihilation from Milky Way Dwarf
1785 Spheroidal Galaxies with Six Years of Fermi Large Area Telescope Data”. In: *prl* 115.23,
1786 231301 (Dec. 2015), p. 231301. doi: [10.1103/PhysRevLett.115.231301](https://doi.org/10.1103/PhysRevLett.115.231301). arXiv:
1787 [1503.02641 \[astro-ph.HE\]](https://arxiv.org/abs/1503.02641).
- 1788 [49] M. L. Ahnen et al. “Limits to Dark Matter Annihilation Cross-Section from a Combined
1789 Analysis of MAGIC and Fermi-LAT Observations of Dwarf Satellite Galaxies”. In: *JCAP*
1790 1602.02 (2016), p. 039. doi: [10.1088/1475-7516/2016/02/039](https://doi.org/10.1088/1475-7516/2016/02/039). arXiv: [1601.06590](https://arxiv.org/abs/1601.06590)
1791 [astro-ph.HE].
- 1792 [50] Javier Rico et al. *gLike: numerical maximization of heterogeneous joint
1793 likelihood functions of a common free parameter plus nuisance parameters*.
1794 <https://doi.org/10.5281/zenodo.4601451>. Version v0.09.03. Mar. 2021. doi: [10.5281/zenodo.4601451](https://doi.org/10.5281/zenodo.4601451). URL: <https://doi.org/10.5281/zenodo.4601451>.
- 1796 [51] Tjark Miener and Daniel Nieto. *LklCom: Combining likelihoods from different experiments*.
1797 <https://doi.org/10.5281/zenodo.4597500>. Version v0.5.3. Mar. 2021. doi: [10.5281/zenodo.4597500](https://doi.org/10.5281/zenodo.4597500). URL: <https://doi.org/10.5281/zenodo.4597500>.
- 1799 [52] T. Miener et al. “Open-source Analysis Tools for Multi-instrument Dark Matter Searches”.
1800 In: *arXiv e-prints*, arXiv:2112.01818 (Dec. 2021), arXiv:2112.01818. arXiv: [2112.01818](https://arxiv.org/abs/2112.01818)
1801 [astro-ph.IM].
- 1802 [53] Alex Geringer-Sameth and Matthew Koushiappas Savvas M. and Walker. “Dwarf galaxy
1803 annihilation and decay emission profiles for dark matter experiments”. In: *Astrophys.
1804 J.* 801.2 (2015), p. 74. doi: [10.1088/0004-637X/801/2/74](https://doi.org/10.1088/0004-637X/801/2/74). arXiv: [1408.0002](https://arxiv.org/abs/1408.0002)
1805 [astro-ph.CO].
- 1806 [54] Gianfranco Bertone, Dan Hooper, and Joseph Silk. “Particle dark matter: evidence, can-

- 1807 didates and constraints”. In: *Physics Reports* 405.5-6 (Jan. 2005), pp. 279–390. ISSN:
1808 0370-1573. doi: [10.1016/j.physrep.2004.08.031](https://doi.org/10.1016/j.physrep.2004.08.031). URL: <http://dx.doi.org/10.1016/j.physrep.2004.08.031>.
- 1810 [55] V. Bonnivard et al. “Dark matter annihilation and decay in dwarf spheroidal galaxies: The
1811 classical and ultrafaint dSphs”. In: *Mon. Not. Roy. Astron. Soc.* 453.1 (2015), pp. 849–867.
1812 doi: [10.1093/mnras/stv1601](https://doi.org/10.1093/mnras/stv1601). arXiv: [1504.02048 \[astro-ph.HE\]](https://arxiv.org/abs/1504.02048).
- 1813 [56] A. et al. Albert. “Searching for Dark Matter Annihilation in Recently Discovered Milky Way
1814 Satellites with Fermi-LAT”. in: *Astrophys. J.* 834.2 (2017), p. 110. doi: [10.3847/1538-4357/834/2/110](https://doi.org/10.3847/1538-4357/834/2/110). arXiv: [1611.03184 \[astro-ph.HE\]](https://arxiv.org/abs/1611.03184).
- 1816 [57] Mattia Di Mauro and Martin Wolfgang Winkler. “Multimessenger constraints on the dark
1817 matter interpretation of the Fermi-LAT Galactic Center excess”. In: *prd* 103.12, 123005
1818 (June 2021), p. 123005. doi: [10.1103/PhysRevD.103.123005](https://doi.org/10.1103/PhysRevD.103.123005). arXiv: [2101.11027 \[astro-ph.HE\]](https://arxiv.org/abs/2101.11027).
- 1820 [58] HongSheng Zhao. “Analytical models for galactic nuclei”. In: *Mon. Not. Roy. Astron. Soc.*
1821 278 (1996), pp. 488–496. doi: [10.1093/mnras/278.2.488](https://doi.org/10.1093/mnras/278.2.488). arXiv: [astro-ph/9509122 \[astro-ph\]](https://arxiv.org/abs/astro-ph/9509122).
- 1823 [59] H. C. Plummer. “On the Problem of Distribution in Globular Star Clusters: (Plate 8.)”
1824 In: *Monthly Notices of the Royal Astronomical Society* 71.5 (Mar. 1911), pp. 460–470.
1825 ISSN: 0035-8711. doi: [10.1093/mnras/71.5.460](https://doi.org/10.1093/mnras/71.5.460). eprint: <https://academic.oup.com/mnras/article-pdf/71/5/460/2937497/mnras71-0460.pdf>. URL:
1827 <https://doi.org/10.1093/mnras/71.5.460>.
- 1828 [60] Daniel R. Hunter. “Derivation of the anisotropy profile, constraints on the local velocity
1829 dispersion, and implications for direct detection”. In: *JCAP* 02 (2014), p. 023. doi:
1830 [10.1088/1475-7516/2014/02/023](https://doi.org/10.1088/1475-7516/2014/02/023). arXiv: [1311.0256 \[astro-ph.CO\]](https://arxiv.org/abs/1311.0256).
- 1831 [61] Barun Kumar Dhar and Liliya L. R. Williams. “Surface mass density of the Einasto family
1832 of dark matter haloes: are they Sersic-like?” In: *Mon. Not. Roy. Astron. Soc.* (2010). doi:
1833 [10.1111/j.1365-2966.2010.16446.x](https://doi.org/10.1111/j.1365-2966.2010.16446.x).
- 1834 [62] M. Baes and E. Van Hese. “Dynamical models with a general anisotropy profile”. In:
1835 *Astron. Astrophys.* 471 (2007), p. 419. doi: [10.1051/0004-6361:20077672](https://doi.org/10.1051/0004-6361:20077672). arXiv:
1836 [0705.4109 \[astro-ph\]](https://arxiv.org/abs/0705.4109).
- 1837 [63] Matthew G. Walker, Edward W. Olszewski, and Mario Mateo. “Bayesian analysis of re-
1838 solved stellar spectra: application to MMT/Hectochelle observations of the Draco dwarf
1839 spheroidal”. In: *mnras* 448.3 (Apr. 2015), pp. 2717–2732. doi: [10.1093/mnras/stv099](https://doi.org/10.1093/mnras/stv099).
1840 arXiv: [1503.02589 \[astro-ph.GA\]](https://arxiv.org/abs/1503.02589).
- 1841 [64] Nicholas L. Rodd et al. “Dark matter spectra from the electroweak to the Planck scale”. In:

- 1842 *J. High Energy Physics* 121.10.1007 (June 2021).
- 1843 [65] Pace, Andrew B and Strigari, Louis E. “Scaling relations for dark matter annihilation and
1844 decay profiles in dwarf spheroidal galaxies”. In: *Monthly Notices of the Royal Astronomical
1845 Society* 482.3 (Oct. 2018), pp. 3480–3496. ISSN: 0035-8711. doi: [10.1093/mnras/sty2839](https://doi.org/10.1093/mnras/sty2839).
- 1847 [66] Albert, A. et al. “Search for gamma-ray spectral lines from dark matter annihilation in
1848 dwarf galaxies with the High-Altitude Water Cherenkov observatory”. In: *Phys. Rev. D* 101 (10 May 2020), p. 103001. doi: [10.1103/PhysRevD.101.103001](https://doi.org/10.1103/PhysRevD.101.103001). URL:
1849 <https://link.aps.org/doi/10.1103/PhysRevD.101.103001>.
- 1851 [67] Victor Eijkhout and Edmund Show and Robert van de Geijn. *The Science of Computing.
1852 The Art of High Performance Computing*. Vol. 3. Open Copy published under CC-BY 4.0
1853 license, 2023, pp. 63–66.